STUDIES OF THE EVOLUTION OF FELSIC MAGMA SYSTEMS: I. ZIRCON IN HISTORIC ERUPTIONS, ICELAND; II. MODELING MAGMA CHAMBER EVOLUTION LEADING TO THE PEACH SPRING TUFF SUPERERUPTION, ARIZONA, NEVADA AND CALIFORNIA

By

Tamara Lou Carley

Thesis

Submitted to the Faculty of the

Graduate School of Vanderbilt University

in partial fulfillment of the requirements for

the degree of

MASTER OF SCIENCE

in

Earth and Environmental Sciences

August 2010

Nashville, Tennessee

Approved:

Professor Calvin F. Miller

Professor Guilherme A.R. Gualda

To my family, with gratitude and love.

ACKNOWLEDGEMENTS

Above all I would like to thank Professors Calvin Miller and Guil Gualda for stimulating my curiosity and providing opportunities for intellectual growth, for organizing adventurous fieldwork excursions, and for their wisdom, patience, guidance and encouragement throughout this research experience. I would also like to express gratitude to the rest of my mentors and peers at Vanderbilt University, specifically to Professor David Furbish who asks what I want to do with my life, to Aaron Covey who makes the impossible possible, to Ayla Pamukcu for her work with the Peach Spring Tuff, to Abraham Padilla and Addy Petrilla for their invaluable assistance in the field and lab, to Lily Claiborne and Danny Flanagan for being intrepid leaders of Team Zircon, to Robin Vaum Lemons for blazing the trail with MELTS, and to Teri Sparkman and Jewell Beasley-Stanley who keep everything running smoothly

There are a number of people outside of the immediate Vanderbilt community who made this work possible. I would like to thank those who contributed to the Icelandic component of my research, specifically Joe Wooden, Jorge Vasquez and Frank Mazdab for their assistance at the Stanford-USGS SHRIMP lab, Professors Ilya Bindeman and Andy Barth for providing both zircons and encouragement, Professors Olgeir Sigmarsson, Gudrun Larsen and Karl Gronvold at the University of Iceland for graciously sharing their local expertise, and Peter Oswald and Professors Sheila Seaman, Karen Harpp and Denny Geist for being so willing to assist in our endeavors. I would also like to thank those who contributed to the Peach Spring Tuff component of my research, specifically Charles Ferguson for identifying the eruptive source of the tuff and for being such a helpful teacher in the field, Mark Ghiorso for modifying MELTS and for providing so much support and encouragement, Joe Dufek for introducing me to the physical aspects of magma systems, and Charile Bacon and Keith Howard for being supportive professional role models. I owe special thanks to my undergraduate mentors, specifically Kirsten Nicolaysen, Bob Carson, and Susan Sakimoto, who helped guide me towards an exciting future. Lastly, I would like to express heartfelt gratitude to my aunt, Wendy Beck, who never ceases to inspire me.

This research was made possible by a Geological Society of America Student Research Grant and National Science Foundation Grants NSF-EAR-0911726 and NSF-EAR-0635922.

TABLE OF CONTENTS

Page

LIST OF TABLES

LIST OF FIGURES

Part II.

PART I

ZIRCON IN HISTORIC ERUPTIONS, ICELAND

CHAPTER I

INTRODUCTION

Icelandic volcanism is controlled by a hotspot in conjunction with a propagating mid-ocean ridge (Figure 1). Approximately 10-12% of rocks in Iceland are silicic (Walker, 1966; Saemundsson, 1979; Gunnarsson et al., 1998), which is unusual in an oceanic setting (Jonasson, 2007). The abundance of silicic rocks in Iceland hints at continental nucleation in an oceanic setting (Gunnarson et al., 1998; Jonasson, 2007; Marsh et al., 1990; Sigmarsson et al., 1991; Jonasson, 1994). Understanding the petrogenetic process(es) creating these magmas has important implications for understanding Earth's early, and ongoing, history as it may provide insight to the formation of the first continents (Jonasson, 2007; Taylor and McLennan, 1985; Johannes and Holtz, 1996).

The generation of rhyolite in Iceland remains a topic of long-standing debate (e.g., Gunnarson et al., 1998, Martin and Sigmarsson, 2007). Two dominant explanations have been proposed: closed-system fractional crystallization of mafic magma (e.g., Carmichael, 1964; Macdonald et al., 1987, 1990; Furman et al., 1992; Prestik et al., 2001; Selbekk and Tronnes, 2007), and partial melting of mafic, hydrothermally-altered crust (e.g., O'Nions and Gronvold, 1973; Sigvaldason, 1974; Oskarsson et al., 1982; Condomines et al., 1983; Sigmarsson et al., 1991, 1992; Marsh et al., 1990; Gunnarsson et al., 1998; Sverrisdottir, 2007). A compelling combination-theory suggests that the thermal condition of the crust controls the rhyolite generation process; fractional crystallization dominates in off-rift systems where magma is injected into a cooler environment, and partial melting at on-rift volcanoes where abundant injected magma provides sufficient heat to melt the already-warm country rock (Martin and Sigmarsson, 2007).

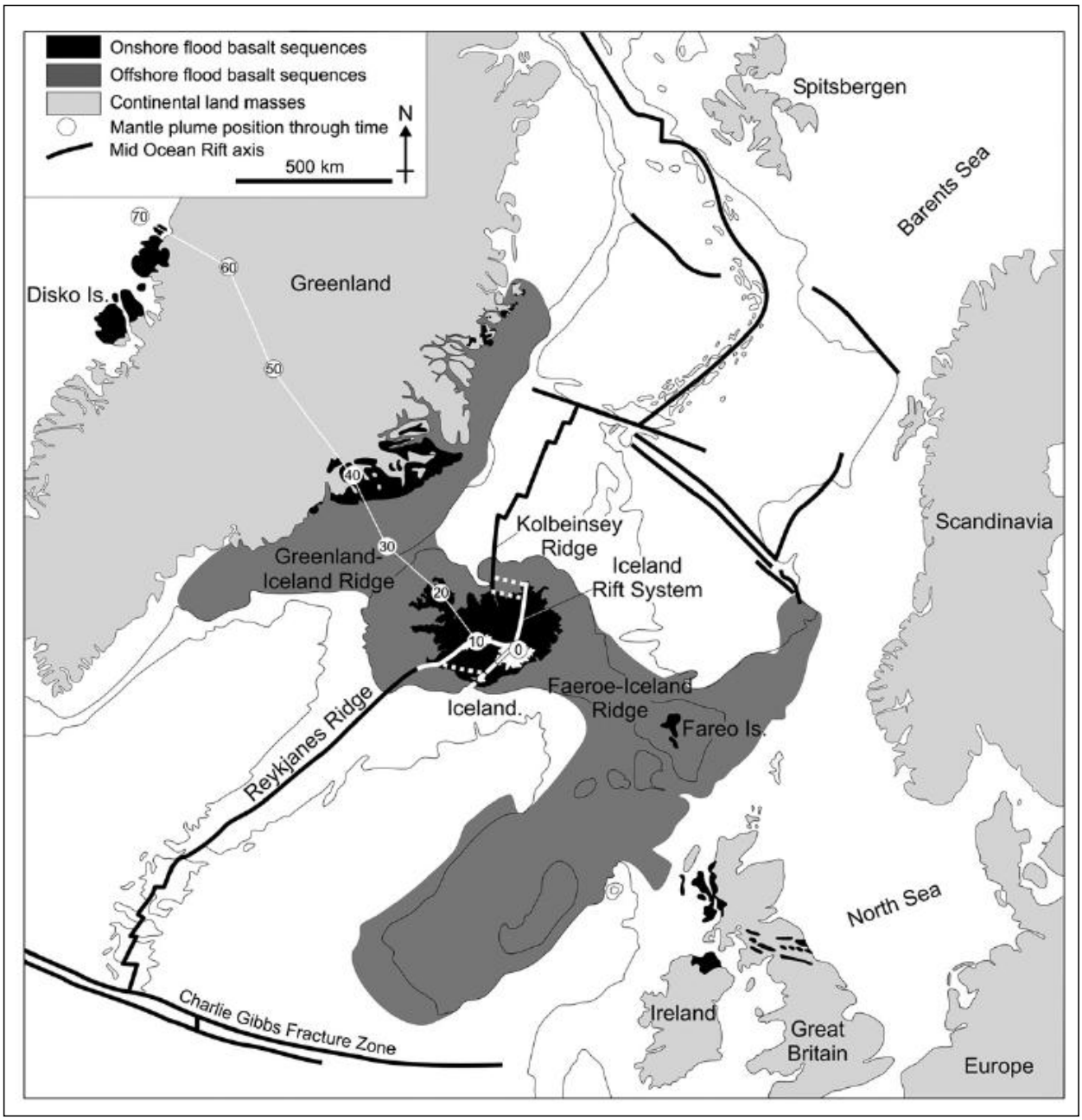

Figure 1

Tectonic and Magmatic Setting of Iceland from Thordarsson and Larsen, 2007.

While many people have investigated the occurrence of silicic rocks in Iceland, this is the first study to use zircon as a lens to examine the history of silicic magmas in Iceland (excepting one GSA abstract by Brown et al., 2004). Zircons are excellent trackers of magmatic processes. U-Th disequilibrium dating has demonstrated that zoned volcanic zircons can record several hundred k.y. of pre-eruption history with precisions of a few k.y. (Bacon et al., 2005; Claiborne et al., 2010b). Also, elemental analyses of zircons expose a record of magma chamber compositions, temperatures, and processes (Watson et al., 2006; Claiborne et al., 2006, 2010a, 2010b). For example, transects of zircon grown via closed-system fractional crystallization are expected to show an increase in fractionation (marked by rising Hf, indicating previous removal of zircon from the magma; Claiborne et al., 2006) and decrease in temperature (marked by falling Ti) toward the rim. Silicic magma formed by partial melting of a crustal source is likely to yield zircons with older cores inherited from the source region, possible resorption features, and trace element geochemistry signatures that deviate from the monotonic relationships associated with fractional crystallization. Open-system processes (e.g. magma recharge) also yield U/Th evidence of protracted histories and trace element concentrations that stray from the monotonic trends of closed-system fractionation (Claiborne et al., 2010a).

The growth and storage history of zircon can be expanded upon to reconstruct the history of host magmatic systems. Where these methods have been applied at Mount St Helens, zircon growth temperatures are substantially lower than eruption temperatures, and it is common to find abundant antecrysts (somewhat older cognate crystals) spanning a range of ages together with much rarer xenocrysts (introduced from genetically-unrelated systems during open-system processes) and phenocrysts (near-eruption age; Claiborne et al., 2010). These observations suggest that zircons are grown and stored in a cooling magma chamber, then remobilized in an eruption. These tests of magmatic dynamics and longevity can be applied to Icelandic systems. Notably, the few U-Th analyses by Brown et al. (2004) at Torfajokull document a span of zircon growth of 60 ka. A focused study of zircons using this particular combination of analytical techniques will add critical chronological, compositional, and thermal details to the histories of silicic magmas in Iceland, and provide valuable tests of their origins.

This study is based on zircons from silicic volcanic rocks from recent (primarily historical) eruptions in different tectonic regions of Iceland with distinct thermal structures and potential magma generating conditions. Eruptive deposits with peralkaline compositions were

avoided because the high solubility of zircons in such magmas makes it unlikely that zircons would be present. Guided by these criteria, we collected samples of silicic pumice and lava from four volcanic centers: Askja 1875 AD, on-rift; Torfajokull 871 and 1477 AD, on-rift, near termination; Hekla 1104 (or 1158[1]) AD, transitional; and Oraefajokull 1362 AD, off-rift (see Figure 2 for general locations and Table 1 for precise locations and sample descriptions). We also included two prehistoric eruptions of silicic lava (~7500 BP, ~3100 BP) at Torfajokiull, allowing us to conduct a longitudinal study at this volcanic center (zircon samples of Brown et al., 2004).

By sampling historical eruptions, we are able to confidently establish a precisely-known age (effectively zero) for the eruptions, which can readily be compared to the U-Th disequilibrium ages, representing crystal growth. Furthermore, the absolute uncertainty in U-Th age decreases with decreasing age, so the younger zircon that in general are expected in the products of young eruptions can be dated more precisely than zircon from older eruptions. The prehistoric eruptions that we study from Torfajokull are both less than 10 ka, much younger than the upper limit of effective U-Th dating (350 ka, ~ 5 half lives of ^{230}Th).

[1] While we had selected our sampling site with the intent to collect pumice from the 1104 AD eruption, our whole-rock geochemical analysis is consistent with published compositions for the 1158 AD eruption rather than the 1104 deposits (Larsen et al., 1999). The major differences between our sample and published compositions from the 1104 AD eruption are in SiO_2 (too low) and Fe_2O_3, MgO, CaO, TiO_2 (too high; Larsen et al. 1999).

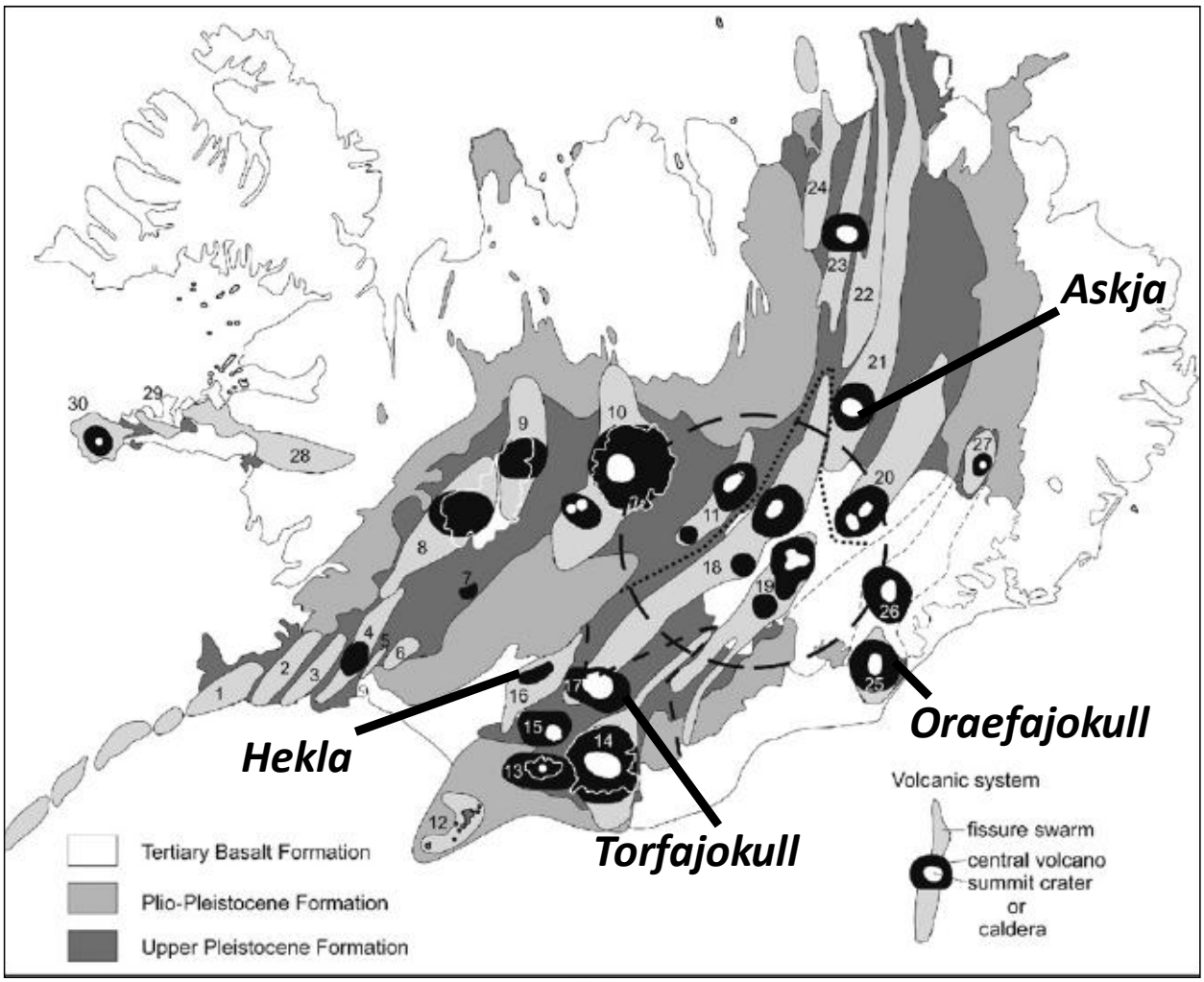

Figure 2

Distribution of volcanoes examined in this study: Askja, Oraefajokull, Hekla and Torfajokull. Image modified from Thordarson and Larsen, 2007.

Table 1

Overview of Eruptions and Samples Discussed in this Study

Volcano	Eruption Date	Erupted Volume (km^3)[2]	Sample Location	Sample Coordinates[3]	Sample type	SiO2 (wt%)[4]	Zr (ppm)	Zircon Sat. Temp (°C)[5]	Initial $^{230}Th/^{232}Th$
Askja	1875 AD	2 (0.2)[6]	Top of ridge to the NE of Lake Oskjuvatn	28 W 041996 7214591	Pumice	71.9	388	855	1.01[7]
Oraefajokull	1362 AD	10 (2)[8]	Small pit on SSE side of HWY 1, between Hofnes Farm and Hnappavellir turn-off	28 V 0420478 7086216	Pumice	72.4	813	932	0.99[9]
Hekla	1158 AD	0.33[10]	S. end of the burfell located W. of Hekla, 2m from ravine-top.	27 W 0558938 7106903	Pumice	68.7	718	920	0.97[11]
Torfajokull	1477 AD	0.01[12]	Lava flowing into Lake Frostastadavatn, at water line	27 W 0595113 7099846	Lava	66.3	668	890	0.9[13]
	871 AD	0.16	Flow access near Laufafell, near (but before) 2nd river ford when approaching from S.	27 V 0584358 7093649	Lava	66.9	605	880	0.9
	3100 BP	0.4	Domadalshraun vent	Unavailable[14]	Lava	70.1	755	920	0.9
	7500 BP	0.01	Domadalshraun vent	Unavailable	Lava	71.9	778	925	0.9

[2] Volume in parentheses given in Dense Rock Equivalent (DRE)
[3] All coordinates are given in UTM Hjorsey 1955
[4] Whole-rock geochemistry values for major elements are normalized to 100%
[5] Calculated using whole rock geochemistry and the methods of Watson and Harrison (1983) and Hanchar and Watson (2003)
[6] Non-DRE from Larsen et al., 1999, DRE from Sigurdson and Sparks ,1981, represents the volume of silicic pumice (not including basalt flows)
[7] Value from Condomines et al., 1981, measured using Askja 1875 AD dacite
[8] Non-DRE from Larsen et al., 1999, DRE from Thorarinsson, 1958; Sharma et al., 2008 suggests a value of 1.2 km^3
[9] Value from Rose-Koga and Sigmarsson, 2008
[10] Non-DRE from Larsen et al., 1999
[11] Value from Sigmarsson 2009, personal communication
[12] All Torfajokull lava volumes taken from Macdonald et al., 1990
[13] Value from Zellmer et al., 2004, 2008
[14] Zircons from the 3100 and 7500 BP eruptions of Torfajokull were from the Brown et al. 2004 study. Precise sampling locations are unavailable at this time.

CHAPTER II

OVERVIEW OF INVESTIGATED VOLCANIC SYSTEMS

Askja, Oraefajokull, Hekla and Torfajokull have been well-studied; regional settings and geochemistry have been characterized, eruptive timescales broadly constrained and petrogenetic models proposed (Jonasson, 1994; Gunnarson et al., 1998; Martin & Sigmarsson, 2007; Oswald and Geist pers. commun., 2009). We provide a brief summary of current knowledge of these four volcanic systems based on published descriptions as well as on our own observations and samples. With this comprehensive volcanic background, we have the benefit of focusing on the contributions of zircon to the debate of silicic petrogenesis.

Askja

We classify Askja's setting as "on rift" because it is located at the southern margin of the actively-spreading Northern Volcanic Zone (NVZ), one of the major components of the axial rift zone that cuts across Iceland (Thordarson and Larsen, 2007; Sparks et al., 1981). The base of the central volcano comprises a ring-like structure of sub-glacial palagonite (Sparks et al., 1981) with a 3-4 km diameter caldera from the 1875 eruption nested inside of an 8 km diameter caldera from a pre-historic eruption (Sparks et al., 1981). Since the 1875 eruption it has been recognized that the Askja central volcano is associated with the Sveinagja fissures located 70 km to the north, with rhyolite erupting from the caldera and basalt erupting from the fissure swarms contemporaneously (Sparks et al., 1981; Thordarson and Larsen, 2007). Ejecta from Askja are chemically distinct from other volcanic deposits in Iceland with comparable SiO_2 contents by their relatively high whole-rock MgO and TiO_2. There have been only two occurrences of silicic magma erupting from the Askja caldera since the last deglaciation, first at the start of the Holocene (Sigvaldason, 2002) and most recently the 1875 AD eruption that we are examining in this study. Tholeiitic ferrobasalt and icelandite were erupted in 1875, as well as silicic and mixed pumice that have a compositional range of 58-74 wt% SiO_2 (MacDonald et al., 1987).

Fractional crystallization has been proposed, and generally accepted, as the favored model for generating rhyolite at Askja. Some argue that extreme fractional crystallization alone can explain the origin of rhyolites from ferrobasalt (e.g., Wood et al., 1978, 1979) while others

cite fractional crystallization as the dominant process at work with contributions from minor wall-rock assimilation, partial melting of silicic xenoliths, and basaltic injection explaining complex trace element geochemistry and low $\partial^{18}O$ (Macdonald et al., 1987; Sigurdsson and Sparks, 1981).

The 1875 AD eruption that formed the Oskjuvatn caldera produced 2 km^3 (0.2 km^3 DRE) of silicic tephra (Larsen et al., 1999; Sigurdson and Sparks, 1981; Macdonald et al., 1987; Jonasson, 2007). Some of the pumice ejected during the 1875 eruption was purely rhyolite, and this is what we chose to collect for our study ("white rhyolite" of Sparks et al. 1981). There is also a great deal of pumice with streaks of tholeiitic basalt, ferrobasalt and icelandite that was mingled with the rhyolite as magma immediately before, or during, eruption (Macdonald et al., 1987).

The pumice that we collected for this study is extremely crystal-poor (<1%), with minor plagioclase, clinopyroxene, Ti-Fe oxides and accessory zircon. Our geochemical analyses (Table 2) and physical observations of coarse, low-density pumice are consistent with those published for "layer D" by Sparks et al. (1981) and MacDonald et al. (1987). Zircon yield was so low in this pumice that we were unable to extract any using our density and picking separation methods. Askja zircons analyzed in this study were extracted from "layer D" pumice and shared by Dr. Ilya Bindeman.

Oraefajokull

Oraefajokull is located in the Oraefi Volcanic Belt (OVB), an active intraplate volcanic zone located at the southern margin of the Eastern Volcanic Flank Zone (Thordarson and Larsen, 2007; Selbekk and Tronnes, 2007; Presvik et al., 2001). The OVB is thought to be a potential "embryonic rift" but for our purposes in this study we classify Oraefajokull as "off-rift" because of its distance (~50 km east) from the dominant axial rift zone (Thordarson and Larsen, 2007; Thordarson and Hoskuldsson, 2002; Selbekk and Tronnes, 2007; Prestvik et al., 2001). The central volcano, the largest in Iceland, is thought to sit unconformably on uplifted and eroded Tertiary basalt (Larsen, 1998; Prestvik, 1985; Presvik et al., 2001; Selbekk and Tronnes, 2007). The base of the volcano is composed dominantly of subglacially erupted pillow basalt and hyaloclastite breccia and tuff (Selbekk and Tronnes, 2007; Prestvik, 1979, 1985; Prestvik et al., 2001). The volcanic deposits from Oraefajokull are compositionally bimodal (basalt and

rhyolite) with notably high Na_2O, low MgO compositions that makes it distinct from the rift-zone volcanoes (Prestvik et al., 2001; Larsen, 1998). Explosive post-glacial eruptions at Oraefajokull are thought to have originated from an ice-filled summit caldera with an area of 14 km^2 (Sharma et al., 2008; Selbekk and Tronnes, 2007).

It has been proposed that rhyolite at off rift volcanoes like, and including, Oraefajokull is likely produced by fractional crystallization because new, hot magma is injected into crust that is "thicker, cooler and stronger" than crust in an extensional zone and better able to dissipate heat without reaching solidus temperatures (Sellbek and Tronnes, 2007; similar to Martin and Sigmarsson, 2007).

There have been two explosive eruptions in historical times, one in 1362 AD and again in 1727 AD (Larsen et al., 1999; Selbekk and Tronnes, 2007). The 1362 AD Plinian eruption that we are examining in this study produced 10 km^3 (2 km^3 DRE) silicic tephra, and is thought to be "the most voluminous explosive silicic eruption" in Iceland in historical times (Larsen et al., 1999; Thorarinsson, 1958; Sharma et al., 2008). Pumice from the 1362 eruption is extremely crystal poor (<1%) with minor plagioclase, olivine, clinopyroxene, Fe-Ti oxides and accessory zircon (our observations; Selbekk and Tronnes, 2007). The pumice from the 1362 eruption is distinct because of the extreme compositional homogeneity of the glass and phenocrysts throughout the entire recognized deposit (Selbekk and Tronnes, 2007). This striking homogeneity is taken to represent a uniform and extremely well-equilibrated magma chamber, or upper zone in a large magma chamber (Selbekk and Tronnes, 2007).

The Oraefajokull pumice that we analyzed has a whole-rock composition that is typical of published results describing pumice from the 1362 eruption (Table 2; Sharma et al., 2008; Selbekk and Tronnes, 2007).

Hekla

We classify Hekla's tectonic setting as "transitional" to the main axial rift that runs through Iceland because it is located at the western extreme of a propagating rift that extends from the Eastern Volcanic Zone (EVZ; Sverrisdottir, 2007). The volcanic center forms a NE-SW trending ridge built upon basaltic hyaloclastite of Pleistocene age (Sverrisdottir, 2007). Silicic magma erupts from a 5 km-long summit fissure and from short radial fissures on the flanks of the volcano, while basalt erupts from the Vatnafjoll fissure swarm that runs parallel to the Hekla

ridge (Thordarson and Larsen, 2007; Sverrisdottir, 2007; Gronvold et al., 1983). Hekla erupts lava and tephra that span compositions from basalt through icelandite to rhyolite, breaking the Icelandic pattern of compositionally bimodal eruptive deposits (Sverrisdottir, 2007). Approximately 95% of the intermediate lava that has been erupted in Iceland in historical times has been erupted from Hekla. The silicic tephra erupted during the 1158 AD event can be distinguished from other historical deposits of silicic material based on its relatively high FeO and CaO, and low K_2O (Larsen et al., 1999).

Partial melting of tholeiitic crust with subsequent magma mixing has been proposed as a mechanism for silicic magma generation at Hekla, based on Th isotopes and major-mineral composition and zoning (Sverrisdottir, 2007). Fractional crystallization of a persistent basaltic andesite magma chamber beneath the volcano has also been suggested as a viable process for creating silicic magma based on mineral assemblages and compositions, as well as whole-rock and glass compositions that display continuous and for some elements (e.g., Zr) inflected trends extending from mafic to silicic end members (Oswald et al., 2007; Geist pers. commun., 2009).

It has been observed that the SiO_2 content of the magma ejected from Hekla during an eruptive event decreases throughout the course of the eruption. The SiO_2 content of the first erupted material correlates with the period of time that has passed since the last eruption, with higher SiO_2 compositions following longer periods of repose (Thorarinsson, 1967; Oswald et al., 2007). Historical eruptions at Hekla, including the 1158 eruption, have followed a generally consistent pattern, starting with a brief (<1 hr) but vigorous subplinian to Plinian event in which a great deal of magma is evacuated from the chamber, followed by a period of simultaneous lava fountaining and tephra ejection, and concluding with intermittent Strombolian eruptions (Thordarson and Larsen, 2007).

The pumice that we collected for this study is crystal-poor (<5%), with a phenocryst assemblage characteristic of Hekla consisting of plagioclase, fayalitic olivine, clinopyroxene, Fe-Ti oxides, apatite, and zircon. Whole rock geochemistry of our sample matches almost perfectly that of 1158 tephra (Table 2; Larsen et al., 1999).

Torfajokull

Torfajokull is located within the non-spreading Southern Flank Zone (SFZ) in a volcanically-active belt at the intersection of the Eastern Rift Zone (ERZ) and the South Iceland

Seismic Zone (SISZ; Gunnarsson et al., 1998). We choose to classify the setting of Torfajokull using the term "propagating rift" from Gunnarson et al. (1998). The Torfajokull central volcano is a large caldera structure, 30 km long in the WNW-ESE direction and 18 km wide in the NE-SW direction, that is built upon 10 Ma tholeiitic crust (Gunnarsson et al., 1998). More than 80% of the volcano exposed at the surface is composed of silicic extrusives, and with a volume of ~225 km^3 and an area of ~450 km^2, Torfajokull is the largest exposure of silicic rock in all of Iceland, and perhaps in the entire oceanic crust (Gunnarsson et al., 1998; Larsen et al., 1999). Torfajokull is also the largest high-temperature geothermal region in Iceland, which has led to pervasive hydrothermal alteration of crust in the area (Arnorsson et al., 1987; Saemundsson, 1988; Gunnarsson et al., 1998). Postglacial rhyolite and basalt have erupted from linear fissures in the western part of the caldera, which is thought to be the most actively-fissuring section of the ERZ (Gunnarson et al., 1998). Basaltic volcanism often occurs at the nearby Veidivotn fissure swarm contemporaneously with rhyolitic eruptions from the Torfajokull caldera fissures (Zellmer et al., 2008; Mork, 1984; Blake, 1984; Jonasson, 2007).

One explanation for silicic magmatism at Torfajokull is that >90% fractional crystallization of parental basalt has yielded sub-alkaline rhyolites, and continued fractionation of these sub-alkaline melts led to peralkaline rhyolite generation (Macdonald et al., 1990). This conclusion was drawn by analysis and interpretation of whole rock geochemical trends. A second explanation is that magma influx related to rifting and fissuring of the crust in the Torfajokull area supplies heat necessary for partial melting of the hydrothermally altered crust (Gunnarsson et al., 1998). It has been suggested that this silicic partial melt is stored and continues to evolve to its final composition by crystal fractionation before being erupted (Zellmer et al., 2008; Martin and Sigmarsson, 2007). These conclusions were drawn on the basis of low $\delta^{18}O$ values and whole-rock trace element geochemistry.

In this study we examine 4 post-glacial (2 pre-historic, 2 historic) eruptions of silicic lava: 7500 BP at Domadalshraun (0.74 km^2, 0.0126 km^3), 3100 BP from the Domadalshraun vent (1.13 km^2, 0.0396 km^3;), 871 AD Hrafntinnuhraun flow (4.87 km^2, 0.160 km^3) and the 1477 AD Namshraum flow (0.87 km^2, 0.0084 km^3 (Macdonald et al., 1990). In general, Torfajokull lavas are characterized as being high K rhyolites with low crystallinity (<7%) and mineral assemblages that include plagioclase, anorthoclase, clinopyroxene, Fe-Ti oxides, hornblende, olivine, apatite and zircon (Gunnarsson et al., 1998). Our whole-rock geochemical analyses for

the prehistoric eruptions (3100 BP, 7500 BP, Barth pers. commun., 2009) are consistent with published results, while historical (1477 AD, 871 AD) eruptions show compositions with lower SiO_2 and K_2O and higher Al_2O_3 and TiO_2 than published results (among other differences; Table 2; MacDonald et al., 1990).

Table 2

Major[15] and Trace Element Geochemistry of Pumice and Lava Samples

	Askja 1875 AD	Oraefajokull 1362 AD	Hekla 1158 AD	Torfajokull 871 AD	1477 AD	3100 BP[16]	7500 BP
Major Elements (wt%)							
SiO_2	71.9	72.4	68.7	66.9	66.3	70.1	71.9
Al_2O_3	12.6	13.2	14.6	14.4	14.9	14.9	14.1
$Fe_2O_{3\ (T)}$	4.63	3.97	5.95	4.97	5.79	3.26	2.70
MnO	0.11	0.10	0.15	0.10	0.12	0.08	0.07
MgO	0.86	0.04	0.30	1.85	0.96	0.22	0.13
CaO	2.79	1.10	2.78	2.43	2.51	1.06	0.75
Na_2O	3.78	5.40	4.69	4.75	5.20	5.54	5.52
K_2O	2.28	3.40	2.37	3.86	3.60	4.47	4.52
TiO_2	0.89	0.27	0.40	0.69	0.54	0.32	0.24
P_2O_5	0.20	0.02	0.07	0.10	0.08	0.04	0.02
(LOI)	1.23	1.97	1.03	0.24	0.17	0.41	0.50
Selected Trace Elements (ppm)							
Rb	52	71	48	94	81	112	114
Sr	107	64	219	115	140	81	51
Ba	372	669	578	418	483	505	421
Cs	0.3	0.6	0.4	0.8	0.6		
Pb	<5	<5	<5	7	<5		
Nb	40	94	91.9	127	114	135	160
Ta	2.28	4.74	4.47	6.3	6.34		
Co	4.5	1.4	2.1	10.7	6		
Cr	<0.5	7.1	9.8	72	8.4		
Ni	2	2	5	45	8		
V	27	<5	<5	54	39		
Zr	388	813	718	605	668	755	778
Hf	10.7	21.1	18.2	16.2	17.7		
Th	7.46	10.3	9.81	15.2	14.1		
U	2.19	3.07	2.92	4.58	4.3		
Sc	11.6	1.43	9.84	6.12	6.88		
Y	57	102	76	56	59	76	96
La	40.1	69.5	70.1	78	74.8	94	94
Ce	81.2	150	143	152	154		
Pr	9.67	18.3	17.3	16.7	17.3		
Nd	39	73.9	68.2	60.3	61.9		
Sm	9.14	17.2	15.1	11.9	12.3		
Eu	2.13	3.06	3.65	1.72	2.3		
Gd	9.63	18	14.6	11.1	11.5		
Tb	1.66	3.23	2.48	1.77	1.92		
Dy	10.3	19.4	14.6	10.8	11.5		
Ho	2.15	3.82	2.86	2.12	2.23		
Er	6.45	11.1	8.27	5.98	6.48		
Tm	0.98	1.67	1.25	0.88	0.96		
Yb	6.5	11.3	8.48	5.91	6.3		
Lu	1.06	1.81	1.34	0.91	1		

[15] Major element compositions are normalized to 100% (excluding LOI).

[16] Whole rock data for prehistoric eruptions at Torfajokull were shared by Andy Barth and Brown et al. (2004).

CHAPTER III

METHODS

Whole rock geochemistry

Samples of silicic pumice and lava were sent to Activation Laboratories (ActLabs, Ancaster, Ontario Canada) for lithogeochemistry analysis. ActLabs pulverized samples using mild steel and then used a combination of inductively coupled plasma optical emission spectroscopy (ICP), instrumental neuron activation analysis (INAA), inductively coupled plasma mass spectrometry (ICP-MS) and x-ray fluorescence spectrometry (XRF) to measure major and trace element concentrations. Results can be found in Table 2.

Zircon separation methods

We removed individual zircon grains from bulk-rock samples in a process that included crushing, density separation by water table and heavy liquid (LST), magnetic susceptibility separation by Frantz magnetic separator, and hand-picking. Approximately 5 kg of each sample was processed for mineral extraction.

Zircon image analysis

Zircon grains were mounted in epoxy and polished to expose grain interiors. Once mounted, grains were imaged under a reflected light microscope and by cathodoluminescence (CL) on the JEOL JSM 5600 scanning electron microscope (SEM), at the Microanalysis Center shared by the US Geological Survey (USGS) and Stanford University (see Appendix A for all CL images). We used reflected light and CL images to characterize zircon populations using the following criteria: maximum length, representative width, presence of discrete (typically CL-dark) centers, presence and character of zoning, and signs of resorption. We determined average characteristics for individual zircon populations from each sample in this study, and then conducted an inter-eruption comparison with the goal of either (a) identifying universal morphological characteristics of historical zircons from Icelandic volcanoes, or (b) to identify unique morphological characteristics based on the individual volcanic system and setting (thermal and tectonic).

Zircon SHRIMP-RG trace element analysis

The Stanford-USGS sensitive high resolution ion microprobe reverse geometry (SHRIMP-RG) was used to determine trace element compositions of zircons, emphasizing Hf, U, Th, Ti and rare earth elements (REE). The basic operating parameters of the SHRIMP-RG, elemental suite analyzed, and data reduction techniques are as described in Claiborne et al. (2006, 2010a). A beam size of 15 μm was used in analysis, and spot placement was determined for each grain using CL and reflected light images. Where possible, multiple spots were placed on grains to discern differences between grain interiors and rims.

Zircon saturation temperatures and Ti-in-zircon thermometry

Zircon saturation temperatures were estimated using the equation:

$$ln\ D_{Zr}^{zircon/melt} = (-3.8-[0.85(M-1)]+12900/T$$

rearranged to

$$T_{Zr} = 12900/[2.95+0.85M+\ln(496000/Zr_{melt})]$$

where $D_{Zr}^{zircon/melt}$ is the concentration ratio of Zr in zircon to Zr in the melt, Zr in zircon is taken to be ~476,000 ppm, M is the cation ratio (Na+K+2*Ca)/(Al*Si), and T is temperature in Kelvin (Watson and Harrison 1983; Miller et al. 2003). Concentrations of Zr in melt and the cation ratio M were determined estimated using whole-rock geochemical analysis. Whole-rock geochemistry was appropriate to use in this study because our pumice and lava samples are dominantly unaltered volcanic glass with small volumes of phenocrysts (<10-15%), and therefore bulk analyses are comparable to melt compositions.

We estimated zircon crystallization temperatures using the calibrated Ti-in-zircon thermometry equation determined by Ferry and Watson (2007):

$$\log(\text{ppm Ti-in-zircon}) = (5.711\pm0.072)-(4800\pm86)/T(K)-\log a_{SiO2} + \log a_{TiO2}$$

rearranged to

$$T(K) = \frac{-(4800 \pm 86)}{\log[\text{ppm Ti-in-zircon}]+\log(\alpha SiO2)-\log(\alpha TiO2)-(5.711 \pm 0.072)}$$

Temperatures calculated by this method are dependent on a_{TiO2} and a_{SiO2}. The a_{TiO2} in a typical silicic magma usually falls between 0.6 and 0.9 (Ferry and Watson, 2007; Watson et al., 2006). Overestimating a_{TiO2} leads to an underestimate of temperature; for example, a calculation with an activity of 0.9 may yield a temperature of 777 °C while an activity of 0.7 for the same sample will yield a temperature of 803 °C. The calculated a_{TiO2} of our Icelandic samples fell within a range of 0.4->1 (based on the method of Hayden et al. [2007] and Ti concentrations in the whole-rock necessary to saturate rutile of 750 - 900 °C; in all cases, calculated values approach or exceed unity at T = 800 °C). We decided to assume a uniform a_{TiO2} of 0.7 (broadly consistent with our findings) to calculate Ti-in-zircon temperatures. The a_{SiO2} of quartz-undersaturated silicic melts is rarely less than 0.5 (Ferry and Watson 2007; Watson et al 2006; Hayden et al. 2007; cf. Carmichael et al. 1974), but overestimating a_{SiO2} can lead to calculated temperatures that exceed reality by tens of degrees (°C); for example, a calculation with an activity of 1 may yield a temperature of 805 °C while an activity of 0.7 for the same sample will yield a temperature of 782 °C. Despite these potential errors, we chose to use an assumed a_{SiO2} of 1 in our calculations since zircons are likely to grow in conditions near quartz saturation. Because we cannot quantify the degree to which our estimated activities stray from reality, we cautiously use the Ti-in-zircon thermometer to qualitatively examine intra- and inter-population thermal relationships, rather than to place undue confidence in precise temperatures.

U-Th disequilibrium dating

We use U-Th disequilibrium dating techniques to calculate model ages for the timing of zircon growth. This variation on traditional radiometric dating is particularly well-suited for young (<350 ka) zircons. U-Th disequilibrium ages were calculated using the method previously described by Lowenstern et al. (2000) and Charlier et al. (2005). Our decision to focus our efforts on historical eruptions allows us accurately identify a "zero" age at the time of eruption. Initial whole-rock $^{230}Th/^{232}Th$ ratios for individual volcanoes and, where available, individual eruptions, were taken from published literature (Table 1), and U-Th analyses of individual zircon were conducted using the SHRIMP and a beam size of 30 μm.

CHAPTER IV

RESULTS

Zircon Morphology

Zircon morphology (shape, size, aspect ratio, and zoning pattern) provides important clues to magmatic processes during the lifetime of the grain (e.g., growth rates, magmatic composition, fluctuations in temperature; Hanchar and Miller, 1993; Corfu et al., 2003). In Table 3 we summarize the morphology of the zircon populations from each of our samples. Detailed descriptions and CL images of each zircon grain are available in Appendix A.

Zircon populations in the eruptions from Askja 1875 AD pumice (by Dr. Bindeman), Oraefajokull 1362 AD pumice, Hekla 1158 AD pumice, and Torfajokull 1477 AD, 871 AD, 3100 BP and 7500 BP lavas yielded very sparse, very small zircons (see Table 3). In total, only 191 identifiable zircons were separated from our total sample-set (~5 kg material per eruption). Of these 191 zircons, 72 (38%) are mostly intact (mostly unbroken) while the remaining 119 grains (62%) are identifiable fragments. A compilation of images representing the variety of Icelandic zircon morphologies exhibited by these grains can be seen in Figure 3.

Of all intact grains observed, 40% have discrete dark centers. Oraefajokull and Torfajokull 871 AD have the highest percentage of intact grains with discrete centers, at 60%. Torfajokull 1477 AD, Torfajokull 3100 BP and Hekla 1158 AD zircons have the lowest percentage of intact grains with discrete centers, at 20%. Of all grains examined (intact and fragments), ~70% are visibly zoned in CL; this value increases to ~82% when only intact grains are considered. Overall, the dominant zoning pattern displayed is simple concentric zoning with low brightness contrast. Sector zoning is observed only in the Oraefajokull zircons. The Oraefajokull zircon population is also unique because it exhibits mottled textures in the dark, discrete interiors of multiple grains, a feature not observed in the other zircon populations in this study. Zircons from the historic eruptions of Torfajokull (1477 AD, 871 AD) are also noteworthy because there are a number of examples of rounded grain rims.

Table 3

Averaged Observations of Zircon Population Morphological Features

Eruption	Count	Max length (μm)	Max. Width (μm)	Aspect Ratio[17]	Discrete Center[18] [19]	Obvious Zoning	Obvious Rounding[20]
Askja 1875 AD (all)[21]	10	119	59	2	0.1	0.7	0.2
Askja 1875 AD (intact)[22]	4	120	54	2.1	0.3	0.5	0.3
Oraef. 1362 AD (all)	39	133	38	2.5	0.5	0.8	0.2
Oraef. 1362 AD (intact)	20	131	40	3.3	0.6	1.0	0.2
Hekla 1158 AD (all)	46	166	43	3.3	0.2	0.7	0.2
Hekla 1158 AD (intact)	16	161	42	3.3	0.2	0.8	0.4
Torfa. 871 AD (all)	9	91	42	2	0.3	0.9	0.6
Torfa. 871 AD (intact)	5	108	41	2.5	0.6	0.8	0.6
Torfa. 1477 AD (all)	17	103	54	2	0.2	0.4	0.5
Torfa. 1477 AD (intact)	6	115	58	2	0.2	0.7	0.7
Torfa. 7500 BP (all)	37	112	64	1.7	0.2	0.7	0
Torfa. 7500 BP (intact)	16	128	63	2	0.4	0.8	0
Torfa. 3100 BP (all)[23]	32	84	47	1.7	0.1	0.8	0
Torfa. 3100 BP (intact)	6	107	48	2	0.2	1.0	0
Total Iceland (all)	191	123	49	0.5	2	0.7	0.2
Total Iceland (intact)	72	132	48	0.4	2.5	0.8	0.2

[17] Aspect ratio was calculated by taking the aspect ratio (width/length) of each grain, and then averaging each of these ratios to find the average aspect ratio for each individual population. To find the total Iceland average, we averaged the ratios for each individual grain (not an average of population aspect ratio).

[18] Data in columns titled "Discrete Center," "Obvious Zoning," and "Obvious rounding" refers to the fraction of grains that display these qualities.

[19] A discrete center is identified as a dark interior that is distinguishable, with clear boundaries, from the rest of the surrounding zircon grain.

[20] We looked for evidence of rounding (possible resorption) at grain rims and at the boundaries of discrete interiors.

[21] Our mineral separation efforts yielded no zircon from Askja. Zircon examined in this study were graciously separated and shared from "layer D" pumice by Dr. Ilya Bindeman.

[22] "Intact" refers to zircon grains that have most grain boundaries preserved (mostly-unbroken)

[23] Zircon from the 3100 BP and 7500 BP eruption of Torfajokull are the same zircon used for the Brown et al., 2004 GSA abstract. These zircons were graciously shared with us by Dr. Andy Barth.

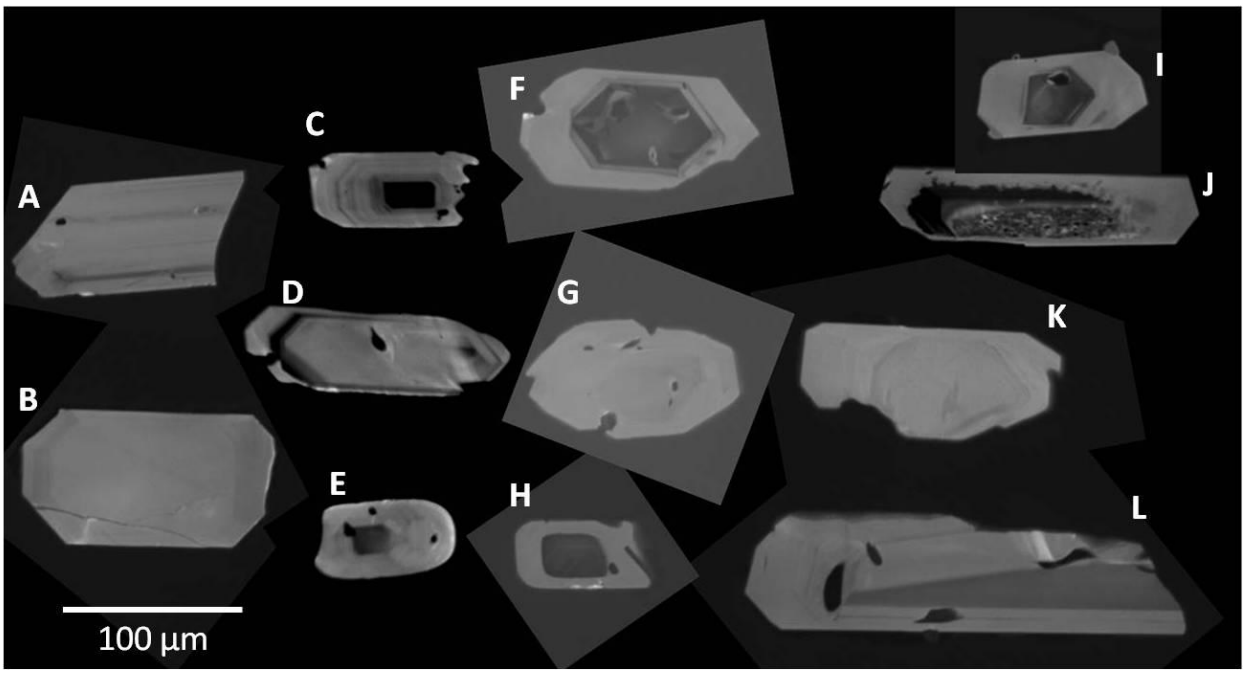

Figure 3

Twelve zircons representing the variety of morphologies seen in Iceland. A-B: Askja; C-E: Torfajokull 871 AD; F-H: Torfajokull 1477 AD; I-J: Oraefajokull; K-L: Hekla. Grain A from Askja, C, D and F from Torfajokull, I and J from Oraefajokull and L from Hekla all display high-CL brightness contrast zoning. Grain B from Askja, G from Torfajokull and K from Hekla all exhibit low CL brightness contrast zoning. Grains C, E, F and H from Torfajokull, I and J from Oraefajokull all have discrete dark centers. Grains E and H from Torfajokull have rounded edges that are suggestive of resorption and grain J from Oraefajokull has a dark, discrete, mottled interior zone.

U-Th Ages

We calculated model ages for zircon growth using U-Th disequilibrium dating techniques (Lowenstern et al., 2000; Charlier et al., 2005) for zircons from all samples except for Askja 1875 AD. We were unable to successfully date zircons from Askja due to large errors related to very low U concentrations and Th-U ratios. All calculated ages of zircon growth fall in a period time extending from near-eruption to ~50ka (Figures 4 and 5). These ages are much younger than seem possible based on published estimates for zircon growth rates (<~10^{-15}cm s-1; Watson, 1996), but are consistent with zircon ages reported from volcanics at Mount St. Helens (Claiborne et al., 2010b) and the Taupo Volcanic Zone (Charlier et al., 2005). Initial whole-rock $^{230}Th/^{232}Th$ ratios used in these calculations, taken from published literature, can be found in Table 1.

Each zircon population shows a distinct distribution of ages (Figures 4 and 5). Zircons from the 1362 AD eruption at Oraefajokull grew in a range of time from near-eruption (~zero ka) to approximately 35 ka. All ages fall in a continuous range, with the exception of the 35 ka date, which is significantly older than the rest. Hekla zircons grew in a period spanning from near-eruption to more than 40 ka. The calculated ages do not fall in a continuous cluster, but more zircon grains must be collected and analyzed before we can confidently distinguish between continuous or multiple episodes of growth. The history of zircon growth at Torfajokull preceded eruption dates by ~0-50 ka. The majority (78%) of this growth occurred between 10-30 ka before eruption. There is notable similarity between growth ages in zircon from the 1477 and 871 AD eruptions. The ages in the 1477 eruption range from 0-25 ka, with one older outlier making the age distribution discontinuous. Zircon ages in the 871 AD eruption are slightly older, ranging continuously from 10-30 ka. Zircons from these two eruptions show significant overlap in the period of time from 10-25 ka: 62% of ages from the 1477 eruption and 63% of ages from the 871 eruption falling within this range. The prehistoric eruptions at Torfajokull extend the growth history to older pre-eruptive ages. Zircons from the 3100 BP eruption have a discontinuous age distribution ranging from ~5-40 ka, with 2 grains dating 15ka+ older than the rest of the population (in the 35-40 ka range). The 7500 BP eruption shows the oldest-overall ages of the combined dataset, with zircon growth pre-dating the eruption by 15-45 ka in a continuous age distribution.

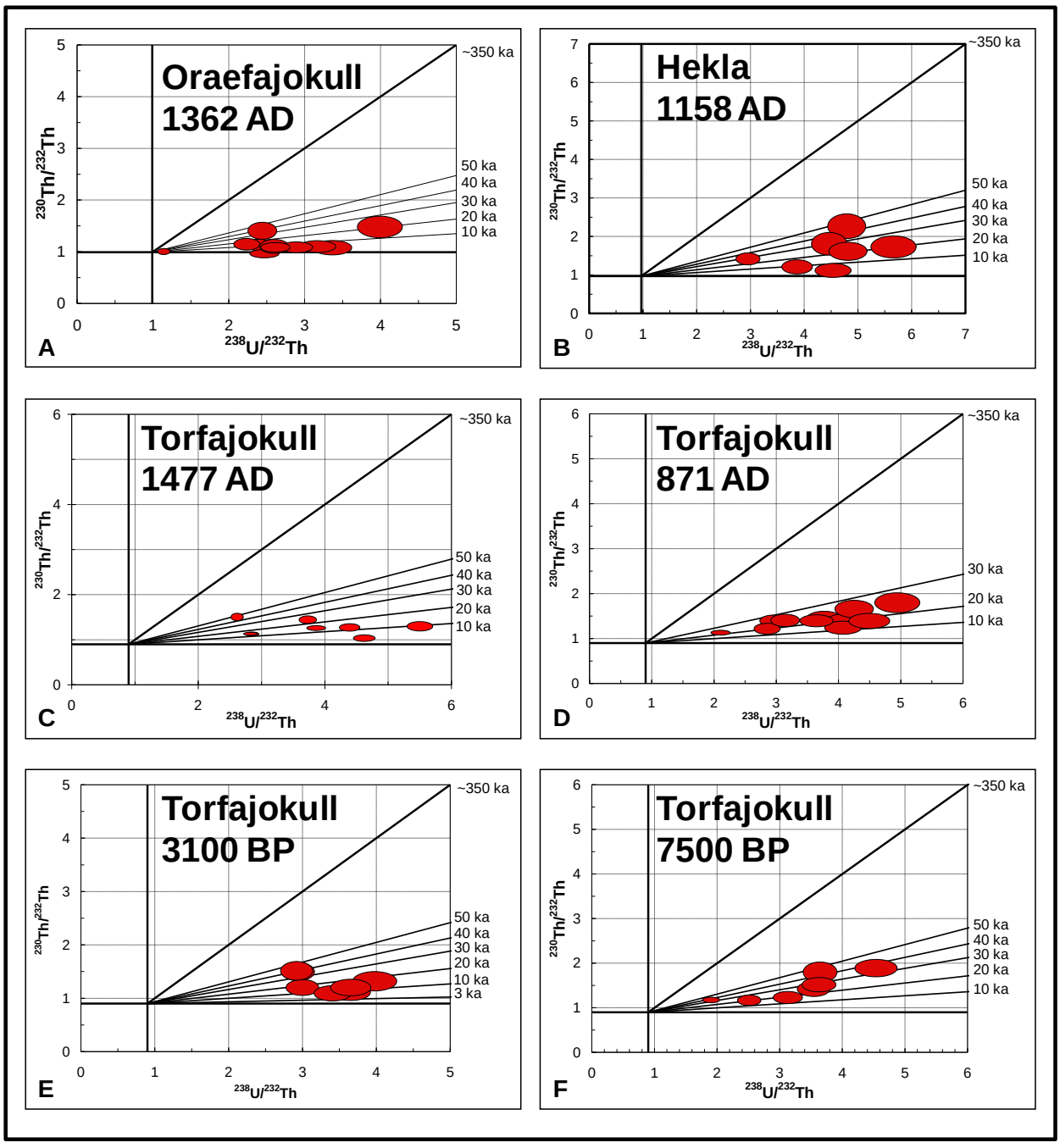

Figure 4

($^{230}Th/^{232}Th$) vs ($^{238}U/^{232}Th$) isochron-style diagrams for model ages derived using U-Th disequilibrium dating techniques (Lowenstern et al. 2000; Charlier et al. 2005). A: Oraefajokull; B: Hekla; C: Torfajokull 1477 AD; D; Torfajokull 871 AD; E: Torfajokull 3100 BP; F: Torfajokull 7500 BP. Initial ($^{230}Th/^{232}Th$) ratios for each eruptive deposit were taken from published literature and can be found in Table 1.

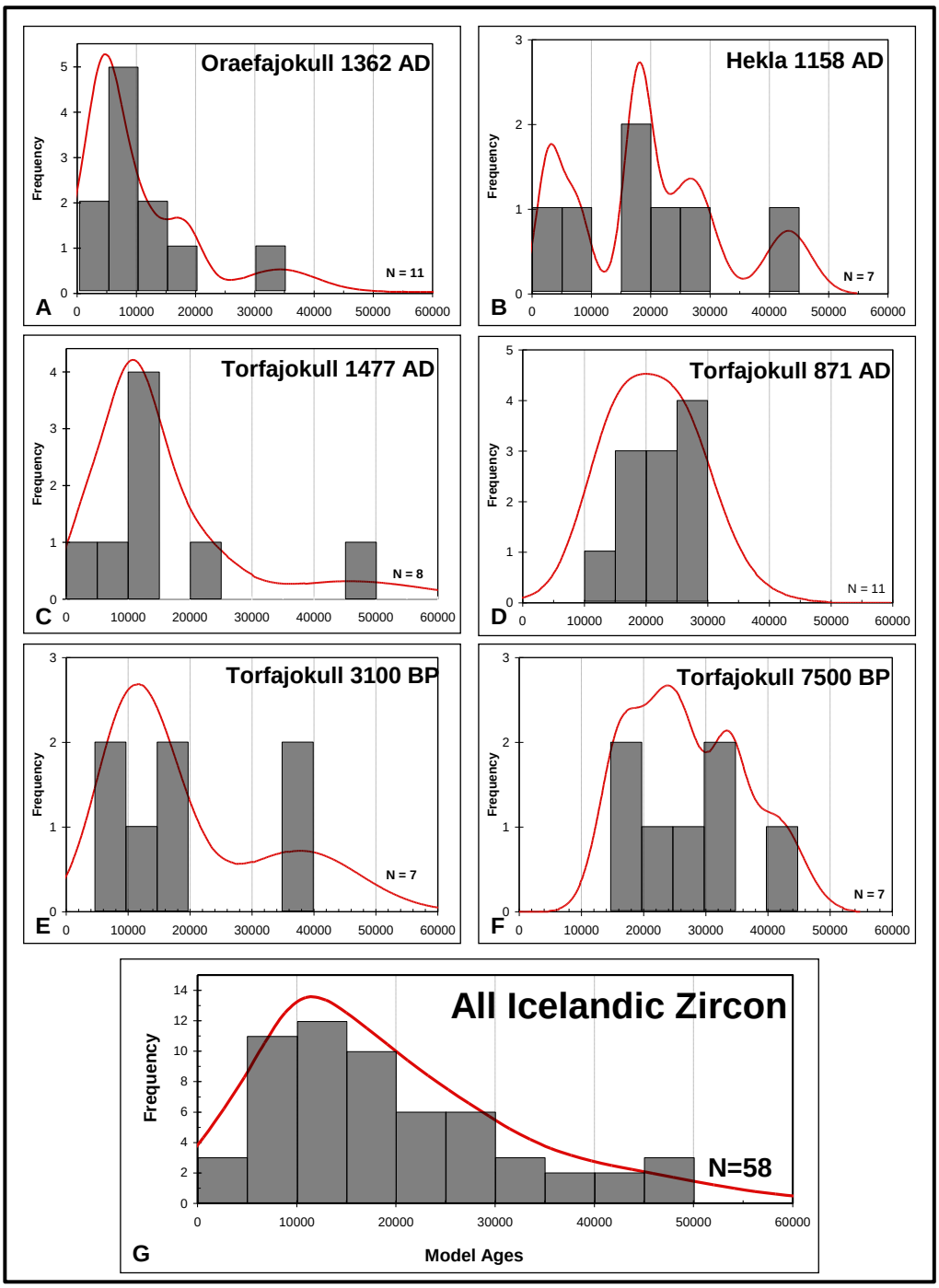

Figure 5

Probability density curves for model ages derived using U-Th disequilibrium dating techniques (Lowenstern et al. 2000; Charlier et al. 2005). A: Oraefajokull; B: Hekla; C: Torfajokull 1477 AD; D; Torfajokull 871 AD; E: Torfajokull 3100 BP; F: Torfajokull 7500 BP. Initial ($^{230}Th/^{232}Th$) ratios for each eruptive deposit were taken from published literature and can be found in Table 1.

Trace Element Geochemistry (Hf, Ti, U, Th)

Results for trace element analyses of individual zircon grains are available in Appendix B. Hf, Ti, U and Th, are especially central in studies of zircon. Hf is an indicator of fractionation, with higher concentrations suggesting growth from more evolved melts from which zircon has already been removed (e.g., Claiborne et al., 2006, 2010a). Ti concentration has been shown to correlate with temperature of crystallization, and Watson and coworkers have calibrated a Ti –in-zircon thermometer (Watson and Harrison, 2005; Watson et al., 2006; Ferry and Watson, 2007; Claiborne et al., 2010a, 2010b). U and Th concentrations in zircons have been widely studied because zircon U-Th-Pb geochronology is so important in geoscience, zircon is a significant reservoir for these heat-producing elements, and Th/U ratios have been shown to correlate with zircon growth environments and with tectonic and lithospheric realms (Hoskin and Schaltegger, 2003; Sawka, 1988; Bea, 1996, O'Hara et al., 2001; Grimes et al., 2007).

Th and U

Th and U concentrations of analyzed zircons are typically subequal and vary by more than two orders of magnitude, from ~10 to >1000 ppm. Th/U ratios are all $\geq$0.3 and reach 2, fairly typical for magmatic zircon (e.g., Hoskin and Schaltegger, 2003). On a log-log plot, seen in Figure 6, U and Th fall within an extended but very well-defined array with a slope slightly greater than 1 (Th/U <1 at low concentrations, >1 at highest concentrations). While data from each eruption plot as part of the same general line, each eruption forms a distinct sub-array. Askja has the lowest concentrations. Half of Oraefajokull data plots immediately next to and parallel with Askja at slightly higher U, while the other half spans the upper extreme of concentrations in the dataset with a slope greater than 1 and higher ($\geq$1). Hekla data also plots close to Askja and Oraefajokull, at slightly higher U and with a steeper slope, and extends to the middle of the combined dataset. The 3100 BP Torfajokull data points cluster in the middle of the dataset, and the other three Torfajokull eruptions (7500 BP, 871 AD, 1477 AD) analyses range from the middle to the upper extreme of U and Th concentrations.

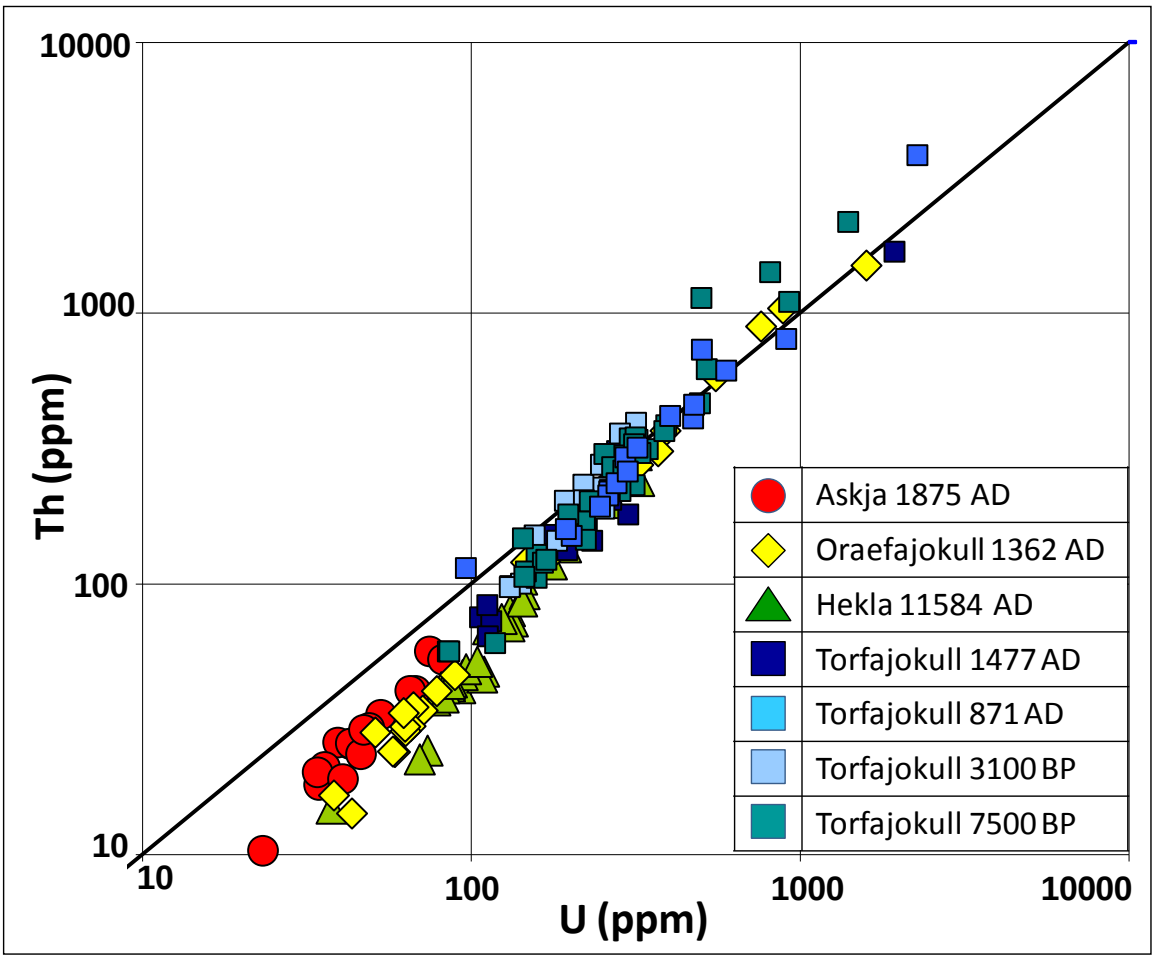

Figure 6

Plot of Th (ppm) vs U (ppm) with logarithmic scales used for the x and y axes. Each spot represents an individual SHRIMP trace element analysis. The bold line dividing the area of the graph represents a Th/U ratio of 1.

Hf concentrations and Hf vs Th/U relationships

Hf is relatively low in analyzed zircons, ranging from about 6000 to 11000 ppm (cf. Grimes et al., 2007; Discussion section, this study). A plot of Th/U vs Hf shows considerable scatter, but the general trend for zircon populations is negative (Figure 7). Askja and Hekla provide the best examples of this negative correlation. Askja spans a range of ~8800-10100 ppm Hf and 0.46-0.75 U/Th, with most points plotting along a weakly linear, negative trend. Hekla spans a greater range of U/Th and Hf than Askja, with Hf concentrations from ~7900-10600 ppm and Th/U from ~0.3-1. Oraefajokull data appear to plot in two distinct groupings, but the general relationship of low-Hf corresponding to high Th/U is still preserved. The group with the highest Th/U ratios (~0.7-1.2) plots at overall-lower Hf concentrations (~6200-8200 ppm), while the group with the lower Th/U ratios (0.3-0.55) plots at overall higher Hf concentrations (~7700-9000 ppm). Data from zircons from each individual eruption at Torfajokull (or Torfajokull as a whole) do not fit the overall-trend defined by Askja, Hekla and Oraefajokull. Zircons from the 7500 BP eruption shows the greatest range of scattered points (Th/U ~0.5-2.25 and Hf ~6800-11300 ppm), while each successively younger eruption shows a tighter clustering of points (3100 BP: Th/U ~0.7-1.3 and Hf ~7900-9000 ppm; 871 AD: Th/U ~0.74-1.4 and Hf ~8600-9500 ppm; 1477 AD: Th/U 0.56-1.1 and Hf ~8800-9800 ppm).

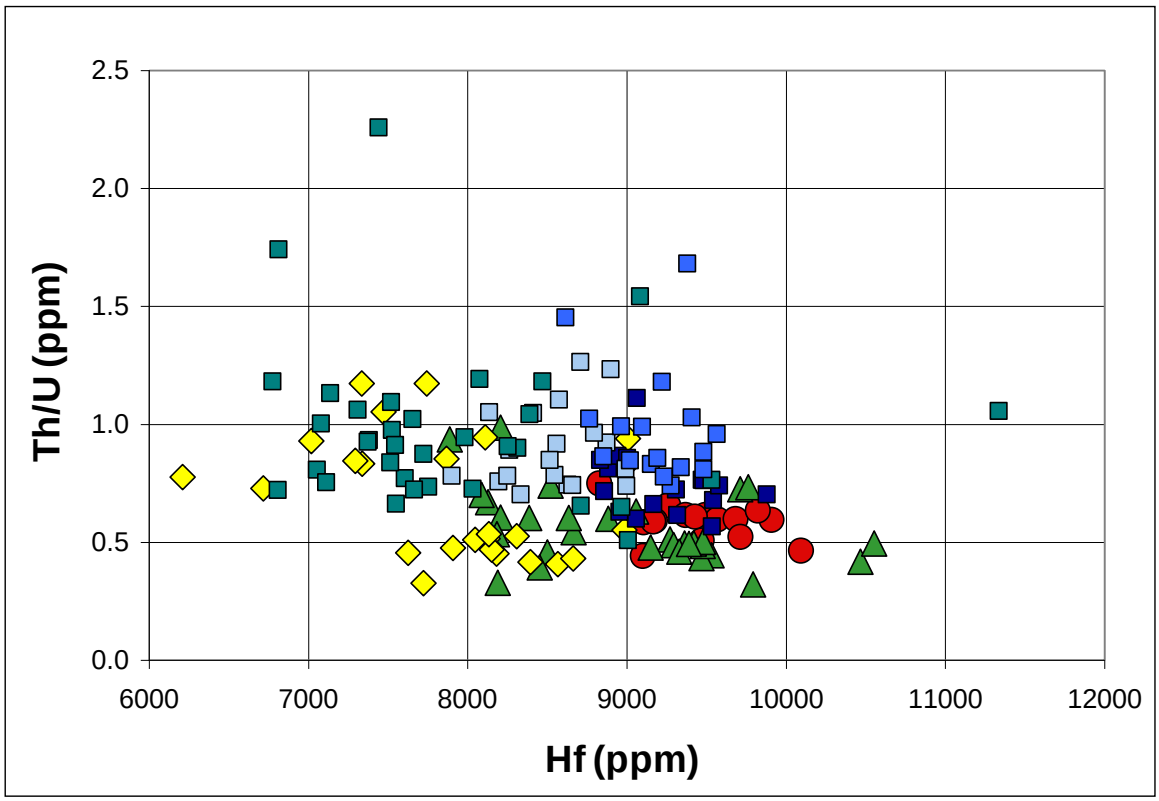

Figure 7

Plot of Th/U vs Hf (ppm). Symbols as in Figure 6. Each spot represents an individual SHRIMP trace element analysis. Hf was selected for the x axis because we consider it to be representative of fractionation (Claiborne et al., 2010a).

Ti concentrations and Ti vs Th/U and Hf relationships

Measured Ti concentrations are relatively high, with most exceeding 10 ppm and highest concentrations exceeding 30 ppm (cf. Fu et al., 2008; Claiborne et al., 2006, 2010a, 2010b). This suggests that most zircons from historic silicic eruptions in Iceland crystallized at relatively high T (see Discussion). Analyses from individual eruptions define unique patterns in a plot of Ti vs Th/U (Figure 8). Askja data, among the highest Ti and lowest Th/U of the dataset, plot nearly vertically with a narrow range of Th/U (0.44-0.75) and a broader range of Ti (19-32 ppm). Oraefajokull analyses plot in two distinct groupings: a tight cluster of points with low Th/U (0.3-0.6) and a modest range in Ti (9-15 ppm), and a larger cluster with higher U/Th (0.7-1.2) and Ti ranging to higher concentrations (9-29 ppm). Like those from Askja and the first Oraefajokull cluster, Hekla zircons have relatively low Th/U (most 0.3-0.7) and a wide range of Ti (7-36 ppm). Taken as a whole, the 3100 BP, 871 AD and 1477 AD Torfajokull datasets overlap to create a weak negative correlation. When considered individually, the 3100 BP eruption has the highest Th/U (0.7-1.3) and Ti (17-26 ppm) concentrations. The 871 AD eruption has the next-highest Th/U ratios (0.75-1, excluding outliers) followed by the 1477 AD eruption (0.56-1.1). The Ti concentrations for the two historical eruptions (871 and 1477 AD) overlap, ranging from ~8-22 ppm. The 7500 BP Torfajokull dataset plots linearly with a positive slope and a wide range of Ti (6-16 ppm, with some higher outliers) and Th/U ratios (0.5-2.3).

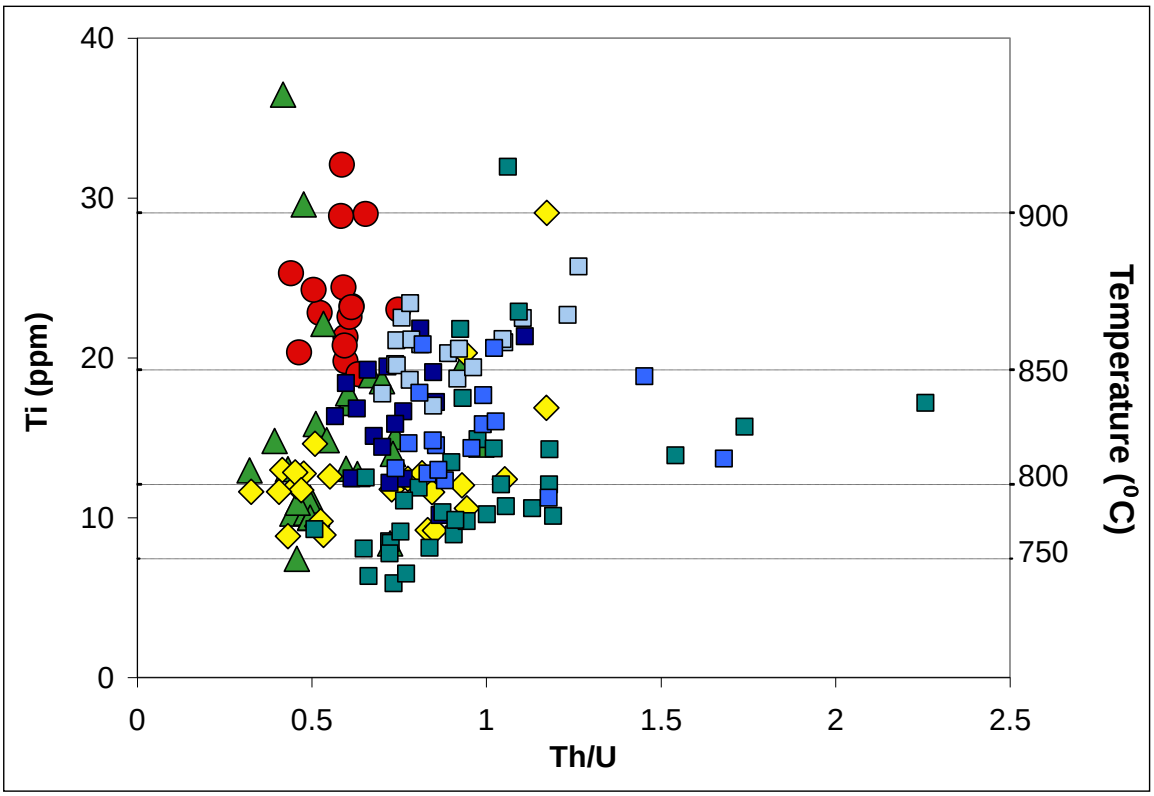

Figure 8

Plot of Ti (ppm) vs U/Th. Symbols as in Figure 6. Temperature estimates are shown on the secondary y-axis (Ferry and Watson 2007). Each point represents a separate SHRIMP analyses.

With the exception of Oraefajokull and interesting inter-population relationships at Torfajokull, zircons from each volcano cluster in a distinct, sub-parallel, linear array with a negative slope on plots of Ti (ppm) vs Hf (ppm; Figure 9). Within these sub-parallel groupings, Askja zircons have the highest Ti (e.g., 25 ppm) for a given Hf (e.g., 9000), followed by Torfajokull (20 ppm) and then Hekla (12 ppm).

When considered together, there is a continuous, monotonic decrease in the Torfajokull dataset, starting with the prehistoric 3100 BP eruption (Ti 23 ppm, Hf 8000 ppm) and transitioning into the historical 871 AD and 1477 AD eruptions (Ti 12ppm, Hf 9500ppm). When considered individually, the prehistoric 3100 BP dataset forms a tight cluster at relatively high Ti (17-25 ppm) and low Hf (8000-9000 ppm), while the historic 871 AD and 1477 AD eruptions plot in overlapping linear arrays. The 7500 BP dataset is far more scattered and exhibits no identifiable trend on this plot.

Oraefajokull dataset is unlike all other samples, with data points forming a sub-horizontal array that plot that spans a wide range of Hf concentrations (from 6000-9000 pmm), but plots (mostly) in a narrow range of Ti concentrations (~9-14 ppm).

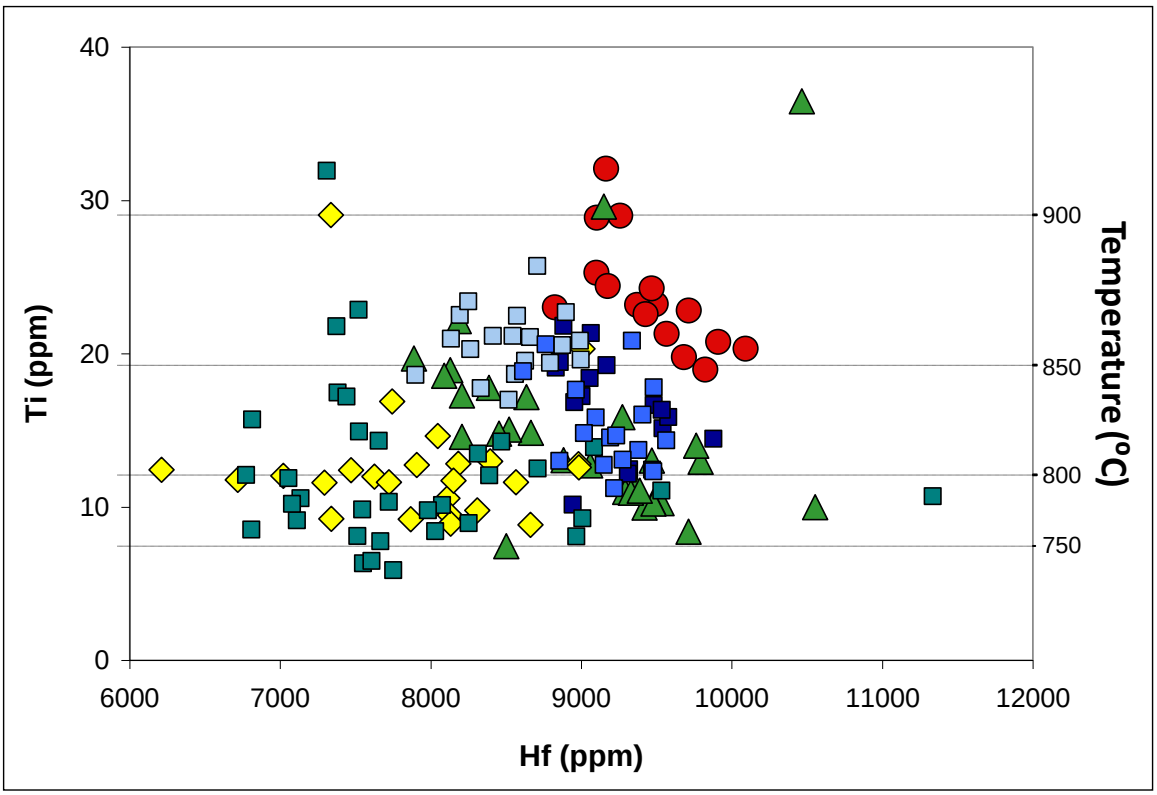

Figure 9

Plot of Ti vs Hf. Symbols as in Figure 6. Hf is representative of fractionation (Claiborne et al., 2006) and Ti is representative of temperature (Watson and Harrison, 2005; Watson et al., 2006; Ferry and Watson, 2007). Temperature estimates are shown on the secondary y-axis (Ferry and Watson, 2007). Each point represents a separate SHRIMP analyses.

Iceland Ti-in-Zircon Estimated Temperature Distribution

Zircon-growth temperatures (estimated using the calculation of Ferry and Watson 2007, SiO_2 activity of 1 and TiO_2 activity of 0.7; see Methods) for all data collected in this study are plotted in Figure 10. Calculated temperatures for 158 separate analyses fall in the range of 730-930 °C (mean ~815 °C, median ~810 °C).

Individual eruptions have distinctly different Ti-temperature distributions. Of all of the eruptions considered, Askja has the highest overall Ti and estimated temperatures. The mean temperature is 875 °C which is 60 °C higher than the total mean and 20 °C higher than zircon saturation for our analyzed sample.[24] The Hekla temperature distribution is similar to the distribution of the entire dataset, but it is dominated by intermediate temperatures. The mean estimated temperature at Hekla is 820 °C, just 5 °C higher than the total mean, but 100 °C lower than zircon saturation for this population. The temperature distribution for Oraefajokull zircons is very similar to that for all of Iceland, but with a narrower range of temperatures. The mean estimated temperature at Oraefajokull is 800 ºC, which is 15 ºC below the total mean and 130 °C lower than zircon saturation for this population.

The estimated temperature distribution for Torfajokull (prehistoric and historic) is nearly identical to that of our total Iceland dataset, but skewed to slightly lower temperatures. The thermal history of Torfajokull through time as estimated from zircons is thus very similar to the thermal record that we see recorded in zircons from across the different thermal and tectonic settings of Iceland. As seen in the total Iceland compilation, individual eruptions from Torfajokull distinctive Ti-temperature distributions. The 1477 AD Torfajokull temperature distribution is similar to that of all of Iceland, but is dominated by higher temperatures. The mean estimated temperature from the 1477 Torfajokull eruption is 830 ºC, which is 15 ºC higher than the total Iceland and total Torfajokull average and 60 °C lower than zircon saturation for this population. The 871 AD Torfajokull temperature distribution spans a far narrower range of temperatures than the total Icelandic compilation. The estimated mean temperature for 871 AD is 770 ºC, which is 45 ºC lower than the total Iceland and total Torfajokull means and 100 °C lower than zircon saturation for this population. The temperature distribution for the 3100 BP eruption at Torfajokull is different from both the distribution of all Icelandic temperatures from this study,

[24] Askja zircon were separated from a sample of "layer D" pumice by Dr. Ilya Bindeman, while we calculated saturation temperatures from a separate sample of layer D pumice.

and also from the combined Torfajokull dataset. There is a narrow temperature range (800-900 ºC), and higher temperatures dominate over lower temperatures. The mean estimated temperature is 860 ºC, which is 40 ºC higher than the total mean, 50 ºC higher than the overall Torfajokull mean, and 60 ºC lower than the zircon saturation temperature for this population. The temperature distribution for the 7500 BP eruption at Torfajokull resembles that of both the total Iceland dataset and the prehistoric-historic Torfajokull dataset. The main difference is the under-representation of higher temperatures. The mean estimated temperature for Torfajokull 7500 BP is 795 ºC, which is 20 ºC lower than the total mean, 10 ºC lower than the Torfajokull average, and 25 ºC lower than the zircon saturation for this population.

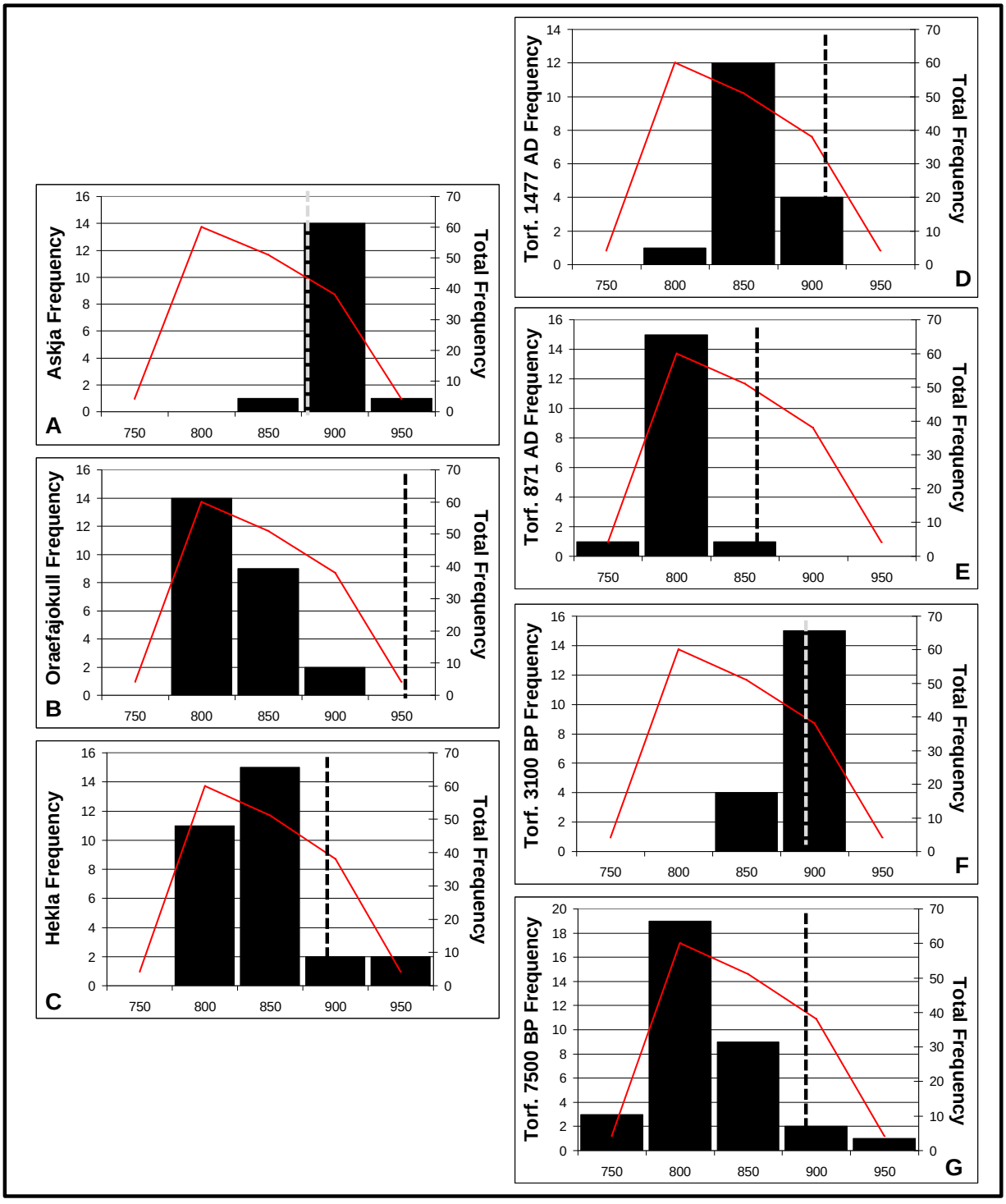

Figure 10

Distribution of estimated Ti-in-zircon temperatures (Ferry and Watson 2007). A:Askja; B: Oraefajokull; C: Hekla; D: Torfajokull 1477 AD; E: Torfajokull 871 AD; F: Torfajokull 3100 BP; G: Torfajokull 7500. The dashed line on each histogram shows the approximate zircon saturation temperature. The red line shown on each plot, provided for ease of comparison, represents the distribution of estimated temperatures for all zircon analyses from all eruptions. Bins span 50 ºC and are labeled by their upper bounding temperature.

Rare Earth Elements (REE)

There is great variability in REE abundances and patterns among zircon populations from different Icelandic eruptions. Zircons from all samples show typical chondrite-normalized zircon REE patterns, with a general increase from low LREE to high HREE and positive Ce and negative Eu anomalies (Figure 11). Torfajokull 3100 BP and 1477 AD analyses plot notably lower than those for 871 AD and 7500 BP, and Oraefajokull is divided into two distinct groupings with patterns of similar shape but different absolute abundances.

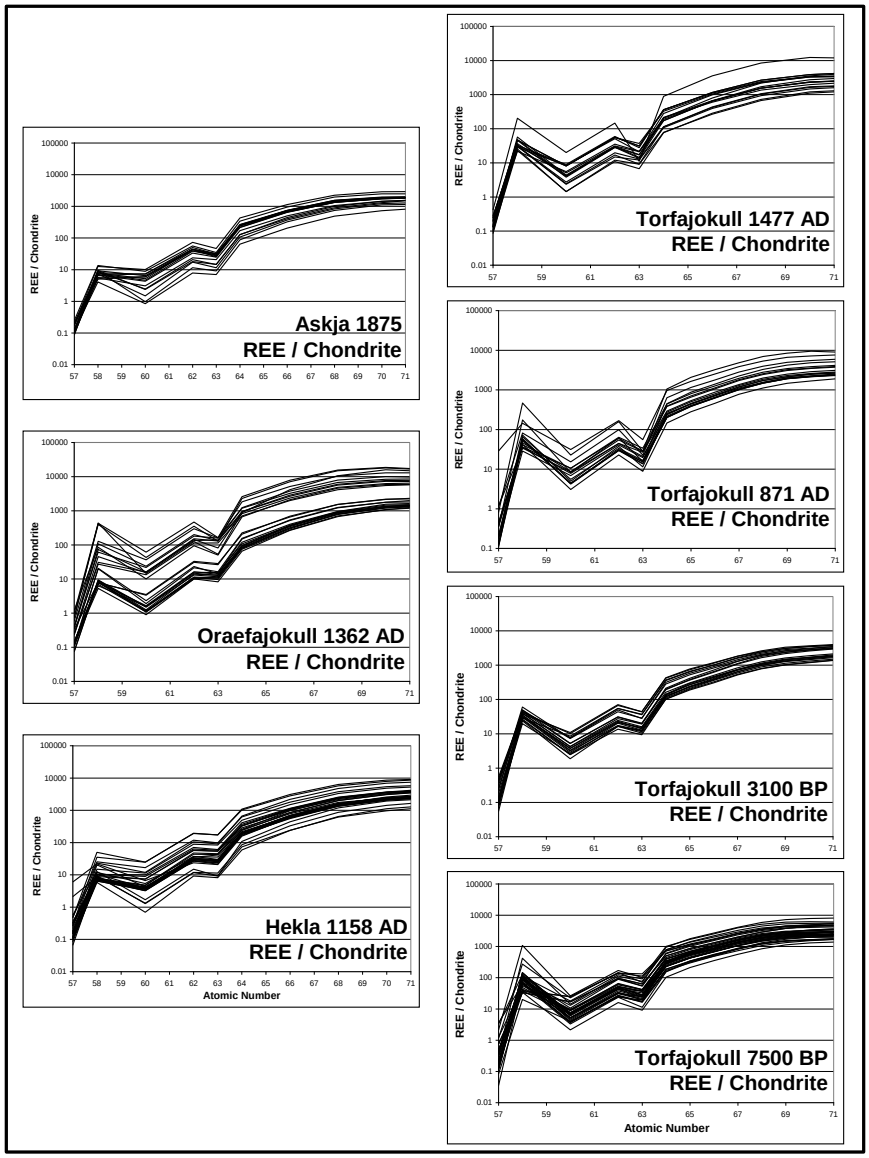

Figure 11

Chondrite Normalized REE.

While major trends can be recognized on plots of chondrite-normalized REE, this type of plot also masks significant diversity that exists in detail. We employed two different methods to emphasize the population-to-population and grain-to-grain REE variability. First, we calculated average Icelandic REE abundances using all REE data collected in this study (see Appendix B) and re-plotted all analyses after normalizing them to these concentrations (Figure 12). Second, we plotted ratios of Yb/Nd, Gd/Nd, and Yb/Gd vs Hf to show enrichment of heavy REE (HREE) relative to light REE (LREE), middle REE (MREE) relative to LREE, and HREE relative to MREE, respectively (see Figure 13). These plots of REE ratios clearly distinguish the eruptions from which zircons were collected.

REE Normalized to the Average Icelandic Zircon Composition

Plots of REE normalized to the average-Icelandic REE composition (Figure 12) reveal that the greatest variability within individual zircon populations is related to LREE, likely due to variability in Ce and Nd (which may be due to inclusions of LREE-rich minerals or melt). Eu anomalies also contribute to variability seem within zircon populations.

These same plots of REE normalized to the average-Icelandic REE composition (REE/Av) also uncover interesting subtleties that make each population distinct from the rest of the Icelandic dataset (Figure 12). Most REE concentrations in Askja zircons are lower than average Iceland REE, falling in a normalized range of 0.1-1. All Ce concentrations fall well-below the Icelandic average, and Eu is also very low for all analyses. The range of REE/Av values in Oraefajokull zircons spans two orders of magnitude (0.1-10). Eleven of the 25 analyses plot clearly above the Iceland average for the full suite of REE while the other 14 plot clearly below the Icelandic average. The upper grouping has an overall concave-down (inverted-bowl) shape and the upper grouping has an overall concave-up (bowl) shape. The range of REE/Av values in Hekla zircons spans two orders of magnitude (0.1-10). There is a great deal of variability in the LREE-HREE range related to Ce, Eu and Nd. Twenty seven of the 29 total Ce analyses fall below the Icelandic average. Four analyses (for the full range of REE) are notably lower than the rest of the Hekla dataset. The general shape of these four samples is an overall LREE-HREE concave-down (bowl) shape that resembles the pattern in one of the Oraefajokull groupings. With one anomalous exception, all REE/Av values for Torfajokull 1477 AD are

relatively low and fall within one order of magnitude (0.1-1). The range of REE/Av values for Torfajokull 871 AD zircons spans two orders of magnitude (0.1-10). For Eu, 15 of 17 points plot lower than the Icelandic average. Most REE/Av values from Torfajokull 3100 BP zircons are low and limited to a range of one order of magnitude (0.1-1). The greatest variability is for Ce (of 19 analyses, 14 show a positive Ce anomaly and 5 have negative anomalies) though all Ce abundances fall below the Icelandic average. The range of REE/Av values from 7500 BP Torfajokull zircons spans two orders of magnitude (0.1-10). Thirteen analyses plot above the Icelandic average, and 21 plot below.

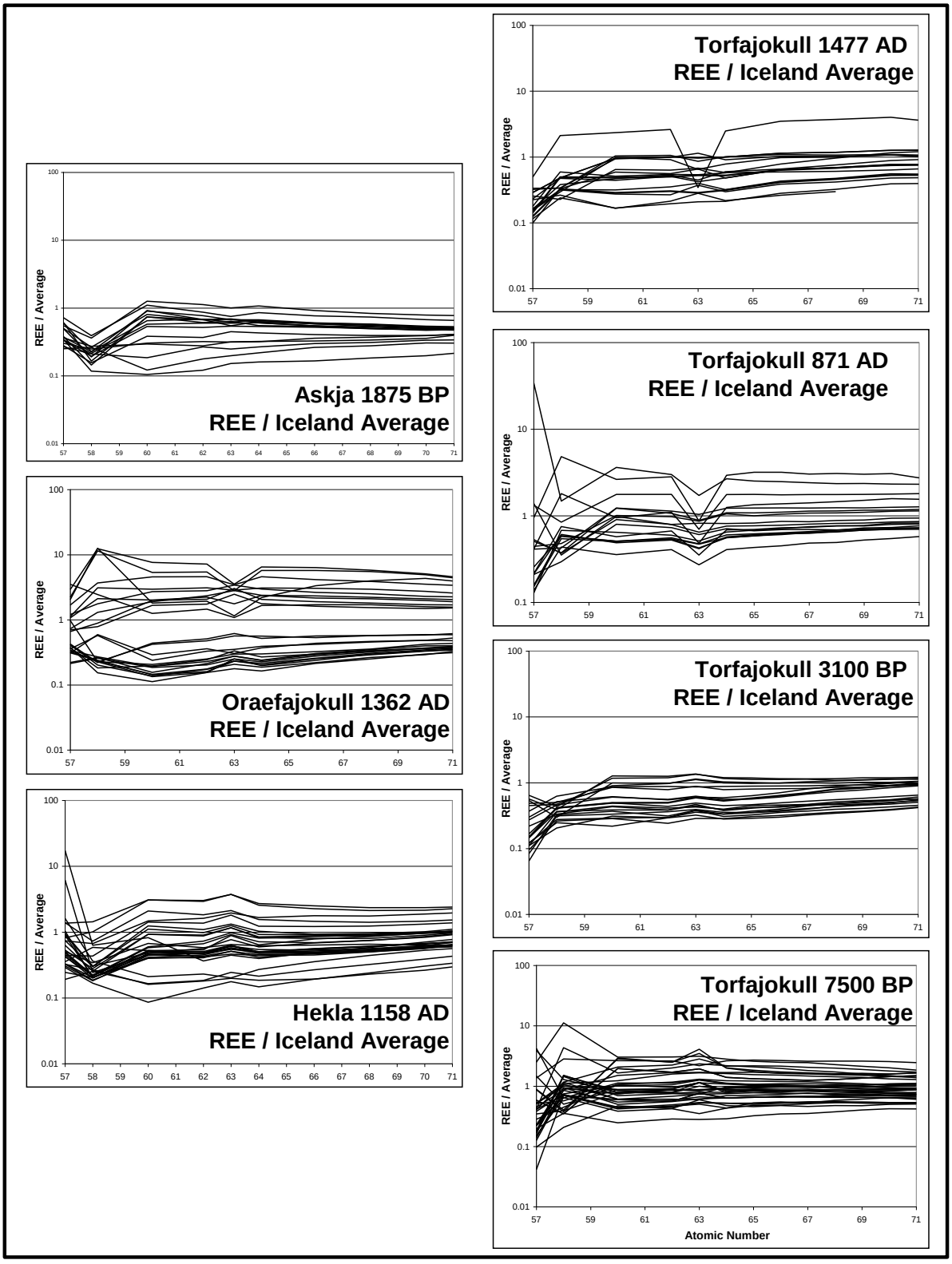

Figure 12

Iceland-Average-Normalized REE. The "Iceland-Average" REE values used to normalize can be found in Appendix B. The variability seen in La (number 57) is due to low abundances combined with analytical error.

Relative Enrichment of LREE, MREE and HREE

Overall, there is a positive correlation between Yb/Nd (HREE/LREE) and Hf, indicating enrichment in HREE relative to LREE with increasing fractionation (increasing Hf; Figure 13). The individual eruption that shows this the most clearly is Torfajokull 7500 BP, which has a continuous, gently positive slope. The slope established by Torfajokull 7500 BP seems to be continued to higher levels of fractionation (higher Hf) by Torfajokull 3100 BP and Torfajokull 1477 AD. Oraefajokull also displays the shallow positive sloping trend at lower degrees of fractionation (lower Hf), but at approximately 8000 ppm there is a sudden break in slope, and the enrichment of HREE relative to LREE becomes much more pronounced.

There is also a positive correlation between Yb/Gd (HREE/MREE) and Hf (Figure 13). The eruption that shows this trend the most clearly is, again, Torfajokull 7500 BP, which has a continuous, gently positive slope (which seems to be continued by Torfajokull 871 AD). Oraefajokull, Hekla and Askja also display this trend for a portion of their data points. Oraefajokull has a gentle, continuous positive slope until approximately 8500 ppm Hf, and then there is a break in slope and much more pronounced enrichment in HREE over MREE. Hekla maintains the overall positive slope for most of its data points, but there are a few anomalous points that break from the trend (3 high Yb/Gd at lower Hf, 1 especially low Yb/Gd at high Hf). Eleven of the 16 Askja data points plot between 8500-10500 ppm Hf with a shallow positive slope, but the remaining 5 points scatter at higher Yb/Gd with no obvious correlation with Hf.

The trend of Gd/Nd (MREE/LREE) vs Hf data is poorly defined compared to those for Yb/Nd and Yb/Gd (Figure 13). However, Oraefajokull zircons are clearly enriched in MREE relative to HREE with increasing fractionation: as Hf concentrations in Oraefajokull zircons increase from ~6000 ppm to ~9000 ppm, there is a gradual and continuous increase in Gd/Nd. The break in slope that is observed in plots of Yb/Gd and Yb/Nd is absent in this plot. Though there are a few analyses that break the trend, Torfajokull 871AD also exhibits an increase in Gd/Nd with increasing Hf, with a slope that is sub-parallel to that of Oraefajokull.

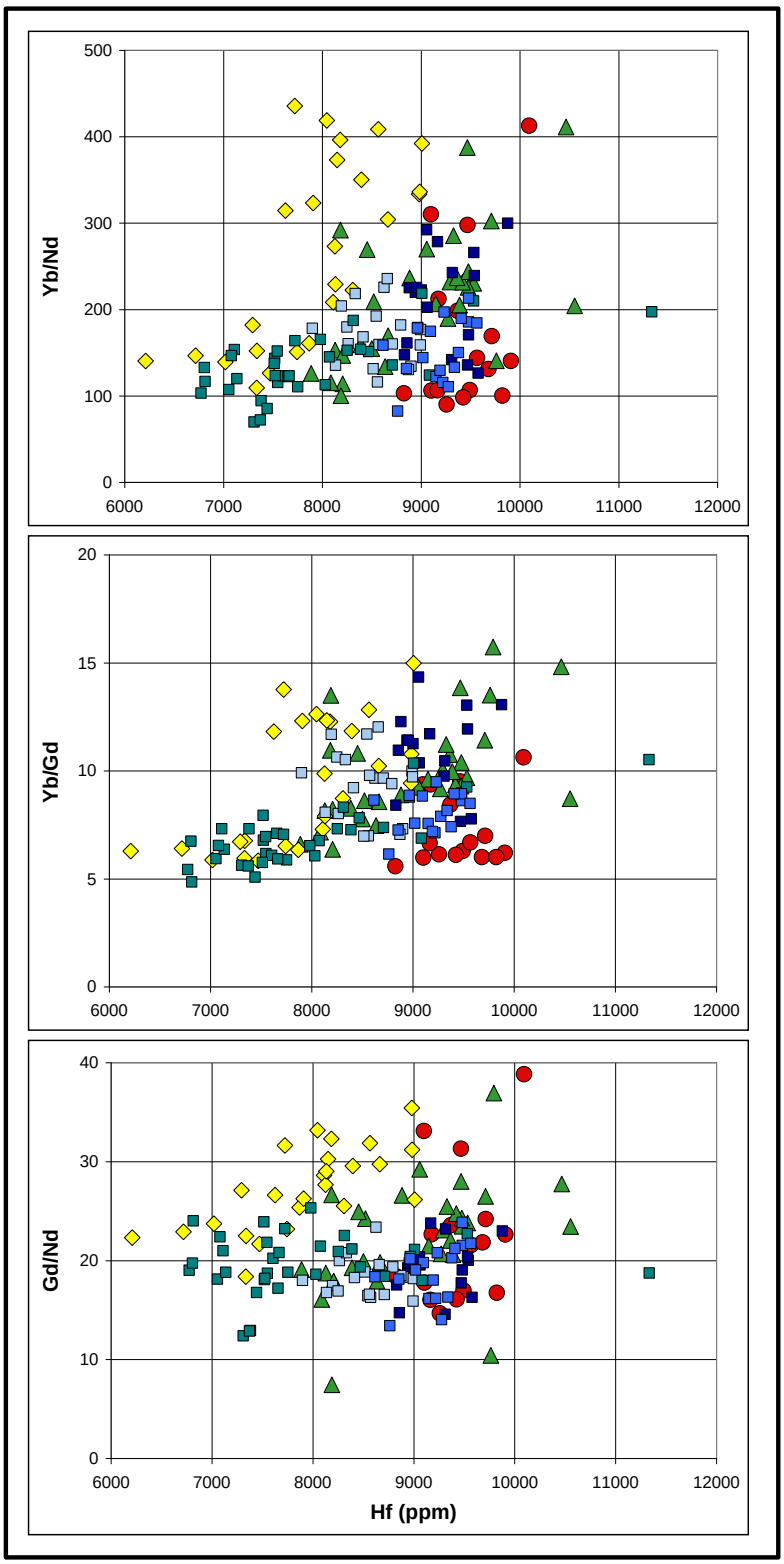

Figure 13

Variation in REE ratios with increasing fractionation (ppm Hf). The specific ratios we examine are HREE/LREE shown with Yb/Nd, HREE/MREE shown with Yb/Gd and MREE/HREE shown with Gd/Nd. Each data point represents an individual SHRIMP analysis. Symbols as in Figure 6.

CHAPTER V

DISCUSSION

We evaluate our Icelandic zircon data set in terms of its relevance to three primary issues:

1. Origins of silicic magma in Icelandic magmatic systems: A primary goal of this study is to test two dominant hypotheses for silicic petrogenesis in the Icelandic oceanic setting: fractional crystallization of parental mafic magma and partial melting of hydrothermally altered crust.
2. Possible correlations between the history of silicic magmas as recorded in zircon with the tectonic and thermal settings in which they formed: we will evaluate whether zircon from the different volcanoes, with their different settings, have unique compositional or chronological "fingerprints," and if so, we will explore possible explanations for their distinctiveness.
3. Comparison of compositions of Icelandic zircon compositions with zircons from other settings worldwide: we ask the question, "Are Icelandic zircons globally distinct in their elemental compositions, or are they similar to analyzed zircons from other settings?"

Origins of Silicic Magma in Icelandic Volcanic Systems

We consider four processes that may be responsible for generating silicic magmas in Iceland:

1. Segregation of silicic, interstitial melt from a crystal-rich mush (cf. Bachmann and Bergantz, 2004)
2. Partial melting of relatively silicic rock and subsequent segregation of silicic melt from the unmelted residue[25]
3. Partial melting of relatively mafic rock and subsequent segregation of silicic melt from the unmelted residue
4. Fractional crystallization of basaltic magma

[25] While this option is somewhat unsatisfying because it does not explain how the parent rock came to be silicic (potentially pods of felsic melt generated during fractional crystallization that solidify before eruption, etc.), it is undoubtedly an important possibility to explain the occurrence of rhyolite in Icleand.

We consider these four possibilities to be distinct processes for generating eruptible silicic magma. However, it is difficult to distinguish between partial melting of silicic and basaltic crust by heating as a consequence of injection of new magma and remobilization of interstitial liquid in a mush by injection of new magma. For this reason we adopt the language of Jonasson (2007) and refer to all three of these possibilities as "near solidus" differentiation. We refer to the alternative petrogenetic process as "near-liquidus" fractional crystallization. Even with the creation of these two broad categories, it is still possible that overlapping characteristics blur the distinction between near-solidus and near-liquidus petrogenesis in the rock record (Bachmann and Bergantz, 2004). We use multiple lines of evidence from each zircon population to attempt to distinguish between near-solidus and near-liquidus petrogenetic differentiation. The evidence we consider includes:

1. Elemental zoning: Zircons grown in a fractionally crystallizing magma body (near-liquidus) and zircons grown in interstitial liquid in a crystal mush (near-solidus) are both likely to be monotonically, normally zoned, assuming that there is no important recharging and heating during the lifetime of the crystal. Pre-existing zircons from the source that are entrained in an anatectic (near solidus) magma are likely to show discontinuities in their elemental zoning. Xenocrystic crystals that are introduced into magma during its ascent – including those entrained by hotter magmas encountering crystal mush (Claiborne et al., 2010b) - are likely to exhibit reverse zoning. Very low Th/U in zones (<~0.1; especially with low Ti) may imply a subsolidus history; if in grain interiors, this would indicate entrainment of zircon during extraction of anatectic melt, or during ascent of magma through crystallized, zircon-bearing rock.
2. Comparing saturation temperature with growth temperature: Zircons erupted in a saturated or near-saturated magma are consistent with growth in a fractionally crystallizing magma (near-liquidus) or in interstitial liquid in a mush (near-solidus). Zircons erupted in an undersaturated magma may have been introduced to the erupted magma via contamination of ascending magma by pre-existing crystal mush or solidified rock (cf. Claiborne et al., 2010b).
3. Ages: U-Th dating reveals the timing of zircon growth preceding eruption. If zircon ages fall within a continuous, or clustered, age distribution that approaches

eruption age (within ~thousands of years), it is possible that the zircons grew together in a fractionally crystallizing magma (near-liquidus) or in the interstitial melt in a crystal mush (near-solidus). If, however, zircon ages are discontinuous, with significant (tens of k.y.) gaps in the growth record, it is possible that multiple episodes of growth contributed zircons to the erupted population. This can be explained by zircon entrainment in an ascending magma via disaggregation of an extant crystal mush, or by retention of zircons during partial melting of pre-existing rock (near-solidus).

4. Morphology: Discrete, distinctive (typically CL-dark) grain interiors and rounded zone boundaries and grain edges provide evidence of zircon being introduced to magmas in which they did not originate, as might happen during partial melting of silicic or basaltic rock (near-solidus) or entrainment of pre-existing crystals in an ascending magma. The absence of these features suggests zircon growth in a fractionally crystallizing magma (near-liquidus) or in interstitial liquid in a crystal mush (near-solidus). Textural evidence for altered cores may suggest sub-solidus processes, indicating that crystals were entrained either in anatectic magma (near-solidus) or as contaminants in ascending fresh magma.

Evidence for each volcano is discussed below and summarized in Tables 4 and 5.

Table 4

Ti and Hf zoning in Individual Zircon Grains

Zircon Grain	Ti interior (ppm)	Ti Edge (ppm)	Ti Zoning	Hf interior (ppm)	Hf Edge (ppm)	Hf Zoning	Consistent Zoning?[26]
ASKJA							
1	23.2	20.7	Normal	9494	9909	Normal	Yes
2	29.0	25.3	Normal	9260	9101	Normal	Yes
3	21.3	24.4	Reverse	9569	9178	Reverse	Yes
4	19.8	24.2	Reverse	9684	9371	Reverse	Yes
5	22.8	23.0	Reverse	9715	8827	Reverse	Yes
7	32.1	19.0	Normal	9167	9824	Normal	Yes
HEKLA							
6	14.8	12.9	Normal	8454	9794	Normal	Yes
9	13.0	17.8	Reverse	8883	8387	Reverse	Yes
12	14.6	13.0	Normal	8207	9468	Normal	Yes
14	7.4	36.5	Reverse	8502	10466	Normal	No
21	11.2	10.9	Normal	9363	9329	~same	~
22	14.8	19.7	Reverse	8666	7889	Reverse	Yes
ORAEFAJOKULL							
3	12.0	11.6	Normal	7019	7294	Normal	Yes
4	29.1	12.8	Normal	7336	8982	Normal	Yes
5	20.3	12.8	Reverse	9008	8183	Reverse	Yes
7	12.4	12.7	~same	7471	7908	Normal	~
14	8.9	11.6	Reverse	8133	7723	Reverse	Yes
15	16.9	13.0	Normal	7744	8396	Normal	Yes
17	9.2	11.7	Reverse	7339	8150	Normal	No
19	10.6	12.0	Normal	8110	7627	Reverse	No
TORFAJOKULL 14777							
5	10.2	15.1	Reverse	8942	9541	Normal	No
6	12.4	14.4	Reverse	9472	9879	Normal	No
8	12.5	17.2	Reverse	9318	9003	Reverse	Yes
14	19.4	16.3	Normal	8858	9535	Normal	Yes
871 AD							
1	17.6	12.7	Normal	8964	9151	Normal	Yes
2	20.6	17.8	Normal	8763	9482	Normal	Yes
3	11.2	12.3	Reverse	9220	9481	Normal	No
4	13.7	15.8	Reverse	9379	9096	Reverse	Yes
6	18.8	13.0	Normal	8615	8854	Normal	Yes
9	14.7	16.0	Reverse	9194	9408	Normal	No
3100 BP							
1	20.8	19.5	Normal	8993	8627	Reverse	No
7500 BP							
2	5.9	10.7	Reverse	7753	11335	Normal	No
7	6.3	11.1	Reverse	7550	9533	Normal	No
8	11.9	9.3	Normal	7055	9008	Normal	Yes
15	7.7	8.1	Reverse	7666	8967	Normal	No
21	14.9	8.9	Normal	7525	8253	Normal	Yes
22	17.2	12.1	Normal	7442	8389	Normal	Yes
24	8.1	9.8	Reverse	7514	7982	Normal	No

[26]"Consistent zoning" means that both Hf and Ti display the same of zoning pattern (both normal, or both reverse).

Table 5

Summary of Zircon Features Considered in Silicic Petrogenesis Investigation

Eruption	Ti zoning: norm./rev./?[27]	Hf zoning: norm./rev/?[28]	Ti-Hf zoning consistency: (yes/no/?)[29]	Ti-in-zircon Temp. range (°C)	Zircon saturation Temp. (°C)	Discrete interiors	Rounded interiors	Rounded exteriors	Range of Ages (ka)
Askja 1875 AD	3/3[30]	3/3	6/0	850-910	855	None	n/a	Few-to-none	Unavailable
Oraefajokull 1362 AD	4/3/1	5/3	5/2/1	770-900	930	Many	Many	Few-to-none	0-20, 35
Hekla 1158 AD	4/2	3/2/1	4/1/1	750-930	920	Few	None	Few-to-none	0-30, 45
Torfajokull 1477 AD	1/3	3/1	2/2	780-865	890	Some	Some	Many	0-20, 45
871 AD	2/4	5/1	4/2	740-800	880	Some	Some	Some	10-30
3100 BP	0/1	1/0	0/1	840-885	920	Some	Few-to-none	Few-to-none	15-40
7500 BP	3/4	7/1	3/4	730-910	925	Some	Few-to-none	Few-to-none	10-15, 35-40

[27] Normal = higher Ti in interior than at edge; the "?" indicates that measured concentrations were too similar to define zoning as normal or reverse
[28] Normal = lower Hf in interior than at edge; the "?" indicates that measured concentrations were too-similar to define zoning as normal or reverse
[29] By "consistency" we mean that both Ti and Hf show the same type of zoning (either both normal or both reverse)
[30] We conducted multiple SHRIMP trace element analyses on 6 grains from Askja (3 +3). The same scheme applies to the other eruptions.

Icelandic zircons erupted in recent (primarily historic) eruptions of silicic magma are generally relatively small (average length 132 μm), relatively sparse (maximum of tens of grains separated from ~5 kg material), and display concentric zoning that is subtle in CL-brightness contrast when compared to magmatic zircons that have been described elsewhere (e.g. Hoskin et al., 2003; Claiborne et al., 2010a, 2010b; Belousova et al., 2006). Despite these broad generalizations, there are critical details on a population-to-population and grain-to-grain scale that provide insight into different magmatic histories. For instance, Oraefajokull has a notable abundance of zircons with dark, discrete and rounded interiors, some of which display a mottled texture that is absent in all other zircon populations examined. Also, some Oraefajokull zircons display sector zoning, a feature that is absent in all other populations. Zircons from the historic eruptions of Torfajokull (1477 AD, 871 AD) are also noteworthy because there are a number of examples of rounded grain rims. In contrast, zircons from Askja are largely euhedral with no rounding, an absence of dark, discrete centers, and very-low CL brightnest contrast zoning.

Because of the small size of zircon grains and the zones visible in CL, as well as the limited number of crystals separated from each sample, we have limited data on interior-to-edge changes in composition. Nonetheless, individual samples consistently reveal complexity in intra-crystal compositional patterns. For each sample, some grains display normal zoning with Ti and Hf while other grains display reverse zoning. Furthermore, on an intra-grain scale, there are instances of grains being normally zoned with Ti but reversely zoned with Hf (or vice versa). The absence of simple, systematic change in individual grains (e.g., consistent normal zoning, consistent reverse zoning) suggests that eruptions examined in this study did not sample zircons grown in uniformly evolving magmas that experienced pure, simple, monotonic fractionation. While simple fractional crystallization may be broadly responsible for petrogenesis of magma for particular eruptions, it was not a process operating in isolation. Rather, our complex zoning results imply complex histories, likely involving zircon entrainment in new melt (liberated from disaggregated melts or partially melted rock), or injection of new, hot magma into a pre-existing melt altering the signatures of evolution preserved within each individual zircon grain.

Calculated zircon saturation temperatures (855-930 °C) and estimated zircon growth temperatures (730-930 °C) are relatively high for Icelandic zircons compared to zircons from continental settings (Claiborne et al., 2010a, 2010b; Fu et al., 2008; Harrison et al., 2007; Harrison and Watson 1983; further discussion below). The high saturation temperatures can be

explained by high concentrations of Zr in the melts (see Table 2; Watson and Harrison, 1983). There are a few instances of zircon growth temperatures exceeding zircon saturation temperatures (all but one grain at Askja; two at Hekla; at least one from each eruption at Torfajokull), and a few instances of zircon growth temperatures extending well below saturation temperatures (all zircons at Oraefajokull and a number from Hekla and Torfajokull 871 AD and 3100 BP), but generally zircon growth temperatures are closely related to zircon saturation temperatures. These temperature findings are broadly consistent with zircon growth in the melts with which they are erupted, but there are critical discrepancies that suggest introduction and entrainment of zircons that experienced a different growth history. Estimated growth temperatures that are significantly below saturation temperature may suggest the introduction of zircons from a partially-melted rock or entrainment of zircons from a disaggregated crystal mush, as these zircons may have crystallized to solidus or near-solidus conditions. Estimated growth temperatures that are significantly above saturation temperature may suggest the introduction of zircons into the host melt from a more-mafic melt with a higher concentration of Ti (via magma mixing or mingling).

While zircon populations from each individual eruption have a unique age distribution falling between 0 and 50 k.y. before eruption, the majority of zircon growth in Iceland appears to predate eruptions by 10 to 30 k.y. Each population (with the exception of Torfajokull 871 AD) has at least on zircon grain that is significantly older than the rest of the population (in the 35-50 ka range). It is also typical for each population to have a few zircon that are younger than 10 k.y. (the majority of zircon at Oraefajokull, but none for 871 AD or 7500 BP eruptions at Torfajokull). The discontinuity of ages suggests that the zircon populations that are erupted in a single magma likely represent antecrysts (and potentially xenocrysts) that are the result of multiple episodes of growth.

Observations of Zircon from Individual Eruptions

Askja

The majority of zircon growth at Askja took place at temperatures higher than saturation. This suggests that they were grown in a magma other than the one in which they were erupted, then introduced through open system processes (perhaps grown in an evolving, high-Ti,

originally mafic magma then introduced via magma mixing). Other observations appear to be inconsistent with this mode of origin, though. Zircon morphology suggests that crystal fractionation (near-liquidus) or growth in interstitial melt (near-solidus) might be reasonable petrogenetic hypotheses. The majority of grains at Askja lack dark discrete centers suggestive of previous episodes of growth, exhibit simple concentric zoning with low-brightness contrast in CL, and are free of morphological signs of resorption (Figure 3, Appendix A).

Oraefajokull

All zircons analyzed from Oraefajokull have estimated growth temperatures that fall below the zircon saturation temperature estimated for the pumice from which they were collected. With the exception of one date of 35 ka, all U-Th ages are <20 ka and most are ~5-10 ka (Figures 4 and 5). The clustering of ages is suggestive of one relatively young episode of zircon growth, potentially in a fractionally crystallizing basalt (near-liquidus) or interstitial liquid in a crystal mush (near-solidus), but the older age introduces the possibility of open-system processes that entrained older zircons from a disaggregated crystal mush or partially-melted host rock. The presence of dark, rounded grain interiors (Figure 3, Appendix A) supports the hypothesis of zircon contamination in the erupted melt, and young ages of these rounded interiors suggest that the contaminating material was magmatically active in the same cycle as the magma that erupted in 1362 (e.g., zircon entrainment in a new melt involved in silicic petrogenesis at Oraefajokull).

Hekla

All but one zircon analyzed from Hekla have estimated growth temperatures that fall below the zircon saturation temperature estimated for the pumice from which they were collected. The limited U-Th data set includes a single age at 43 ka and two possibly discrete populations at <8 and 18-28 ka (Figures 4 and 5). The apparent breaks age in are suggestive of introduction of older zircons from partially melting crust (near-solidus) or a disaggregating mush, but more zircon grains must be collected and analyzed for Hekla before we can confidently remark on the continuity, or discontinuity, of zircon growth. The majority of zircon grains from Hekla has concentric zoning with very low CL brightness contrast and lack signs of resorption, all suggestive of growth in a fractionally crystallizing magma (near-liquidus) or an

interstitial melt (near-solidus; Figure 3 and Appendix A). There are a few examples, though, of discrete, dark centers that might represent separate episodes of growth, suggesting a component of open-system petrogenesis in the history of this magma.

Torfajokull

Combined observations of zircons from historic (1477 AD, 871 AD) and prehistoric (3100 BP, 7500 BP) eruptions at Torfajokull suggest complex petrogenetic behavior for silicic magma at this volcanic center. Zircons from the 7500 BP eruption yielded inconclusive evidence for petrogenetic process (limited evidence could be interpreted to support near-liquidus or near-solidus differentiation), while observations of zircons from the two younger eruptions strongly support a hypothesis of partial melting (near-solidus) contributing significantly to the generation of silicic magma at Torfajokull.

Zircons from the 1477 AD eruption grew in a period that spanned from near-eruption to ~45 ka (Figure 4 and 5). Most of the documented zircon growth occurred between 0 and 12 ka, with the two oldest grains (~22, ~45 ka) perhaps introduced to the system by partial melting (near-solidus) of pre-existing rock, or entrainment of zircon from a disaggregated mush. This hypothesis of input by partial melting or entrainment of zircons in foreign magma is supported by zircon morphology and zoning (Figure 3, Appendix A). There are a few zircon grains that have dark, discrete centers that are possibly relics from an earlier episode of growth. There are also a number of sub-equant grains with rounded edges, a morphology that suggests that these grains experienced an event that prompted resorption, such as introduction into a new magmatic environment. Zircons from the 3100 BP eruption show a very similar story in terms of discontinuous ages (5 ag ~8 to 18 ka, 2 older at ~3800 ka) and zircon morphology.

Zircons from the 871 AD eruption of Torfajokull are very similar to those erupted in the 1477 AD eruption. U-Th ages place the dominant zircon growth somewhat earlier, between ~11 and 28 ka, without any older outliers (Figures 4 and 5). Zircons show high brightness-contrast zoning in CL images suggesting compositional change throughout the time of growth, and many grains have dark, discrete centers that possibly indicate early growth under different conditions (Figure 3, Appendix A). There are also many grains with rounded edges that are suggestive of resorption. All of this evidence supports partial melting (near solidus) or entrainment of zircons in a foreign magma influencing the silicic petrogenetic history at Torfajokull. It also strongly

suggests that the 1477 AD and 871 AD eruptions sampled similar magma and zircons, though the time of growth appears to differ.

Zircons from the 7500 BP eruption of Torfajokull date between ~16 and 42 ka in what appears to be a continuous episode of growth (Figures 4 and 5), perhaps by fractional crystallization (near liquidus) or growth in an interstitial liquid (near-solidus) during very slow cooling (<200 °C over >25 k.y.). Zircon morphology is also suggestive of fractional crystallization (near-liquidus) or growth in an interstitial liquid (near-solidus). The majority of zircon grains from this eruption lack dark discrete centers and are mainly characterized by very low CL brightness contrast concentric zoning (Appendix A).

Relation between Zircon Compositions and Tectonic Setting

Zircons from volcanoes in different tectonic settings in Iceland appear to have distinctive compositional characteristics. The monotonically decreasing Ti vs.Hf trends are aligned in such a way that, for a given Hf value Askja (on-rift) has the highest Ti (and implied temperatures), followed by Torfajokull (propagating rift tip), followed by Hekla (transitional to rift), followed (mostly) by Oraefajokull, with the lowest Ti at a given Hf concentration (off-rift; Figure 14). To put it another way, for the same degree of fractionation, zircons growing in magmatic systems nearest the rift are growing at higher temperatures. For a given Ti concentration, Askja (on rift) has the highest Hf, followed by Torfajokull 3100 BP-1477 AD (propagating rift tip), followed by Hekla (transitional to rift), followed (mostly) by Oraefajokull (off-rift).

The Ti vs. Hf (~temperature and fractionation) trends recorded by Torfajokull 7500 BP and Oraefajokull zircons completely stray from the sub-parallel, linear, pattern that we see in on- and near-rift volcanoes. Temperatures estimated for Torfajokull 7500 BP grains and Oraefajokull cover a wide range of both temperature (Ti) and fractionation (Hf) with no apparent correlation. The thermal-fractionation history recorded by these zircons suggests that the off-rift Oraefajokull zircons and the transitional-to-rift 7500 BP Torfajokull zircons were growing in magmas that experienced a different sort of petrogenetic history than magmas at on-rift Hekla, younger Torfajokull and Askja.

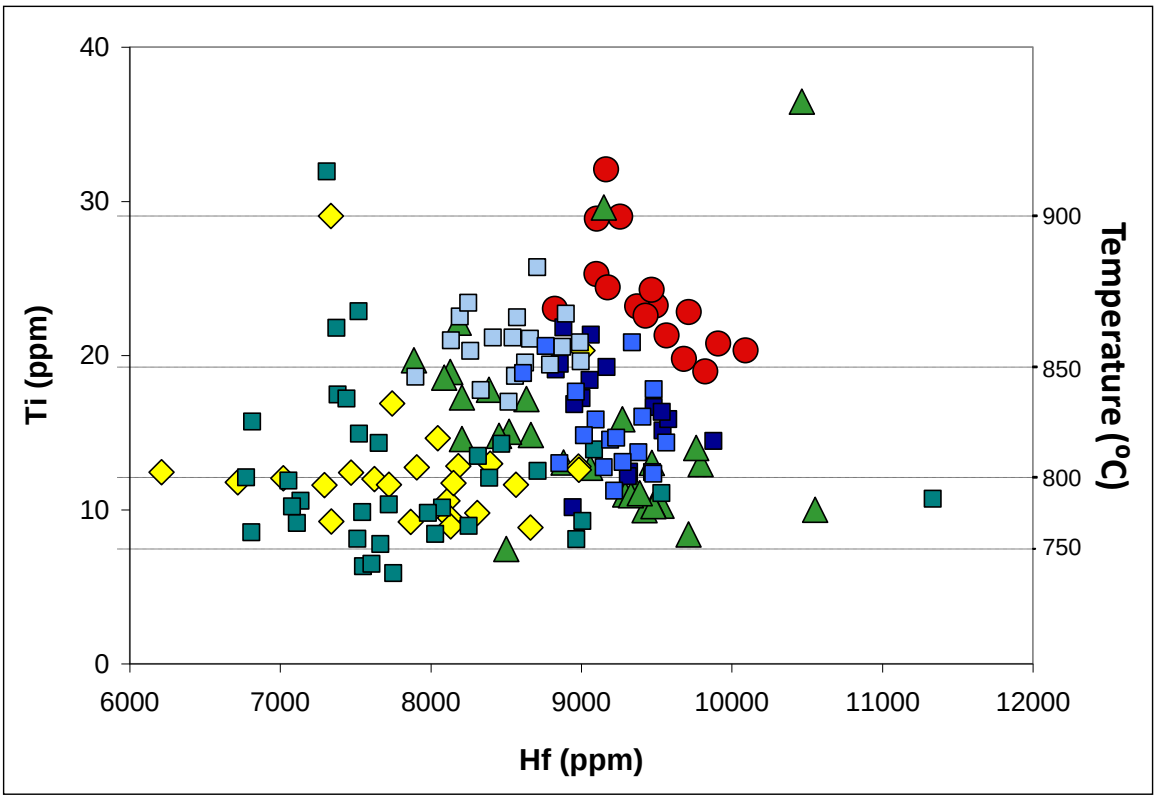

Figure 14

Ti vs Hf and tectonic setting. Ti (temperature) and Hf (degree of fractionation) are correlated with tectonic setting.

Iceland zircon in a global context

To place Icelandic zircons in a global context we compare them to zircons from other silicic systems that we (Vanderbilt University and collaborators) study: active continental rift generating new oceanic lithosphere (Alid volcano [granophyre enclave, rhyolite; Flanagan, pers. comm. 2010], Eritrea; Lowenstern et al., 1997, 2006); onset of continental extension (Colorado River extensional corridor; Highland Range [rhyolite; Colombini, 2009], Nevada; Spirit Mountain batholith [granite-quartz monzonite; Claiborne et al., 2006]; Peach Spring Tuff [rhyolite-trachyte; Pamukcu, 2010]; Faulds et al., 2001, Walker et al., 2007;]; subduction-related continental arc volcano (Mount St. Helens [dacite]; Claiborne et al., 2010b). We also use summaries of global zircon compositions provided by Grimes et al. (2007) for comparison.

We find that zircons from Alid are consistently the most similar to our Icelandic zircons, often with overlapping trace element concentrations and ratios, and plotting with similar patterns. These relationships are particularly pronounced in Th/U ratios (Figure 15) and in plots of To vs Hf (Figure 16) and U vs Hf (Figure 17). The other continental zircons used for comparison often display limited similarities (some overlapping concentrations and ratios), but are overall distinct from the Icelandic and Alid zircon populations (much wider ranging trace element geochemistry, data plotting in different patterns). On plots that distinguish between continental-and MORB-type zircons (Figure 18; Grimes et al., 2007), Icelandic and Alid zircons are confined to a narrow segment of the continental field in close proximity to the MORB-type boundary, with a very restricted range of composition. The other continental zircons that we are using for comparison (Mount Saint Helens, MSH; Highland Range, HR; Peach Spring Tuff, PST; Spirit Mountain Batholith, SMB) overlap with the Icelandic dataset, but extend to much higher Hf and U/Yb and are more typical of continental-type zircons.

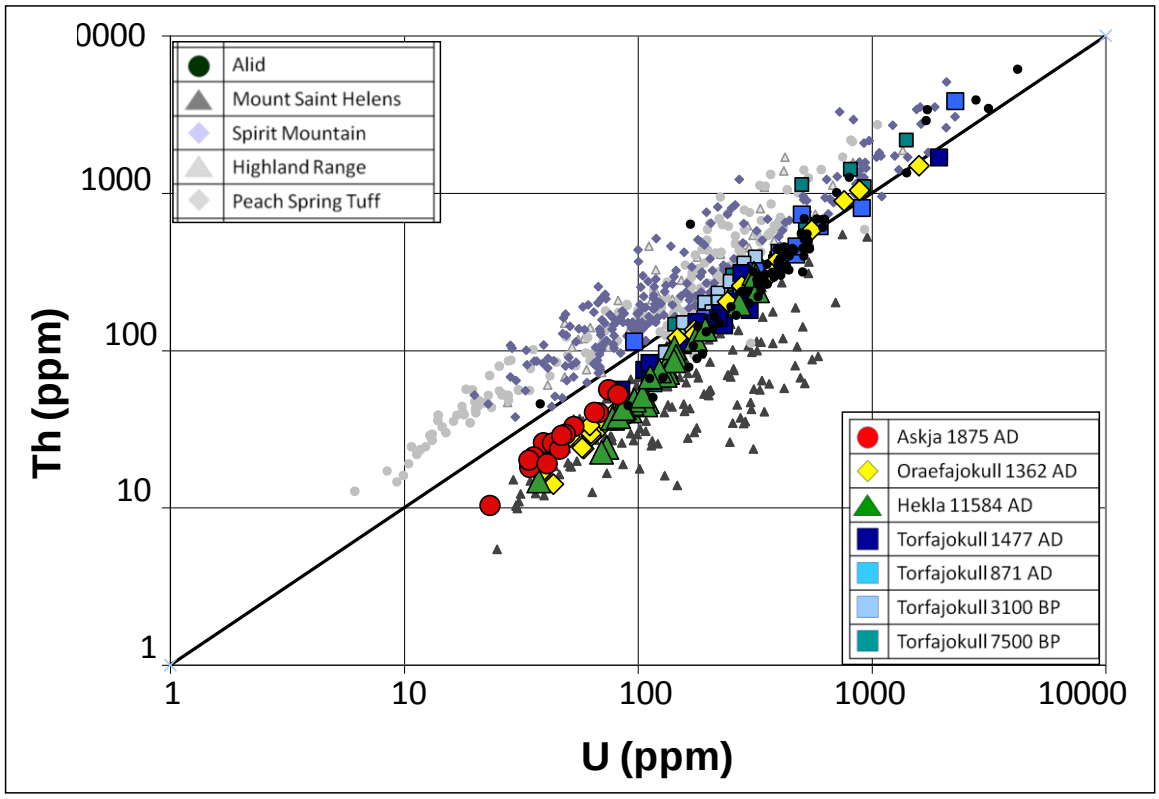

Figure 15

Comparison of Th vs U for Icelandic zircons and zircons from Alid, Mount St. Helens, Spirit Mountain, the Highland Range and the Peach Spring Tuff. Iceland and Alid zircons have Th/U ratios that are generally ≤1 and plot with in a linear pattern on a log-log plot with a slope very slightly >1. Zircons from MSH also have Th/U ratios <1 but extending to considerably lower values than Iceland zircons and plotting with a more-scattered, less-linear pattern. Th/U ratios of zircons from the intracontinental settings (HRL, PST, SMB) plot in a distinct field with higher (>1) Th/U ratios.

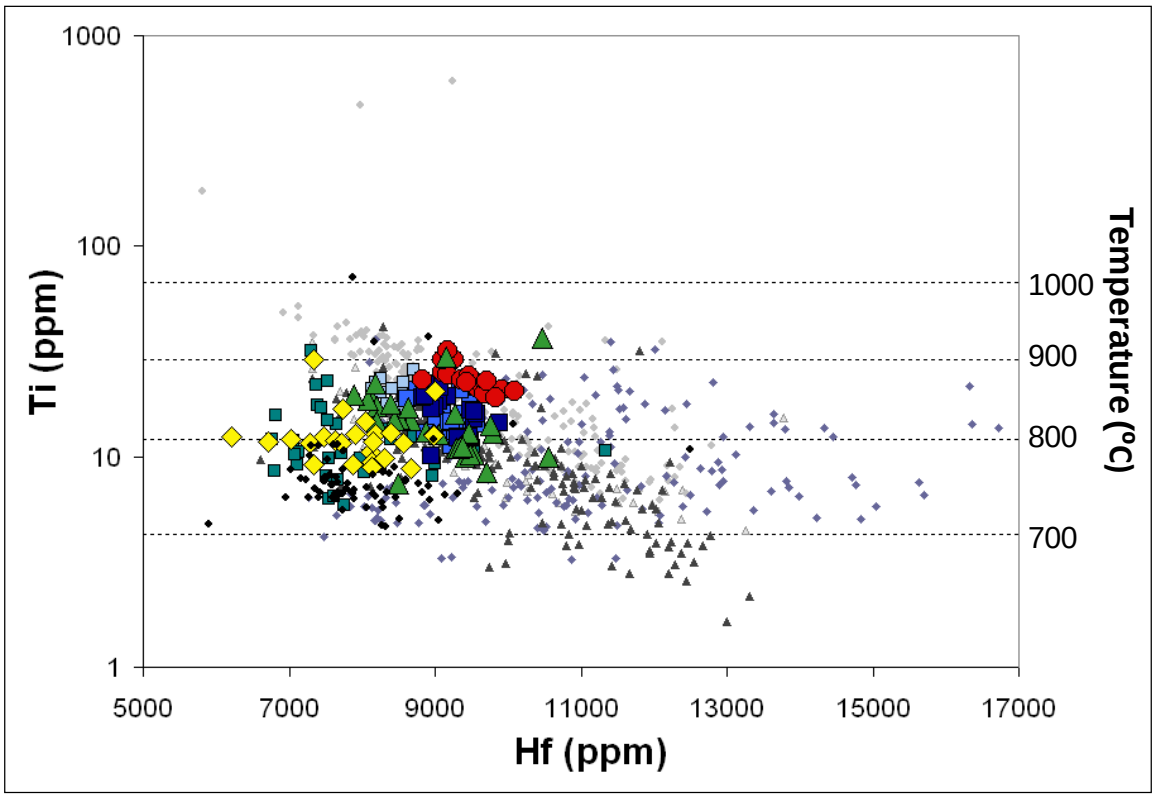

Figure 16

Comparison of Ti vs Hf for Icelandic zircons and zircons from Alid, Mount St. Helens, Spirit Mountain, the Highland Range and the Peach Spring Tuff. Symbols are as in Figure 15. Icelandic zircons plot in a fairly constrained range with relatively high Ti (~10-40 ppm) and low Hf (~6000-11000 ppm). Alid zircons are the most similar to Icelandic zircons overall using these elements for comparison, plotting in the same range of Hf at the lower extreme of the Iceland Ti range. Zircons from all of the other systems considered for comparison (MSH, PST, HLR, SMB) overlap to some degree with Icelandic zircons, but record much higher Hf concentrations (up to ~17000 ppm for SMB) and much lower Ti (down to ~1.5 ppm for MSH). The Icelandic and Alid zircons plot in a relatively constrained cluster while zircons from the other systems extend semi-linearly with a negative slope.

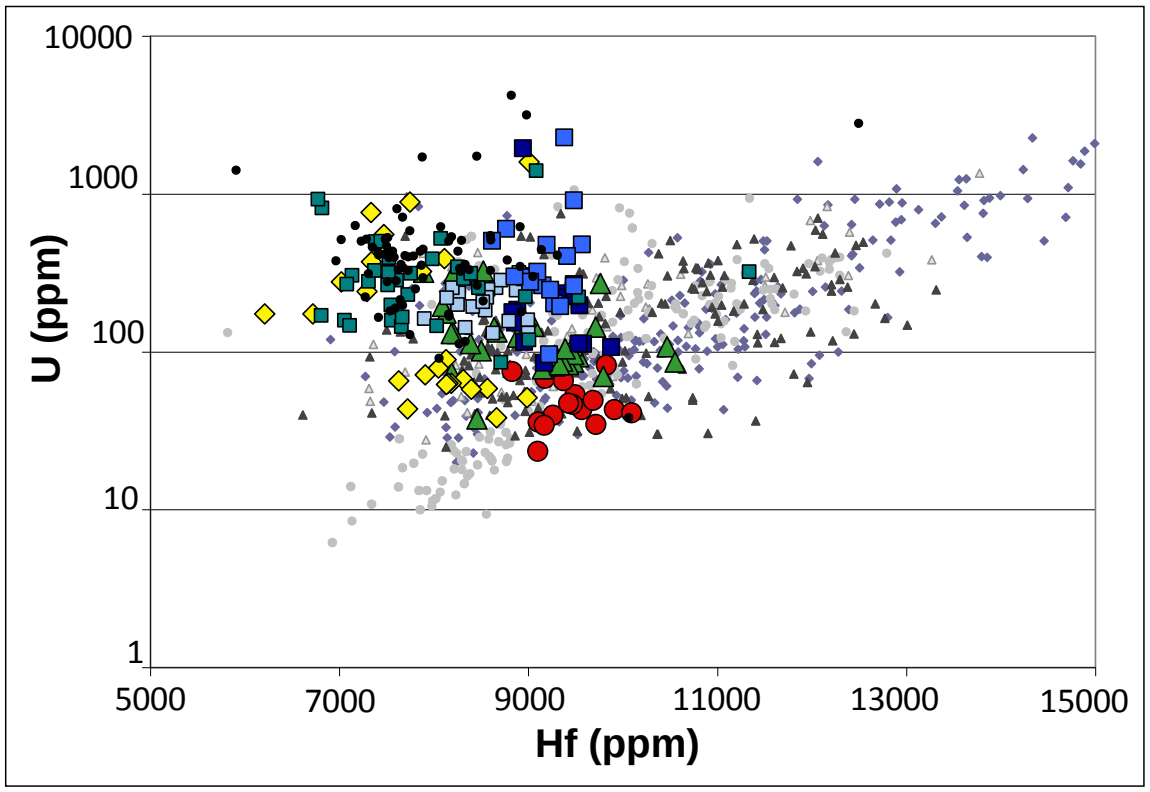

Figure 17

Comparison of U vs Hf for Icelandic zircons and zircons from Alid, Mount St. Helens, Spirit Mountain, the Highland Range and the Peach Spring Tuff. Symbols are as in Figure 15. Icelandic zircons display a wide range of U (~20-2000 ppm) despite their relatively narrow range of Hf. Alid plots in the same general cluster as Iceland. PST, MSH, SMB and HRL collectively plot in a semi-linear pattern with a positive slope that is counter (nearly perpendicular) to the semi-linear pattern with a negative slope that is formed by Icelandic and Alid data points. The linear trend created by MSH, HRL, PST and SMB covers the same general U range as Iceland and Alid, but covers a far greater range of Hf (~7000-15000 ppm).

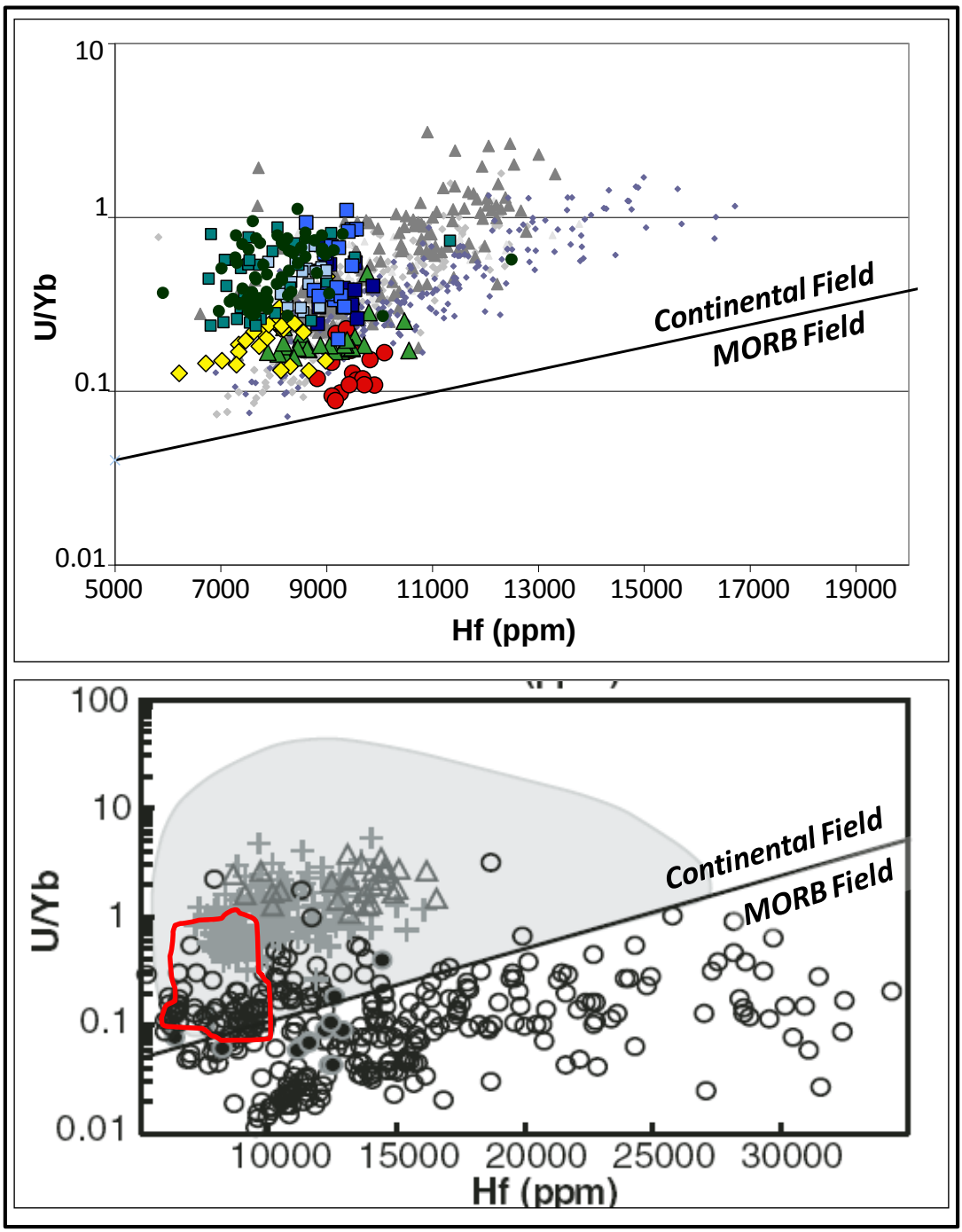

Figure 18

Distinguishing between Continental- and MORB-type zircons on plots in the style of Grimes et al., 2007.
This combination of trace elements (U/Yb vs Hf) is suggested by Grimes et al. (2007) as a means of distinguishing zircons based on their environment of formation: continental or mid-ocean ridge. By plotting Icelandic zircon on this empirical diagram we are placing silicic rocks from a distinctive oceanic setting in a global continental-oceanic context. Top: comparison of U/Yb and Hf from Icelandic zircons and zircons from Alid, Mount St. Helens, Spirit Mountain, the Highland Range and the Peach Spring Tuff. Symbols as in Figure 15. Bottom: Icelandic compositional range overlain on a plot taken (and modified) from Grimes et al., 2007. See original figure for explanation of symbols.

CHAPTER VI

CONCLUSIONS

This study is the first to use zircon as a lens for examining silicic petrogenesis in Iceland. Zircons from recent (primarily historical) eruptions are small (average length ~130 μ) and sparse (maximum of tens of grains separated from ~5 kg material), but record a great deal of information about the magmas in which they were grown and erupted. U-Th dating of Icelandic zircons reveals ages that predate eruption by approximately 0-50 ka, with most ages falling in a range of 5-30 ka. Although most zircon growth substantially predated eruption, the range of ages is far less than has been found in arc and continental interior settings, where zircon ages hundreds of thousands of years older than the time of eruption are common (e.g., Claiborne et al., 2010b; Vasquez and Reid, 2002; Brown and Fletcher, 1999). Icelandic zircons have Ti concentrations that range from ~10-30 ppm (corresponding to estimated growth temperatures of ~750-900 °C), which is relatively high compared to the Ti average of 4.5 ppm for zircons from felsic intrusive rocks (global) and 14.6 ppm for rhyolite (global) presented by Fu et al. (2007). Ti concentrations and implied temperatures correlate with expected thermal conditions for the tectonic settings of the volcanoes. For a given Hf concentration (representative of degree of fractionation) the Askja (on-rift, near hotspot) zircons have the highest measured Ti and estimated temperature followed by Torfajokull (propagating rift tip), Hekla (transitional to rift) and Oraefajokull (off-axis).

Multiple lines of evidence such as zircon grain morphologies, U-Th ages, and the absence of simple, systematic change in individual zircon grains (e.g., consistent normal zoning, consistent reverse zoning) suggest that the grains did not grow from magma that experienced pure, simple, monotonic fractionation. While simple fractional crystallization may be broadly responsible for petrogenesis of magma for particular eruptions, it was not a process operating in isolation. Rather, our complex results imply complex histories, likely involving zircon entrainment in new melt (liberated from disaggregated crystal mushes or partially melted rock), or injection of new, hot magma into a pre-existing melt altering the signatures of evolution preserved in individual zircons.

PART II

MODELING MAGMA CHAMBER EVOLUTION LEADING TO THE PEACH SPRING TUFF SUPERERUPTION, ARIZONA, CALIFORNIA AND NEVADA

CHAPTER I

INTRODUCTION

Silicic volcanism in general, and supereuptions[31] in particular, raise questions about the mechanisms by which magma bodies destabilize and erupt. It is unclear if a system will evolve to a condition where eruption is inevitable or if outside triggers are essential to eruption. If a magmatic system is indeed capable of internally triggering an eruption, it is important to better understand the critical mechanisms and physical controls involved.

This study is an attempt to understand pre-eruptive magmatism and the destabilization of magma bodies using the Peach Spring Tuff (PST) as a model system. A two-pronged attack is adopted to assess the internal factors that lead to magmatic instability: petrologic and geochemical analysis of the tuff itself, and geochemical and thermodynamic modeling of the evolving system. A modified version of MELTS (updated from Ghiorso and Sack, 1995) is used to explore the effects of variable pressure, volatile content and mode of crystallization on the stability of the pre-eruptive Peach Spring Tuff magma body. Data used in the model were collected from the PST itself, and all modeled results are compared to petrologic observations and geochemical analyses. In this way we gain insight into the physical response to chemical evolution within a large, evolving body of silicic magma.

[31] Supereruption: a volcanic eruption that ejects material in excess of 10^{15} kg or 450 km^3 dense rock equivalent (Sparks et al., 2005; Self, 2006).

CHAPTER II

GEOLOGIC BACKGROUND

The Peach Spring Tuff (PST) is a rhyolitic ignimbrite erupted in the early Miocene, 18.66 +/- 0.03 Ma ($^{40}Ar/^{39}Ar$ sanidine, Ferguson and McIntosh in prep, using newly accepted age for Fish Canyon Tuff standard; cf. previous estimates of ~18.5 +/- 0.2 Ma, Nielson et al., 1990, Miller et al., 1998). The tuff is exposed from the Colorado Plateau, across the Colorado River Extensional Corridor (CREC) and into extended and unextended terranes of the Mojave Desert (Glazner et al., 1986; Figure 1). The tuff is generally welded and has a typical thickness of ~20 to 50 m, with outcrops as thick as 150 m in the Piute Mountains, CA, and thinner sheets in distal exposures. Discontinuous outcrops of tuff have been correlated across the region using relative stratigraphic position, absolute ages, and a distinctive mineral assemblage of abundant sanidine, subordinate plagioclase, sphene and biotite with minor to absent quartz and accessory zircon, apatite and allanite (Glazner et al., 1986; Gusa et al., 1986; Buesch and Valentine, 1986; Gaudio et al., 2003). Regional correlation of the tuff has led to conservative estimates of a pre-extensional lateral distribution of ~35,000 km^2 and an erupted volume of more than 640 km^3 dense rock equivalent ([DRE]; Glazner et al., 1986; Gusa et al., 1987; Buesch 1992), which classifies the PST as a supereruptive deposit (Sparks et al., 2005; Self, 2006).

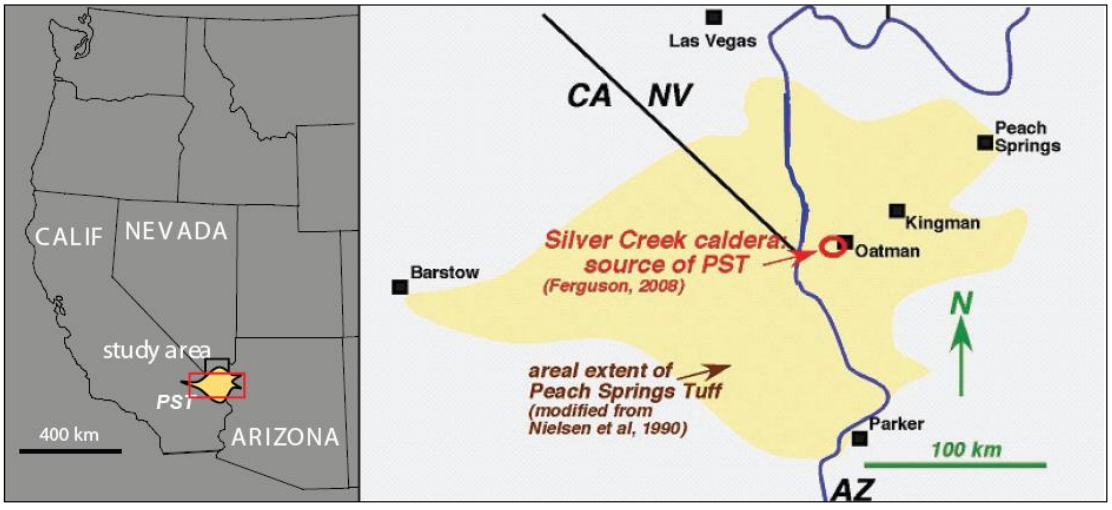

Figure 1

Regional distribution of the Peach Spring Tuff.

The PST eruptive source long went unrecognized, though anisotropy of magnetic susceptibility (AMS) studies constrained the eruptive source to the CREC in the vicinity of the Arizona-Nevada-California intersection (Figure 1; Wells and Hillhouse, 1986) and variable thickness of the deposits indicated that the source was likely in or near the Black Mountains (Young and Brennan, 1974; Glazner et al., 1986). The Silver Creek Caldera has recently been identified as the PST vent based on age and phenocryst assemblage of intracaldera and outflow tuff, and consistency with previously described regional patterns of thickness and flow directions (Ferguson, 2008; Ferguson and McIntosh in prep). This deeply-incised caldera, located ~10 km northwest of Oatman, AZ, in the western Black Mountains, is filled by a single-cooling unit of ash-flow tuff that lacks a preserved top and confirmed base. Exposed caldera margins and intracaldera tuff have been intruded by granites that are approximately the same age (18.5 +/- 0.5 U-Pb zircon) as the PST (Thorson, 1971; DeWitt et al., 1986; Ferguson, 2008). The identification of the Silver Creek Caldera as the probable eruptive source of the PST provides fresh opportunities for investigation of this supereruption.

CHAPTER III

METHODS

Fieldwork

Samples were collected at well-exposed outcrops of PST located in, and at variable distances from, the Silver Creek Caldera (see Figure 2 and Table 1 for locations and sample descriptions). To the extent possible, the pumice and fiamme (welded pumice clasts) sampled are unaltered and have a glassy component. We did not analyze bulk-tuff because abundant lithic fragments (from chamber wall, conduit, and substrate of ash flow) and mechanical fractionation of particles during emplacement make them unreliable representatives of magmatic composition.

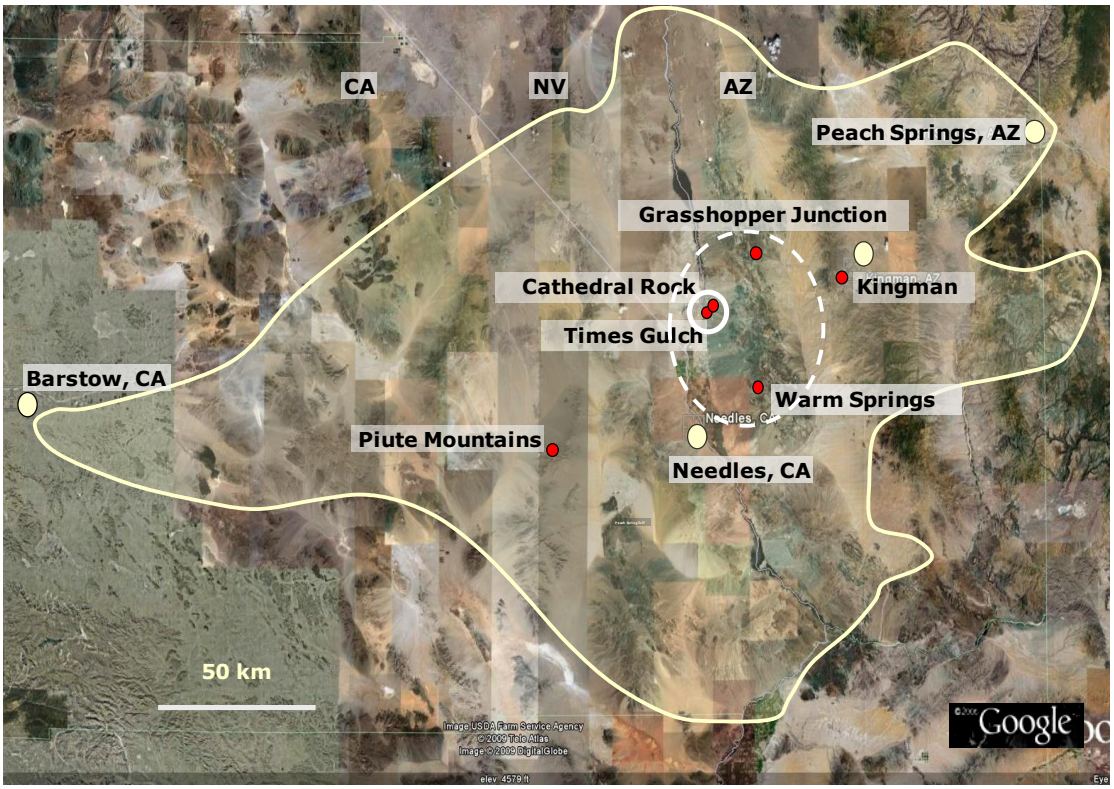

Figure 2

Map of the PST distribution and approximate locations of sampling sites. Yellow ovals mark the approximate location of towns (labeled), for reference. Red circles mark the approximate locations of sample sites (labeled). The solid white circle indicates the general location of the Silver Creek Caldera and the zone we refer to as the intracaldera. The dashed white line shows the approximate boundary for what we refer to as the proximal outflow. The light yellow boundary that encompasses most of the area shown indicates the approximate known-distribution of the PST.

Table 1

Locations and Descriptions of Peach Spring Tuff Samples

Sample Name	SiO_2 (wt. %)	Sample Type	Sample Coordinates	Location Description	Location Designation
CRWPST	66.1	Fiamme	11S 0731653 3882577	Silver Creek Caldera, Cathedral Rock, west; near bottom (AZ)	Intracaldera
CRWPST-2A	68.7	Fiamme	11S 0731656 3882579	Silver Creek Caldera, Cathedral Rock, west; near top (AZ)	
PSTG-1C	68.2	Fiamme	11S 0730332 3881149	Silver Creek Caldera, Times Gulch (AZ)	
28571-PST-BF	62.9	Fiamme	11S 0733407 3881328	Silver Creek Caldera, Times Gulch; narrow canyon (AZ)	
28556-PST-P1	69.3	Pumice	11S 0744585 3865481[32]	Warm Springs Wilderness Area, east; non-welded capping unit (AZ)	Proximal Outflow
WSWPST-1	57.6	Magmatic Enclave	11S 0739814 3864385	Warm Springs Wilderness Area, west (AZ)	
WSWPST-2A	75.1	Pumice	11S 0740155 3864007	Warm Springs Wilderness Area, west; white gully (AZ)	
WSWPST-2B	71.0	Pumice			
WSWPST-2D	76.1	Pumice			
WSWPST-2F	74.8	Pumice			
WSWPST-2G	74.4	Pumice			
WSWPST-4B	69.1	Pumice (Mod. Welding)	11S 0740173 3864203	Warm Springs Wilderness Area, west (AZ)	
WSWPST-4D	71.9	Pumice (Mod. Welding)			
GJPST-1A	72.0	Pumice	11S 0739361 3902329	Grasshopper Junction; top of prominent knob (AZ)	
GJPST-1C	73.1	Pumice			
PT-1B-4	75.2	Pumice	11S 0670678 3848191	Piute Mountains; low wash (CA)	Distal Outflow
KPST01A	75.3	Pumice	11S 0769890 3897793	Kingman; outcrop of tuff overtopping cinder cone (AZ)	
KPST01B	75.1	Pumice			
KPST01C	75.4	Pumice			
KPST01D	75.5	Pumice			
KPST01E	75.1	Pumice			

[32] This coordinate is located at a lower elevation from the actual sampling site. The sample was taken from the top-most unit of the section, in a non-welded zone

PST textures and mineral assemblages

Thin sections were examined using a petrographic microscope to characterize mineral assemblages and to observe textural features. The Hitachi S-4200 scanning electron microscope (SEM) in the Vanderbilt University Electron Optics Laboratory was used to examine and image mineral assemblages and textures in epoxy-mounted samples using secondary electron (SE) and backscattered electron (BSE) detectors. Glass compositions were determined using a Cameca SX-50 electron microprobe (EMP) at the University of Tennessee-Knoxville EMP Laboratory. Special attention was given to CRWPST and KPST01D, compositional end members in this study (excluding mafic enclave WSWPST-1).

Whole rock geochemistry

We treated uncrushed samples of pumice and fiamme in successive acid baths (0.1M oxalic acid and 2% H_2O_2 then 0.1 M HCl, 2% H_2O_2) to reduce effects of weathering and surface alteration. Samples were sent to Activation Laboratories (Actlabs, Ancaster, Ontario Canada) for whole-rock geochemical analysis. Actlabs used a combination of inductively coupled plasma optical emission spectroscopy (ICP), instrumental neuron activation analysis (INAA), inductively coupled plasma mass spectrometry (ICP-MS) and x-ray fluorescence spectrometry (XRF) to measure major and trace element compositions (Table 2).

MELTS modeling

We used a modified version of MELTS (Ghiorso and Sack, 1995; Ghiorso, 2010, pers. comm.) to model changing conditions in the pre-eruptive Peach Spring Tuff magmatic system. The version of MELTS that we used is calibrated for use with systems with high SiO_2 and adjusted to better compute the quartz-alkali feldspar saturation surface (Gualda and Ghiorso, 2009). This study is among the first to use this updated version of MELTS (see also AGU abstract by Vaum et al., 2009) to model the evolution of silicic systems, so as we attempt to constrain behavior of the PST magmatic system, we simultaneously attempt to assess the limits of this new model and its benefits and limitations for our analytical purposes.

We conducted our modeling using the two compositional end-members from our whole-rock geochemistry dataset. The high-silica end member is KPST01D, a pumice clast from the

distal outflow sheet. The low-silica end member is CRWPST, a fiamma from the welded intracaldera tuff.

In our modeling efforts we explore the effects of pressure, water content, and crystallization mode (equilibrium versus fractional crystallization) on the chemical evolution and physical response of the magmatic system (modeled each time with a mass of 100 g). We use KPST01D and equilibrium crystallization to examine the response of the system to variable pressure (150MPa to 350 MPa in 50 MPa increments) and variable water contents (2, 3, 5, 7 wt. %), which can be conveniently displayed as a matrix (Appendix C). We charted the evolving composition of the melt, the relative timing of new phases entering the system, the mass, volume and density of the total system and of each phase present, temperature range over which changes took place, and variable liquidus and cotectic (minimum) conditions. After exploring the parameter space using KPST01D and equilibrium crystallization, we used a pressure of 250 MPa with fractional crystallization to see how this change impacted the behavior of the system. Simulations run with 5 wt. % water using both equilibrium and fractional crystallization yielded unrealistic results (due to convergence problems for these conditions) and have been excluded from this study, but plotted results are still available in Appendix D.

The final modeling step was to run melting experiments using the CRWPST composition, 250 MPa and a range of water contents (0.25, 0.5, 1, 2 wt. % water). The purpose of these simulations was to examine the evolution of melt percentage with temperature, with particular attention to the effect of variable water content on the temperature and energy necessary for melting.

CHAPTER IV

RESULTS

Whole Rock Geochemistry

Whole-rock geochemistry analytical results are available in Table 2. Selected major-element data are presented as plots of total alkalis against silica (wt. %) in Figure 3, and in Harker-type diagrams in Figure 4. Whole-rock and glass compositions are also projected onto the Qz-Ab-Or ternary in Figure 5 using the projection scheme of Blundy & Cashman (2001); experimentally-determined quartz-alkali feldspar cotectic curves for various pressures are indicated, also following Blundy & Cashman (2001). Our analyses reveal that the Peach Spring Tuff is characterized by high to very high K_2O (5.8-7.3 wt. %) but in other respects samples range widely in composition. This compositional variability, previously unrecognized in the tuff, appears to correlate with proximity to the eruptive source. Whole-rock compositions reveal that fiamme in the intracaldera fill are trachyte (66-69 wt. % SiO_2); pumice and fiamme in proximal outflow are trachyte to rhyolite (68-76 wt. % SiO_2), and distal outflow pumice is rhyolite with somewhat higher silica contents (~75 wt. % SiO_2). Sparse magmatic enclaves (57 wt. % SiO_2 [a single analysis]) indicate that mafic to intermediate magma was present in the chamber during eruption. The correlation between major-element whole-rock compositions and proximity to caldera is shown particularly well in the Harker diagrams (Figure 4**)**. Most elemental concentrations vary regularly against SiO_2, with Al_2O_3, CaO, TiO_2, Fe_2O_3, MgO and P_2O_5 decreasing monotonically as SiO_2 rises. There is a general decrease in Na_2O with rising SiO_2, and outliers can reasonably be explained by modifications during alteration. K_2O remains relatively constant at all SiO_2 concentrations.

Table 2

Whole-Rock Geochemistry of Peach Spring Tuff Samples

	Intracaldera				Proximal Outflow							
	CRW PST	CRW 2A	PSTG 1C	28571 PST-BF	28556 PST-P1	WSW PST 2A	WSW PST 2B	WSW PST 2D	WSW PST 2F	WSW PST 2G	WSW PST 4B	WSW PST 4D
SiO_2	66.1	68.7	68.2	62.9	69.3	75.1	71.0	76.1	74.8	74.4	69.1	71.9
Al_2O_3	17.0	16.30	15.99	14.87	15.39	12.84	14.70	12.69	13.35	13.57	16.18	14.80
$Fe_2O_{3(T)}$	3.26	3.33	2.74	8.35	2.65	1.40	1.96	1.09	1.27	1.32	1.98	1.69
MnO	0.06	0.05	0.08	0.15	0.08	0.08	0.08	0.05	0.04	0.05	0.05	0.05
MgO	0.81	0.66	0.46	1.50	1.11	0.20	0.23	0.09	0.13	0.12	0.60	0.35
CaO	1.21	0.74	1.26	3.89	1.65	0.61	0.85	0.51	0.60	0.65	1.19	0.92
Na_2O	3.49	5.82	3.91	3.82	2.69	3.63	4.04	3.29	3.45	3.56	3.75	3.86
K_2O	7.33	3.80	6.64	2.73	6.56	5.86	6.77	5.99	6.17	6.06	6.67	6.03
TiO_2	0.57	0.49	0.57	1.22	0.46	0.23	0.35	0.19	0.21	0.22	0.39	0.34
P_2O_5	0.20	0.13	0.10	0.51	0.13	0.02	0.02	0.02	0.02	0.02	0.04	0.03
LOI	1.05	1.3	0.74	2.06	5.56	0.68	0.61	0.45	0.56	0.43	2.07	1.46
Rb	149	81	125	80	141	195	178	196	213	211	157	162
Sr	437	256	177	360	185	18	23	21	26	19	67	27
Ba	2850	1565	934	907	802	40	75	70	60	65	222	59
Cs	1.8	0.8	1.2	1.3	1.5	1.5	1.4	1.4	1.4	1.7	1.9	2.1
Pb	28	16	30	14	15	24	25	20	16	18	25	25
Nb	18.5	23.7	32	28.2	31.4	34.3	31	30.9	34	33.9	24.1	30.8
Ta	1.18	0.95	2.52	1.17	1.38	2.43	2.18	2.23	2.33	2.53	1.61	2.29
Co	3.3	2.9	2.4	7.5	2.3	1.8	1.5	1.2	1.9	1.6	2.3	2
Cr	52.2	6.4	3.9	25.8	1.8	29.8	8	39.6	5.4	29.6	4.6	39.7
Ni	6	5	2	17	2	4	3	6	3	4	2	3
V	32	21	23	92	18	< 5	8	6	< 5	< 5	12	9
Zr	759	615	679	510	608	257	513	249	252	238	500	475
Hf	14.9	13.5	14.5	12.4	14.4	8.1	12.2	7.6	7.5	7.6	11	11.8
Th	16.7	16.5	21.1	6.09	22	24.5	20	27.6	28.4	29	19	20.8
U	2.39	2.03	3.27	1.71	2.8	4.1	2.77	4.89	4.07	4.62	2.53	2.91
Sc	1.4	6.84	0.6	14.9	6.8	1	0.6	0.9	1.1	1.5	9.3	6.2
Y	30	27	38	51	34	33	57	33	32	33	30	61
La	34.2	154	39.2	59.7	147	15.6	30	14.4	13.2	15.1	31	24.7
Ce	113	295	129	136	298	48.2	107	43.9	41.8	45.1	108	96.3
Pr	16	32.8	19.4	17	32.3	8.5	22.3	8.01	7.35	8.01	16.5	20.8
Nd	3.8	114.0	3.1	66.3	112.0	0.6	1.6	0.6	0.6	0.6	2.5	1.5
Sm	12	15.9	14.5	13	16.8	6.48	15.9	6.08	5.45	6.53	10.3	15.7
Eu	1.29	3.46	1.67	2.6	2.66	1.03	2.63	0.99	0.91	1.01	1.39	2.5
Gd	6.13	9.93	8.12	11.2	11.4	5.85	14	5.66	5.21	5.62	6.8	13.2
Tb	1.1	1.21	1.49	1.68	1.52	1.19	2.49	1.12	1.08	1.15	1.26	2.45
Dy	3.08	5.85	4.04	9.67	7.58	3.47	6.32	3.18	3.14	3.37	3.43	6.16
Ho	0.45	1.07	0.24	1.87	1.38	0.2	0.14	0.33	0.38	0.41	0.12	0.24
Er	0.42	2.89	0.58	5.33	3.81	0.55	0.88	0.54	0.52	0.55	0.50	0.85
Tl	2.72	0.37	3.53	0.26	4.14	3.46	4.86	3.17	3.31	3.47	3.02	4.79
Tm	0.40	0.41	0.50	0.77	0.54	0.47	0.62	0.44	0.46	0.48	0.45	0.60

Table 2 (Continued)

Whole-Rock Geochemistry of Peach Spring Tuff Samples

	Proximal Outflow			Distal Outflow					
	WSW PST 1	GJPST 1A	GJPST 1C	PT-1B-4	KPST01A	KPST01B	KPST01C	KPST01D	KPST01E
SiO_2	57.6	72.0	73.1	75.2	75.3	75.1	75.4	75.4	75.2
Al_2O_3	16.96	14.74	14.08	12.76	12.74	12.80	12.24	13.14	12.90
$Fe_2O_{3(T)}$	7.48	1.83	1.80	1.19	1.19	1.17	1.09	1.06	1.18
MnO	0.07	0.04	0.08	0.06	0.08	0.07	0.07	0.07	0.07
MgO	2.50	0.17	0.19	0.43	0.17	0.26	0.35	0.20	0.24
CaO	5.41	0.55	0.61	1.05	1.13	0.61	1.15	0.75	1.02
Na_2O	3.50	3.89	3.74	2.12	2.23	2.63	2.61	2.72	2.29
K_2O	4.59	6.32	5.96	6.93	6.92	7.15	6.82	6.39	6.91
TiO_2	1.32	0.36	0.33	0.21	0.23	0.21	0.19	0.20	0.22
P_2O_5	0.55	0.06	0.06	0.02	0.02	0.02	0.03	0.03	0.02
LOI	1.82	0.89	1.22	4.01	3.5	3.2	3.5	3.2	4.0
Rb	96	142	138	242	201.0	217.0	221.0	198.0	194.0
Sr	1514	22	37	26	17.0	14.0	17.0	17.0	18.0
Ba	1943	87	209	193	32.0	51.0	34.0	40.0	48.0
Cs	6.3	0.9	1	3.5	3.5	3.8	3.9	3.3	3.3
Pb	46	25	20	26	30.0	34.0	23.0	24.0	26.0
Nb	21.5	28.3	31.8	49.3	37.8	44.5	43.4	39.4	38.4
Ta	1.27	2.22	2.48	2.55	2.5	2.8	2.8	2.5	2.5
Co	14.4	2.5	2.2	1.4	1.8	1.6	2.2	1.7	2.7
Cr	123	48.1	2.8	6.6	< 0.5	2.1	< 0.5	< 0.5	< 0.5
Ni	51	4	2	2	< 1	< 1	< 1	< 1	< 1
V	109	19	12	7	6.0	6.0	7.0	< 5	9.0
Zr	400	478	445	250	221.0	239.0	223.0	221.0	200.0
Hf	9	11.4	11	9.2	8.6	9.1	8.7	8.8	7.9
Th	20.3	22.2	20.6	37.1	32.2	34.4	35.3	32.9	30.2
U	4.15	2.82	2.5	6.99	6.1	6.3	6.7	6.2	5.7
Sc	83.6	0.6	0.6	3.32	3.6	3.4	3.4	3.5	3.6
Y	31	47	38	31	38.0	36.0	33.0	33.0	38.0
La	30.8	26.7	24.6	58.9	70.1	72.1	68.8	69.7	69.0
Ce	104	98.6	90.4	118	127.0	131.0	124.0	124.0	121.0
Pr	15.8	20.3	18	11.9	14.7	15.2	13.9	13.9	14.5
Nd	3.4	1.5	1.4	36.5	42.2	43.4	38.6	38.7	41.7
Sm	11	14.1	12.6	6.68	7.8	7.9	6.8	6.7	7.5
Eu	1.2	2.18	1.84	0.418	0.6	0.6	0.5	0.6	0.6
Gd	5.64	11.1	9.09	5.33	6.5	6.6	5.7	5.5	6.5
Tb	1.01	1.96	1.62	0.87	1.1	1.1	0.9	0.9	1.0
Dy	2.74	4.88	4.06	5.26	6.1	6.2	5.4	5.2	5.7
Ho	0.54	0.32	0.33	1.06	1.2	1.2	1.1	1.0	1.1
Er	0.37	0.73	0.58	3.24	3.4	3.5	3.3	3.2	3.4
Tl	2.35	3.83	3.42	0.9	1.4	1.3	1.4	1.1	2.3
Tm	0.33	0.51	0.45	0.54	0.5	0.6	0.5	0.5	0.5

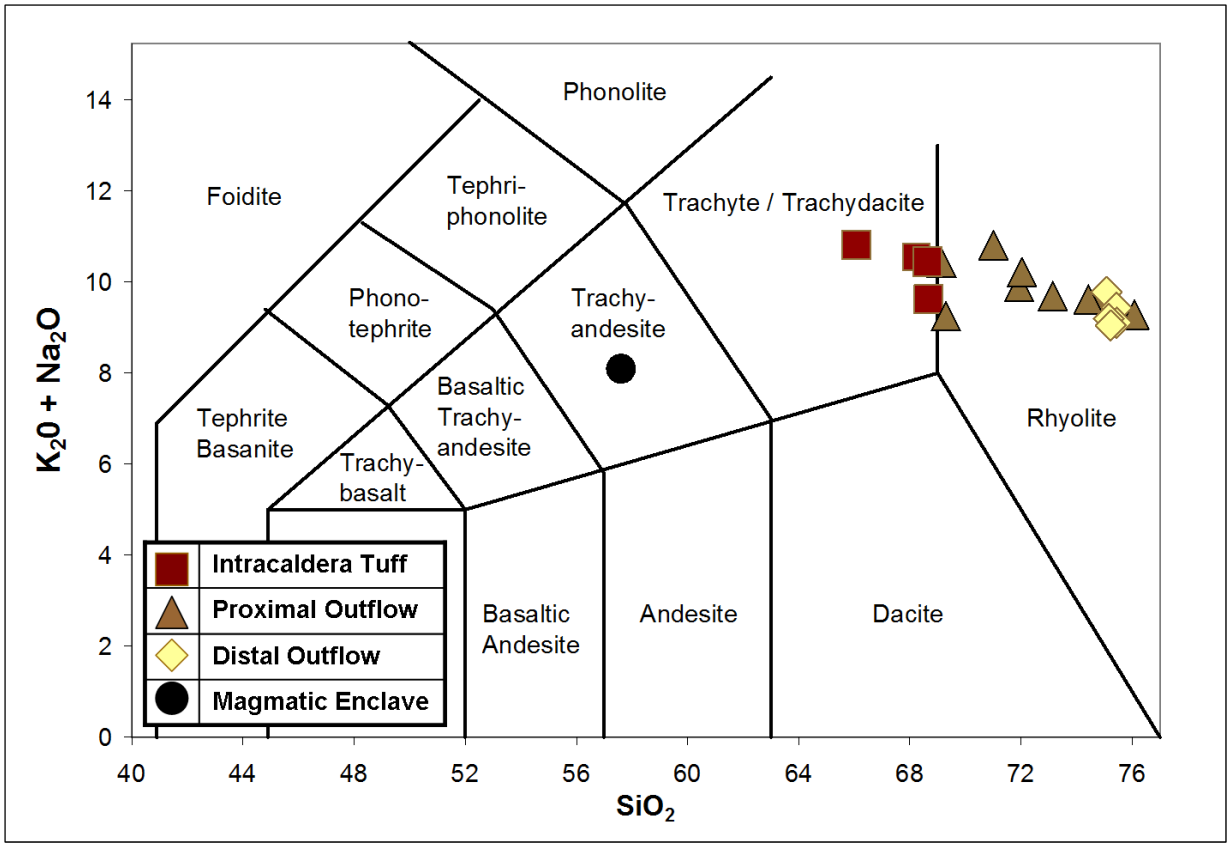

Figure 3

IUGS (Le Bas, 1986) volcanic rock classification using total alkalis vs silica (wt. %). Fiamme and pumice compositions are correlated with proximity to caldera, with the lowest silica and highest total alkalis in the caldera fill and the highest silica and lowest total alkalis farthest from the caldera. The composition of the magmatic enclave (from PST at Warm Springs Wilderness Area) is included to illustrate the range of compositions associated with this magmatic system, though we do not think it has direct bearing on the geochemical evolution of the PST.

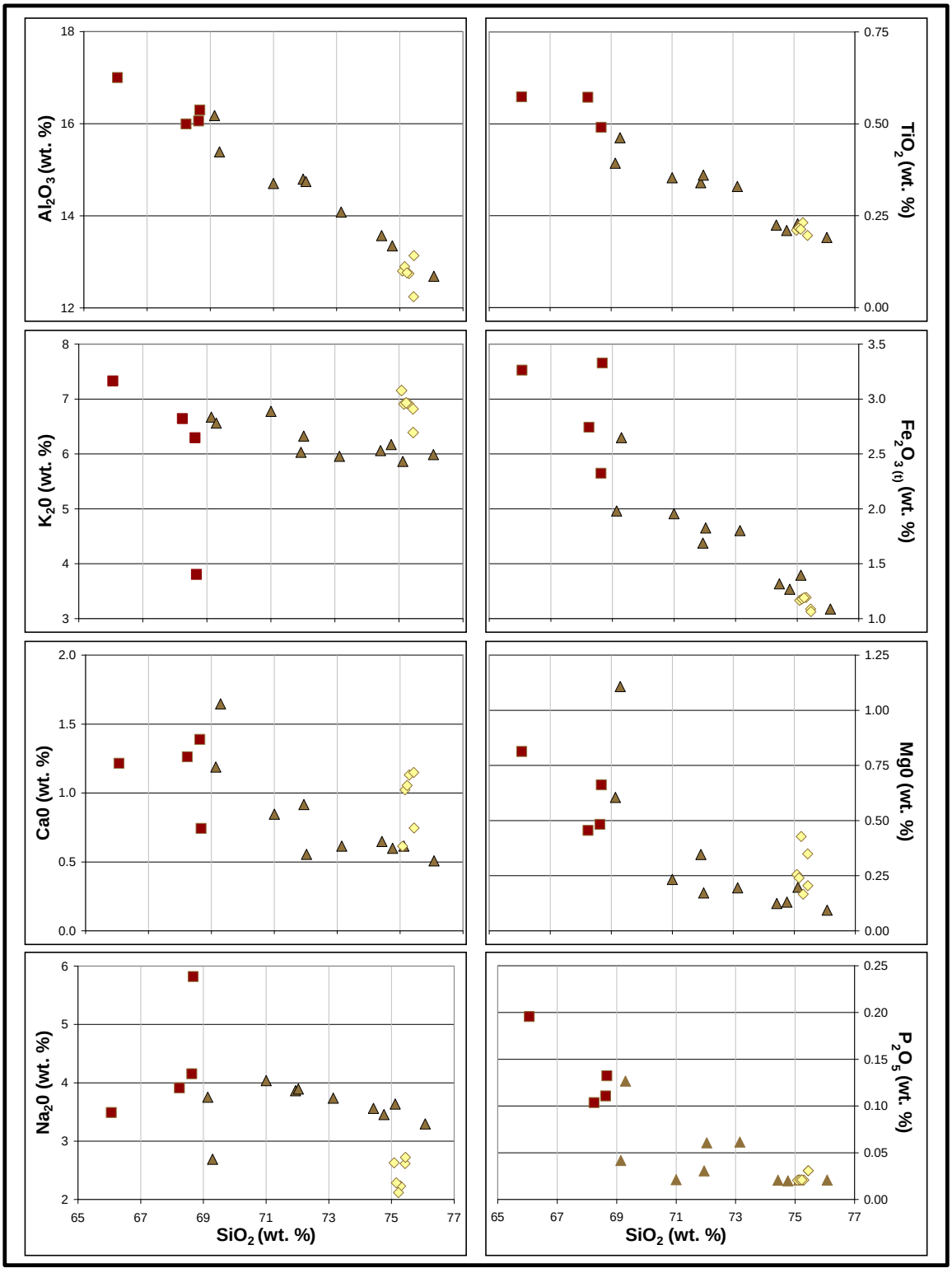

Figure 4

Whole rock geochemistry Harker diagrams for major elements. Symbols as in Figure 3. The correlation between chemistry and proximity to caldera is shown particularly well in these plots.

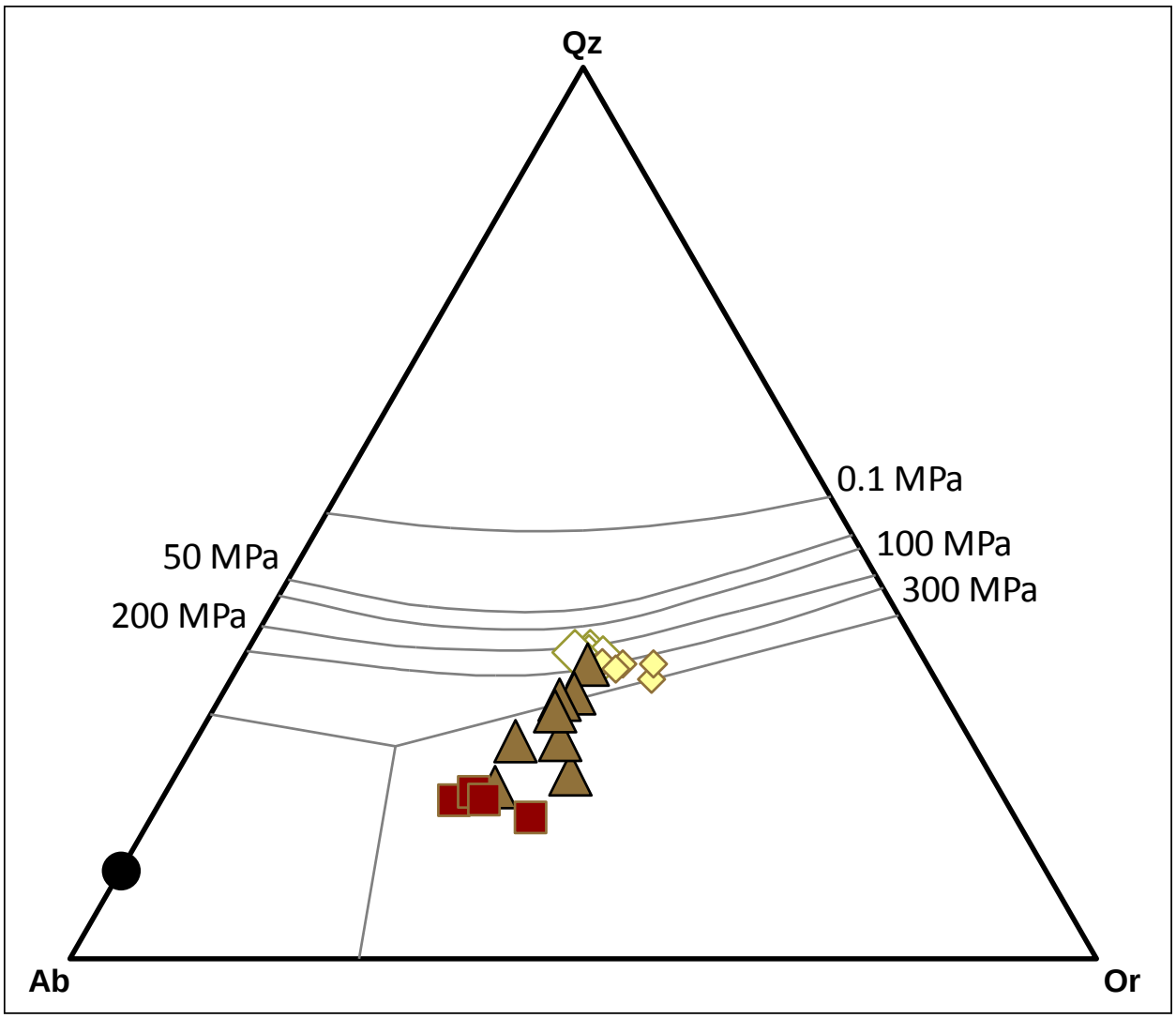

Figure 5

Whole-rock and glass compositions projected onto the Qz-Ab-Or ternary, following the projection scheme of Blundy & Cashman (2001); experimentally-determined quartz-alkali feldspar cotectic curves for various pressures are shown for reference, also from Blundy & Cashman (2001). Symbols as in Figure 3, with the exception that filled symbols represent whole-rock compositions while open symbols represent glass compositions.

Modeling Outputs

A total of 28 simulations (24 crystallization, 4 melting) were completed. For our crystallization simulations, our focus is on the chemical evolution and physical response of the Peach Spring system under a variety of conditions. We paid particular attention to variation in mass of individual phases, volume and density of the total system and of each phase present, the sequence of saturation and saturation temperature for each phase entering the system, the temperature range over which changes took place, and liquidus and pseudo-invariant temperatures. For our melting simulations, our primary interest lay in examining the total volume of the system that is accounted for by melt as temperature (and enthalpy input) rises, and to see how water content influences the behavior of the system. A compilation of plotted results for each simulation is available in Appendix D.

Example of a Simulation

The outputs of the crystallization simulation using equilibrium crystallization, 200 MPa and 3 wt. % water are shown in Figure 6. We show the variations in mass (of individual phases), volume and density as a function of temperature, and a projection of melt compositions on a Qz-Ab-Or ternary diagram, to illustrate the type of data considered in this study.

Graphs depicting variation in mass (e.g., Figure 6.A) and volume (e.g., Figure 6.B**)** of individual phases versus temperature reveal liquidus temperature, saturation temperature for the various phases, relative abundance of each phase, and changing proportions of solids (crystals), liquid (melt) and fluid (water). In this particular simulation, we see that sanidine is the liquidus phase, saturating at ~830 °C with quartz appearing after approximately 30 °C of cooling. In each simulation, there is a point at which the total volume and density of the system, the masses of individual phases, and the composition of the melt change dramatically, causing a sharp kink in plotted curves. This abrupt change corresponds with the system reaching a pseudo-invariant (very few degrees of freedom in the context of the Gibbs phase rule) where the melt is multiply-saturated in quartz, plagioclase, sanidine, and fluid (water). In this particular simulation, we see that this pseudo-invariant is reached at approximately 750 °C when plagioclase and water enter the phase assemblage. We are particularly interested in the changes in total volume and density as the system nears, and reaches this pseudo-invariant. In this particular simulation (Figure 6.C), we see that the total density of the system gradually increases until the pseudo-invariant is

reached, at which point there is a sudden 15% decrease in density over ~10 °C interval, a consequence of extensive fluid exsolution.

In the Qz-Ab-Or ternary (Figure 6.D**)**, we see that the simulated melt evolves from its initial composition away from the Ab-Or join, towards a composition that approximately matches the actual KPST01D glass composition; upon quartz saturation, the melt starts evolving along a path that parallels the experimentally-determined 200 MPa cotectic curve, as expected.

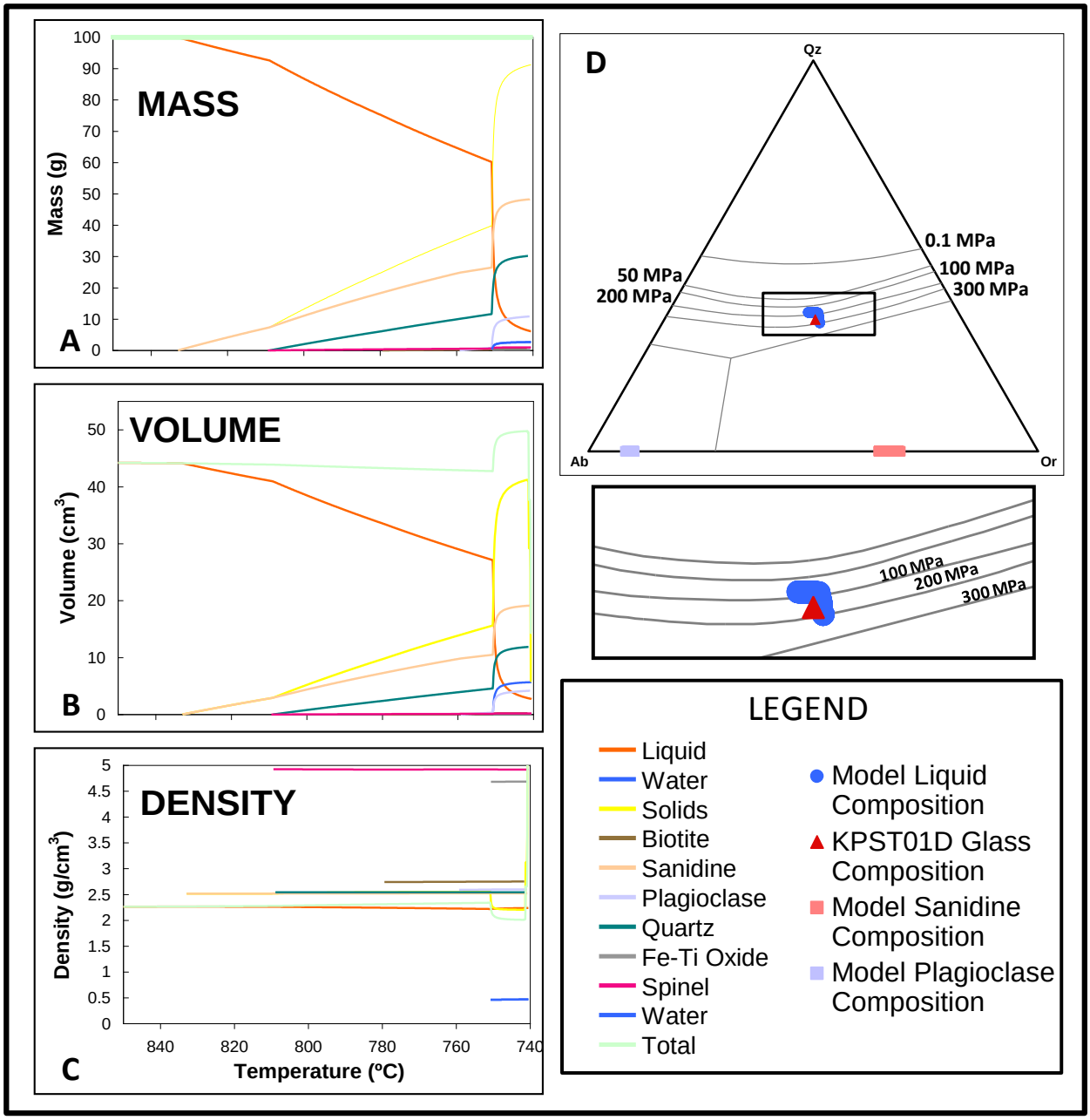

Figure 6

Data from one simulation run with equilibrium crystallization, composition KPST01D, 200 MPa and 3 wt. % water. The dramatic kink that is present in plots of mass (A), volume (B) and density (C) at approximately 750 °C represents the response of the system to reaching a pseudo-invariant where the melt is saturated in quartz, two feldspars and water. (D) Evolution of melt compositions on the Qz-Ab-Or ternary (using the Blundy and Cashman, 2001 projection scheme) is also shown, with the evolving melt composition plotting along the 200 MPa quartz-alkali feldspar cotectic, shown in detail in zoomed-on box. Cotectic pressures in the labeled box are placed below the cotectic curve to which they correspond.

Crystallization Results

We compiled results from crystallization simulations and created a number of simple summary plots to study the variable response of the system to variations in pressure, water contents, and crystallization conditions.

Crystallization Intervals

For simulations run with equilibrium and fractional crystallization at a fixed pressure of 250 MPa and variable water contents (Figure 7 and 8, A and B), we see that the temperature range over which crystallization takes place is dependent upon the water content of the system. Systems with lower water contents achieve the liquidus condition at higher temperatures, but the temperature of the pseudo-invariant remains the same for each simulation. Liquidus temperatures for simulations run with 2, 3 and 7 wt. % water were 890 ºC, 840 ºC and 762 ºC, respectively, and the pseudo-invariant temperature for each of these runs was 743 ºC.

For simulations run with equilibrium and fractional crystallization at a fixed water content of 3 wt. % and variable pressure (Figure 7 and 8, C) we see that the liquidus temperatures for each simulation, while not exactly the same, are quite similar (850 ºC to 825 ºC) and do not appear to vary systematically. The temperature of the pseudo-invariant is, however, inversely correlated with pressure.

Total Volume Evolution

Water content has a strong effect on the range of total volume achieved by the evolving system. In the case of simulations run with equilibrium crystallization at a constant pressure of 250 MPa, 2 and 3 wt. % water, total volume decreases with decreasing temperature, while the opposite is observed for the simulation with 7 wt. % water (Figure 7, A). The key difference is that simulations with 2 and 3 wt. % water were water-undersaturated during this stage, while the 7 wt. % water simulation was water-saturated from the beginning. Once the pseudo-invariant is achieved, the total volume for each simulation increases dramatically. The magnitude of this volume-increase is different for each system, dependent upon water content and timing of water saturation (volume change in 7 wt. % < 2 wt. % < 3 wt. %). One of the most noteworthy observations from our simulations is that volume increases dramatically over a very narrow range of temperatures once systems reach the pseudo-invariant (e.g., 14% in 13 ºC for the run

with 3 wt. % water). Systems with high initial water, which are saturated in water before reaching the pseudo-invariant, experience a smaller increase in volume compared to systems that have less initial water and remain undersaturated until the invariant (e.g., 2% increase with 7 wt. % water vs. 14% increase for system with 3 wt. % water).

With all other conditions held constant, we see that fractional crystallization leads to volume changes very similar to those achieved with equilibrium crystallization (Figure 7, B). For 3 and 7 wt. % water, equilibrium and fractional crystallization gave nearly identical results. The simulation with 2 wt. % water was very similar, but the magnitude of volume change upon reaching the pseudo-invariant was much lower with fractional crystallization.

We see that pressure has a moderate control on the range of volumes achieved by the evolving system. Using simulations run with equilibrium crystallization and a fixed water content of 3 wt. % as a guide (Figure 7, C), we notice a gradual decrease in volume as crystallization progresses from the liquidus to the pseudo-invariant. During this stage of crystallization, the systems simulated at the lowest pressures had the largest volumes, while the systems simulated at the highest pressures had the smallest volumes, a consequence of the increase in melt density with pressure. The general trend is that volume dramatically increases upon reaching the pseudo-invariant (see above), with a few notable exceptions. The simulation run at 150 MPa had an abrupt drop in volume upon reaching conditions where quartz and 2 feldspar were both saturated, but after 1 ºC water also saturated, and the system responded with a great increase in volume. The simulation run at 350 MPa is different from all others we considered: when the system reaches the pseudo-invariant, we see a dramatic drop in volume, rather than a dramatic increase. This high-pressure simulation is the only one in which water does not saturate during the modeled course of crystallization (presumably saturation would have been achieved before the solidus was reached, but the model was terminated before that point).

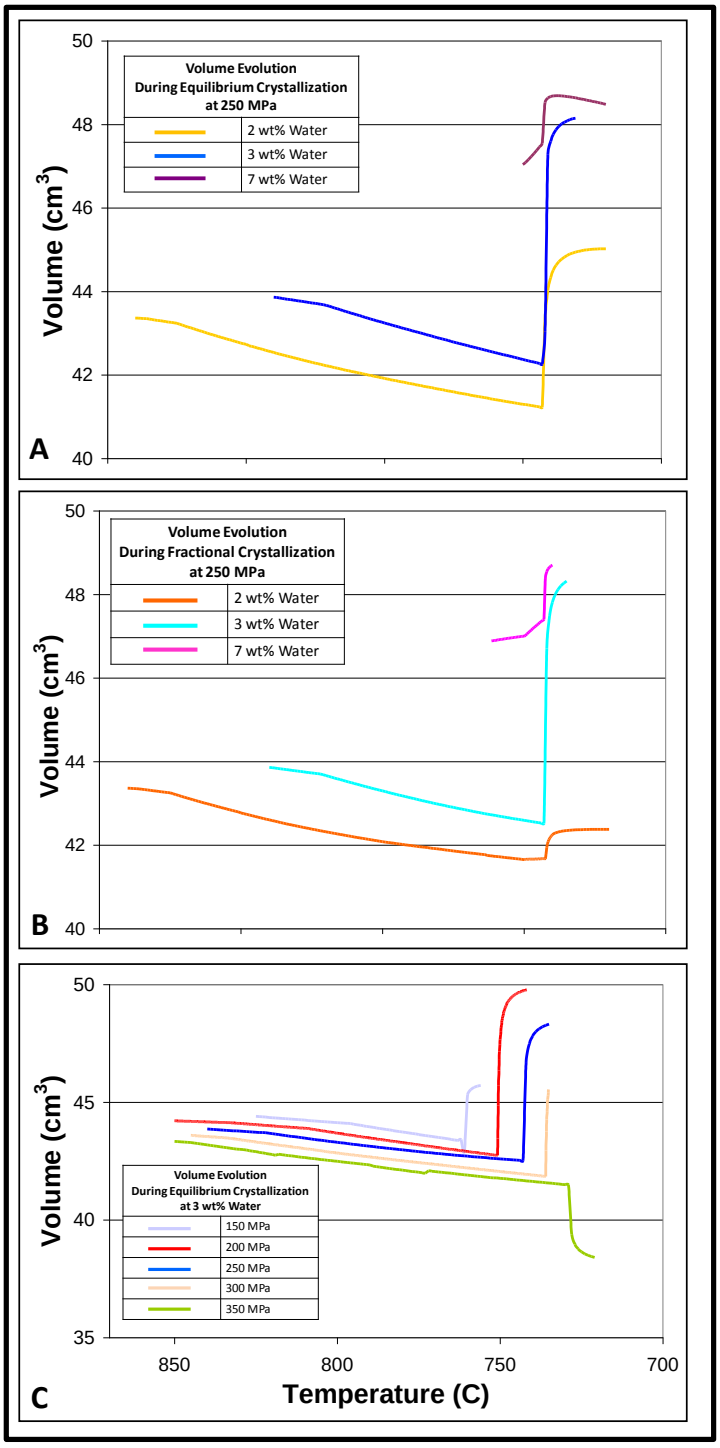

Figure 7

Compilation plots for volume evolution throughout the course of crystallization. All simulations were run with an initial mass of 100 g. A: Volume evolution during fractional crystallization with constant pressure (250 MPa) and variable water contents (2, 3, 7 wt. %); B: Volume evolution during equilibrium crystallization with constant pressure and variable water contents; C: Volume evolution during equilibrium crystallization with fixed water (3 wt. %) and variable pressure (150, 200, 250, 300, 350 MPa). Each line represents a single simulation conducted using the whole-rock composition of KPST01D.

Total Density Evolution

The evolution of density in our simulations parallels the volume evolution described above. Water content has a strong control, and pressure a moderate effect, on the range of density that will be achieved by the evolving system. With one exception, the density for each simulation decreases dramatically when the pseudo-invariant is reached. The only exception is the simulation with 3 wt% water and 350 MPa (equilibrium crystallization), in which water-saturation was never reached. In this case, density dramatically increased at the pseudo-invariant as a result of increased crystallization in the absence of water. In cases where density decreased, the magnitude of the decrease is largely dependent upon water content (though similar results are seen when pressure is altered and water is held constant). The greatest density decreases are for systems in which water saturation takes place close to or at the pseudo-invariant (e.g., 2 and 3 wt. % water), while systems that are saturated in water throughout the course of crystallization experience a more subtle decrease in density (e.g., 7 wt. % water). What is striking about our results is that they show that density can drop by as much as 10-15% to values as low as 2.05 g/cm^3 in a temperature range as narrow as 1-10 ^{o}C.

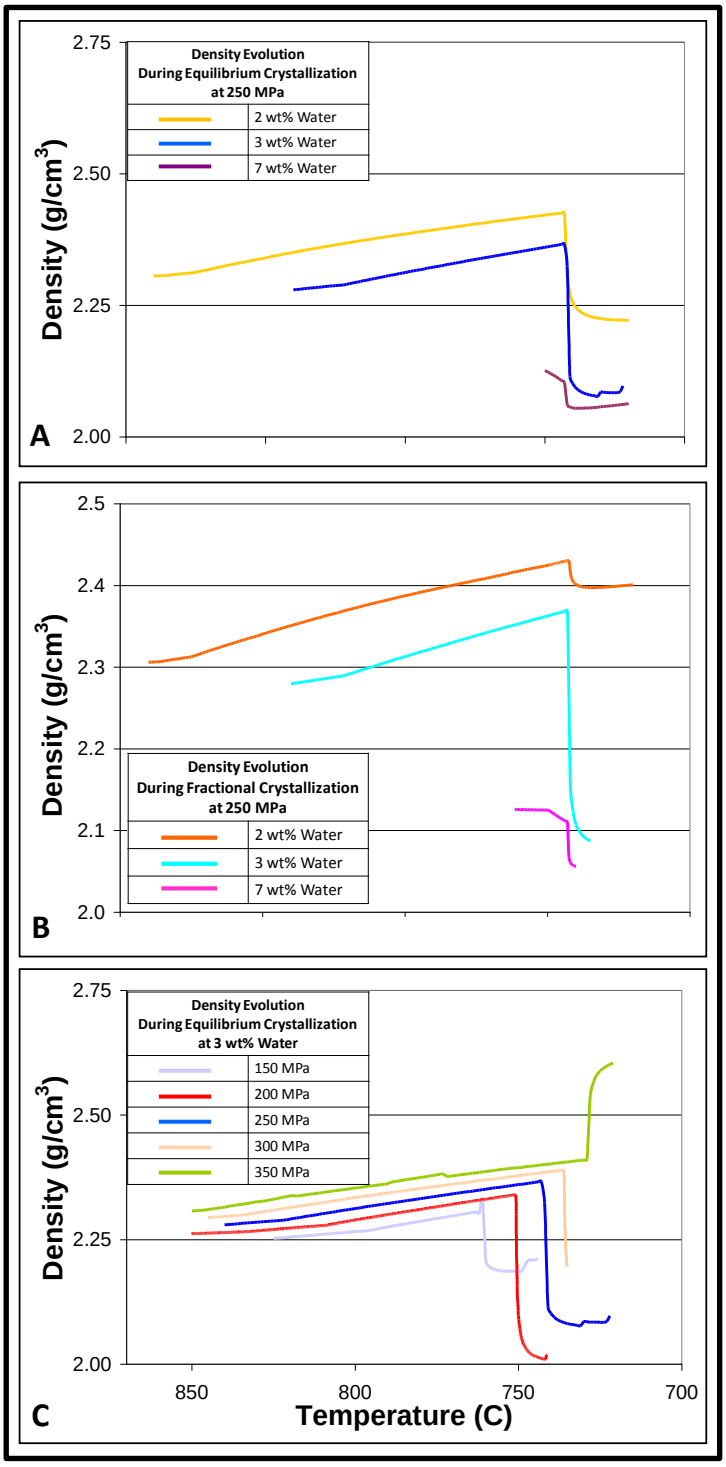

Figure 8

Compilation plots for density evolution throughout the course of crystallization. A: Density evolution during equilibrium crystallization with constant pressure (250 MPa) and variable water contents (2, 3, 7 wt. %); B: Density evolution during fractional crystallization with constant pressure and variable water contents; C: Density evolution during equilibrium crystallization with fixed water (3 wt. %) and variable pressure (150, 200, 250, 300, 350 MPa). Each line represents a single simulation conducted using the whole-rock composition of KPST01D.

Evolution from 0 to 25% wt. % Crystals

We are interested in the behavior of the PST magma from near-liquidus conditions (very crystal poor) to a point of approximately 25 wt. % crystals. Most PST pumice and fiamme show between 4 and 25 modal % crystals, so by examining conditions from ~0 to ~25 wt. % crystals we are attempting to study conditions from the inception of crystallization to the time of eruption (with the assumption that modal % and wt. % are approximately equal). With this objective in mind, we plotted the % change in total volume and density vs. change in temperature from liquidus conditions to the point of 25% crystallization for each simulation (all pressures, water contents, and crystallization modes; Figure 9).

Fractional crystallization and equilibrium crystallization yield the same changes when simulations are run at the same pressure and water content. Water content appears to have the greatest control on the behavior of the system as it transitions from liquidus conditions to a point of 25% crystallization. Simulations conducted at low water contents (2, 3 wt. %) experienced a 1-2% increase in volume and a 1-2% decrease in density. It took between 40 and 55 °C of cooling from the liquidus to achieve 25% crystallization for these simulations with lower water contents. Simulations conducted at high water contents (7 wt. %) experienced a 1-2% decrease in volume and 1-2% increase in density (exceptions: greater change for equilibrium crystallization, 350 MPa 7 wt. % water). Simulations for these higher water contents achieved 25% crystallization after 15 to 30 °C of cooling from the liquidus.

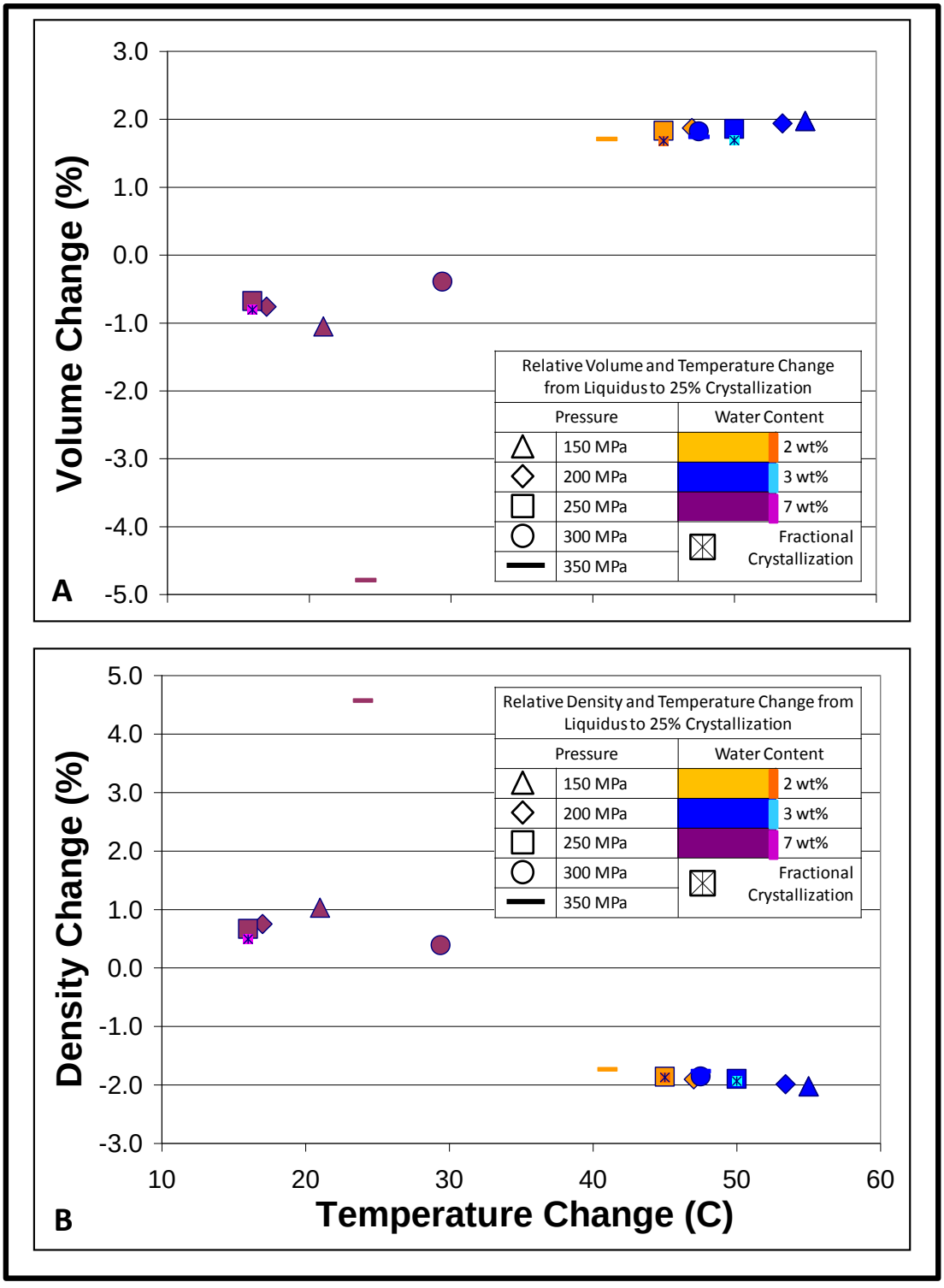

Figure 9

Change in Temperature, Volume and Density from Liquidus to 25% Crystallization. For ease of comparison between simulations, temperature change is given in degrees while change in density is given as a percentage. Each plotted point on the graphs represents data from a single simulation (equilibrium crystallization unless otherwise indicated).

Tracking the Pseudo-invariant with Qz-Ab-Or Ternary

We evaluated the consistency with which our simulations (with variable crystallization mode, pressure and water content) achieved the pseudo-invariant, in an attempt to understand both the reproducibility of the model and also the ability of our simulations to identify the pressures experienced by the Peach Spring Tuff magma. In the Qz-Ab-Or ternary diagram (Figure 10.A), we see that the melt compositions in which quartz and alkali feldspar saturation is reached in each simulation cluster tightly together, approximately following the experimentally-derived cotectic curve for the appropriate pressure. The compositions at which each simulation became saturated in quartz and 2 feldspars are similarly clustered (Figure 10.B), with somewhat of a larger horizontal spread. Figure 10 shows that quartz saturates before the plagioclase, and the melt compositions follow paths from quartz saturation to plagioclase saturation (toward the ternary minimum) that parallel the experimentally-derived cotectic curves.

Some of the results from our simulations are in disagreement with characteristics of the PST. In particular, the model consistently predicts quartz saturation prior to plagioclase saturation, while PST rocks invariably have plagioclase while quartz is rare or absent. Despite this limitation, the general physical changes (density, volume) and their relative magnitudes calculated by MELTS should be robust as systems approach and achieves the pseudo-invariant, and these are the focus of the present study.

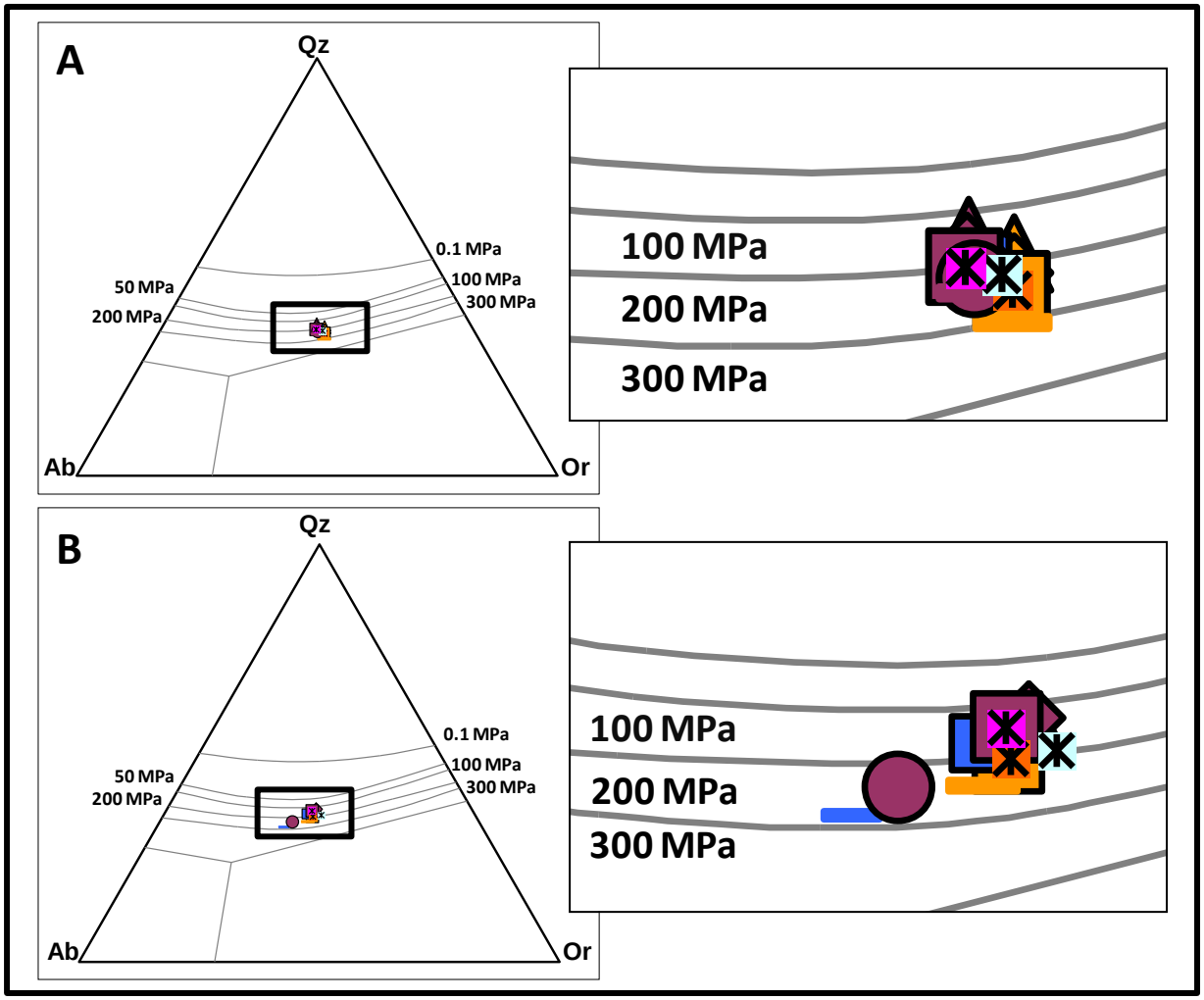

Figure 10

Tracking the pseudo-invariant with Qz-Ab-Or projections. Symbols as in Figure 9. Each plotted point represents the composition of melt (for a single simulation) at the temperature at which (A) quartz and one feldspar are present together in the melt for the first time, and (B) quartz and two feldspars are present together for the first time. Experimental cotectics (Blundy and Cashman, 2001) are drawn in for reference, with labels falling below the corresponding cotectic in the zoomed-in box. Notice how each simulation plots close to the cotectic for the corresponding pressure.

Melting Results

We ran melting simulations using the composition of CRWPST, our most-mafic fiamme from the intracaldera tuff. Simulations were run at a constant pressure of 250 MPa and variable water contents (0.25, 0.5, 1, and 2 wt. %). Our primary interest in these simulations is to examine the evolution of melt abundance with temperature (particularly ≥50% melt, see discussion) and to see how variable water content influences the energy (enthalpy) input and temperature range necessary to increase the total amount of melt in the system from near-zero to ~50% by volume. Results can be seen in Figure 11.

Water is positively correlated with the volume of melt in a magmatic system that is being subjected to heating. We see that for a given temperature, melts with the highest water content have the highest melt fractions and lowest input of enthalpy. Similarly, magmas with more water will have a higher melt fraction at a lower temperature than magmas with less water. For instance, consider the temperature necessary for each system to reach a point where melt accounts for 50% of the total volume of the system. This condition is reached at 948 °C (and enthalpy input of 42.5 J/g) for the system with only 0.25 wt. % water, but at only 747 °C (and enthalpy input of 17.5 J/g) for the system with 2 wt. % water.

The correlation between water-content and variable-volume ceases to apply when the systems being compared are both water-saturated. For example, our simulations with 1 and 2 wt. % water are both water-saturated at temperatures of ≤ 700 °C to 732 °C. In this temperature range, under conditions of saturation, these two simulations behave identically. It is only after temperatures exceed 732°C and the simulation with 1 wt. % water becomes undersaturated in water that the two systems can be distinguished on the basis of water content and relative volume of melt.

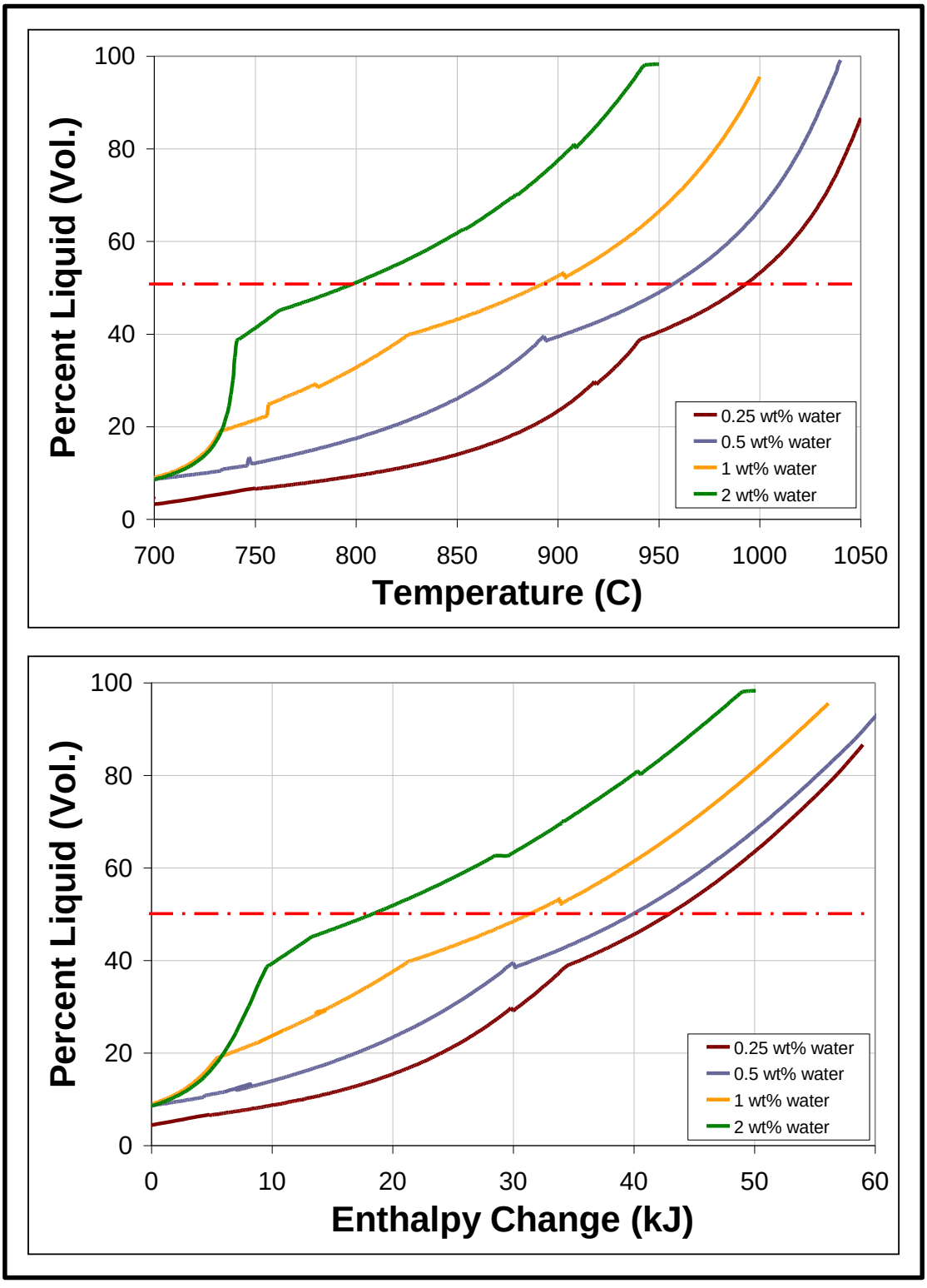

Figure 11

Plots depicting (A) the changing percent liquid (by volume) with rising temperature and (B) the changing percent liquid (by volume) with rising enthalpy. The red dashed line on each plot is located at 50% liquid (by volume), a threshold that we consider necessary to overcome for the intracaldera PST magma to have been eruptible.

CHAPTER V

DISCUSSION

Potential for a Zoned Magma Chamber

The systematic compositional heterogeneity that we observe in the Peach Spring Tuff leads us to hypothesize that the PST magma chamber was zoned at the time of eruption. The spatial distribution of our sampled compositions suggests that the most-felsic, lowest-density magma was erupted first from the top of the chamber and created the distal outflow sheet, while the least-felsic, highest density magma was erupted last from the bottom of the chamber, creating the intracaldera fill. This hypothesis is in line with early ideas by Lipman et al. (1966), Smith (1979) and Smith and Bailey (1966) that have guided interpretation of many large silicic deposits (e.g, Hildreth, 1981, 2004; Knesel and Duffield, 2007), though it should be recognized that eruptive mechanisms may also influence compositional distribution in deposits (e.g, Hildreth, 1981).

Various hypotheses can explain how this type of zoned magma chamber came into being. Initial zoning may be explained in some cases by crystallization, mush compaction, and melt expulsion (e.g. Bachmann and Bergantz, 2004, 2008). It has been suggested that basal cumulate – melt-depleted mush – can be mobilized by subsequent heating and erupt in the final stages of large eruptions (Kennedy and Stix, 2007; Bindeman and Valley, 2003; Pamukcu, 2010, this study). We use our modeled results to assess the roles that these processes may have played leading to the Peach Spring supereruption.

Crystallizing the Crystal-Poor Rhyolite Cap

Crystallization in a large-volume, zoned magma chamber likely has important physical consequences that may prime a system for eruption (c.f. Blake, 1984; Tait et al., 1989; Fowler and Spera, 2008). We explore the physical response that a magma with the composition of KPST01D may have undergone while crystallizing (fractional and equilibrium) under a variety of initial water contents and pressure conditions. We use our findings to elucidate internal

conditions that may have led to the destabilization and eruption of the Peach Spring Tuff magmatic system.

The system's response to crystallization at different pressures and initial water contents was consistent and systematic for crystallization from the liquidus to near-pseudo-invariant conditions. Higher water contents (e.g., 7 vs. 2-3 wt. %) led to lower liquidus temperatures, higher total volume, lower total density and a narrower temperature range necessary to achieve 25% crystallization. Higher pressure led to lower total volumes, higher bulk density, suppression of water saturation and delayed achievement of the pseudo-invariant (lower temperatures necessary; systematic changes from 350 MPa to 150 MPa).

The most critical aspect of our simulations is that large changes in bulk properties of the system (e.g., bulk density and volume) are observed upon reaching the pseudo-invariant (Table 3). Due to the crystallization of multiple phases simultaneous with water exsolution, the system is subject to sudden changes in volume and density over a narrow range of temperature (e.g., 10-15% increase in volume in the span of 1-10 °C cooling). These sudden changes have significant physical consequences and indicate that the PST system may have been capable of driving itself to eruption.

It is conceivable that these sudden changes (increases or decreases) in total magma volume and density could exceed the yield-strength of surrounding host-rock, promoting eruption by creating fractures that become pathways for magma to escape the system. As our simulations reveal, crystallization at the pseudoinvariant can lead to exsolution of an abundant water-rich fluid phase, which in turn can lead to a significant increase in volume. This sudden increase in volume (and corresponding decrease in density) might initiate fracturing by "pushing" out against the surrounding rock. Conversely, a sudden decrease in volume (and corresponding increase in density), which happens when the pseudo-invariant is reached without fluid saturation (crystals occupy smaller volumes than the melt from which they grew), may initiate fracturing by contracting and disrupting the support and stability of the overlying rock (Blake, 1984). Even in this latter case, where volume decreases and density increases, the density of the magma is lower than that of the surrounding rock. We infer that the hot, buoyant magma may still escape to the surface via the newly created fracture-system, and that fluid saturation would likely be induced by depressurization (though testing this hypothesis with modeling goes beyond the scope of this study).

We emphasize the magnitude of the change in volume and density and the narrow temperature interval over which these changes occur because we hypothesize that these are crucial factors that correlate with the potential for destabilization of the magmatic system, and the likelihood that the system can drive itself to eruption. The observed volume and density changes are most pronounced in systems with only moderate water (e.g., 3 initial wt. % water) that achieve water saturation at, but not before, the pseudo-invariant (Table 3). This suggests that, while silicic systems may drive themselves to eruption during the course of crystallization (as previously suggested by Blake, 1984 and Fowler and Spera, 2008), some systems are more prone to doing so than others. Magmatic systems with high water contents and low densities may be less likely to be jolted to an eruptive condition via crystallization, as the magnitude of change that they experience is relatively minor compared to that experienced by systems with moderate amounts of water (e.g., 2% increase in volume for a system with 7 wt. % water vs. 14% increase for a system with 3 wt. % water at the same pressure; Table 3).

Table 3

Overview of Physical Changes upon Reaching the Pseudo-Invariant[33]

Pressure (MPa)	Initial Water (wt. %)	Temp. interval (°C)	Bulk Volume Change	Bulk Density Change	% Change[34]	Water Saturation
250	2	3.5	Increase	Decrease	3	At Pseudo-Invariant
250	3	8	Increase	Decrease	14	At Pseudo-Invariant
250	7	3	Increase	Decrease	2	At Liquidus
150	3	5	Increase	Decrease	7	At Pseudo-Invariant
200	3	9	Increase	Decrease	16	At Pseudo-Invariant
300	3	1	Increase	Decrease	9	At Pseudo-Invariant
350	3	8	Decrease	Increase	7	After termination of simulation[35]

[33] This table only includes results for simulations run with equilibrium crystallization. Results for crystallization were so similar that we did not deem it necessary to include them here

[34] This is the absolute value of the approximate percentage change for both volume and density

[35] Water would have saturated eventually but the high pressure prevented water from saturating over the range of crystallization explored in this simulation.

Melting the Crystal-rich Intracaldera Trachyte

A growing body of evidence suggests that the intracaldera tuff may represent a remobilized cumulate with a significant amount of melt generated during some sort of heating event (Pamukcu, 2010). Zircons extracted from intracaldera fiamme have estimated Ti-in-zircon temperatures of >900 °C at the rims (lower Ts in interiors; Pamukcu, 2010). Increasing temperature at the base of the PST magma chamber is also supported by textural evidence, including extensive resorption of feldspar, zircon and sphene. We use our MELTS results to assess the viability of this hypothesis, and to provide physical constraints for the melting process.

The presence of water dramatically facilitates the melting of a cumulate with a composition of CRWPST. When water is dissolved in the melt, the volume % of liquid generated over a specific range of temperatures is positively correlated with the amount of water present. To achieve 50% melt requires a temperature of ~1000 °C in the presence of 0.25 wt. % water, ~950 °C with 0.5 wt. % water, ~900 °C with 1 wt. % water, and only 800 °C for 2 wt. % water. We see that when the system is water-saturated, it behaves the same (in terms of volume % melt produced over a given temperature range) regardless of the specific water abundance, up to the point when all free water can be dissolved in the melt being generated (Figure 11).

Fiamme in the intracaldera tuff (including CRWPST) are > 60 to 65% melt (glass), but we hypothesize that a magma such as this could be mobilized with closer to ~50 % melt by volume (Bachman et al., 2007; Marsh, 1981). This degree of melting can be achieved with water contents as low as 0.25 wt. % with temperatures on the order of 1000 °C, or temperatures as low as 800 °C in the presence of 2 wt. % water. It is quite plausible that the amount of melt necessary to mobilize a basal cumulate in the PST magmatic system could be generated by the range of temperatures estimated from the rims of zircon in the intracaldera tuff.

CHAPTER VI

CONCLUSIONS

Our modeling efforts demonstrate that physical and chemical changes occurring within the Peach Spring magma body may have led to the destabilization and eventual eruption of the Peach Spring Tuff.

We determined that crystallization of rhyolitic melt may prompt physical changes that prime a magmatic system for eruption. Rhyolitic magma systems like the Peach Spring are vulnerable to sudden, potentially destabilizing, changes in density and volume upon reaching pseudo-invariant conditions during cooling and crystallization, but not all systems are affected equally. Systems with modest initial water contents experience larger changes than those with high initial water (e.g., ~15% change in density and volume in <10 °C cooling with 3 wt. % water at 200 and 250 MPa, but only 2% change for 7 wt. % water at 250 MPa).

Observations of accessory mineral textures and Ti-in-zircon temperatures from intracaldera fiamme (in a complementary study by Pamukcu, 2010) indicate that the Peach Spring magmatic system experienced heating and melting of a basal syenite cumulate, with recorded temperatures of ~900 °C. Our modeling demonstrates that near-solidus melting of a syenite cumulate at the base of the Peach Spring magma body is quite plausible, and that an eruptible (>50 % by volume) body of melt could have been generated in this way in the presence of 1-2 wt. % water at temperatures approaching 900 °C. This heating event, and subsequent melting and mobilization of melt, was likely related to the ultimate supereruption of the Peach Spring Tuff.

APPENDIX A

CL Images of Icelandic Zircon

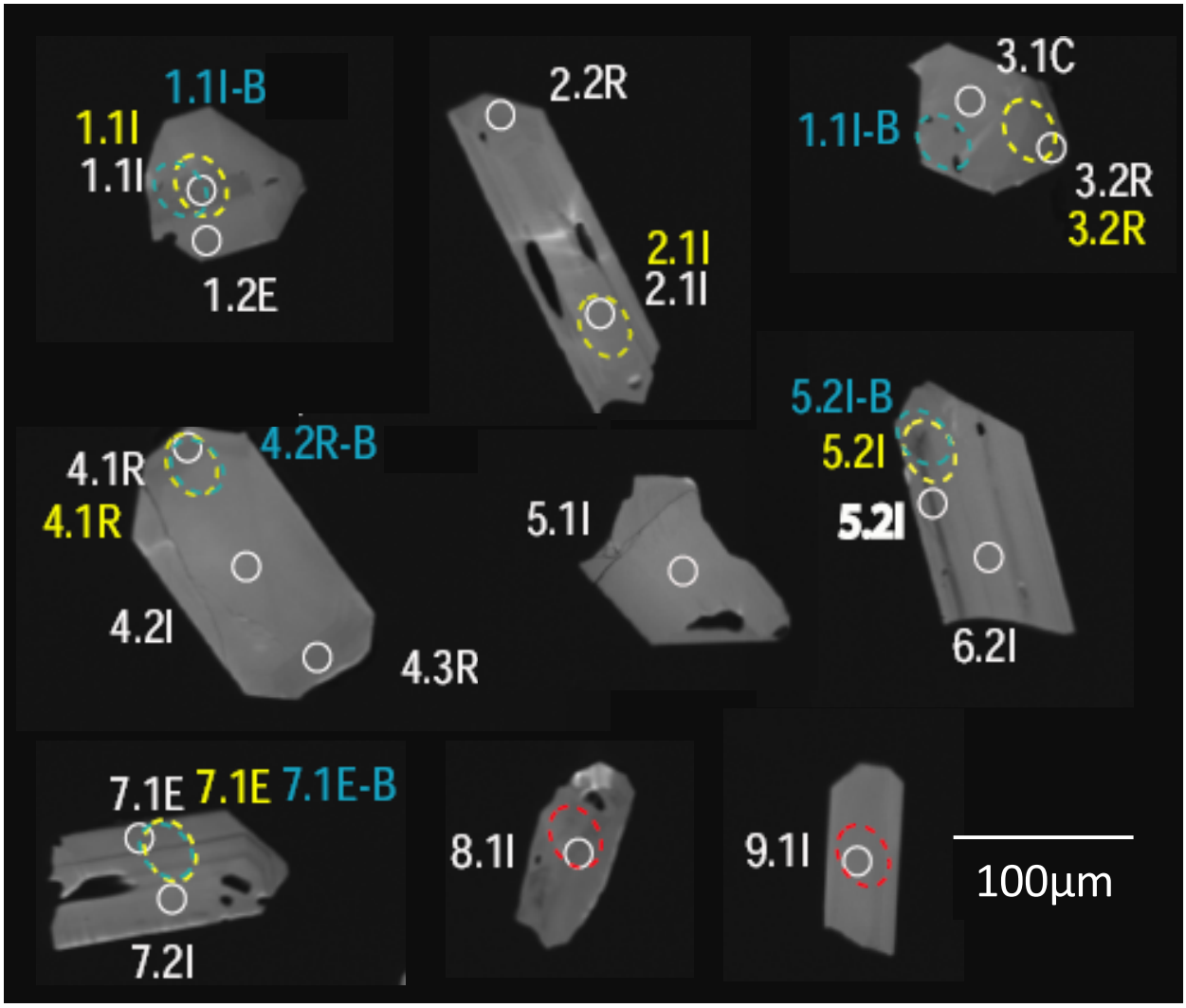

Appendix A.1

CL images of Askja 1875 AD zircons. White circles represent spots analyzed for trace elements using the SHRIMP-RG. Yellow and blue dashed ovals represent spots analyzed for U-Th disequlibrium dating using the SHRIMP-RG. Disregard red dashed ovals. Grain labels correspond to individual analyses shown in Appendix B.

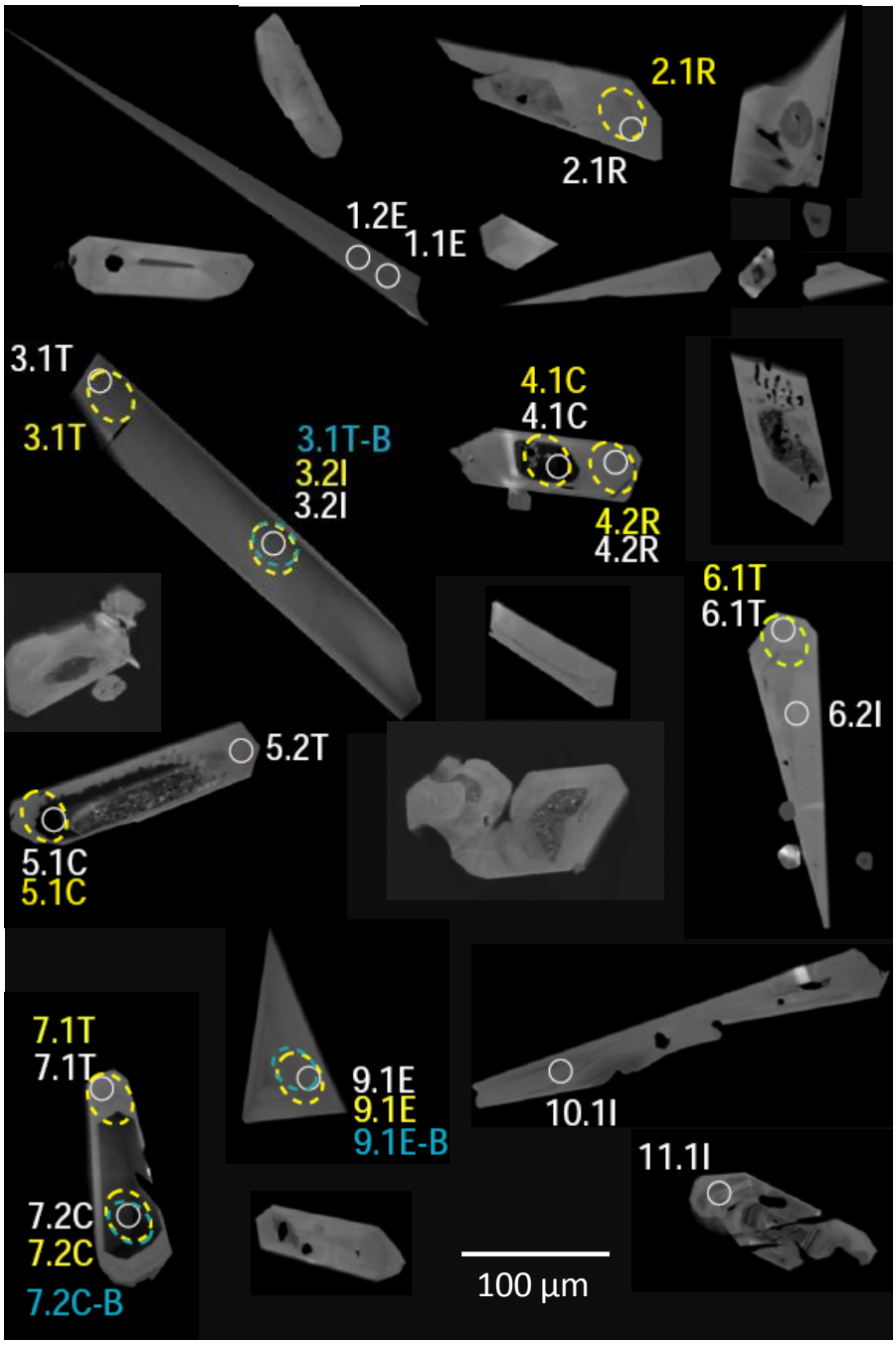

Appendix A.2

CL images of Oraefajokull 1362 AD zircons. White circles represent spots analyzed for trace elements using the SHRIMP-RG. Yellow and blue dashed ovals represent spots analyzed for U-Th disequlibrium dating using the SHRIMP-RG. Grain labels correspond to individual analyses shown in Appendix B.

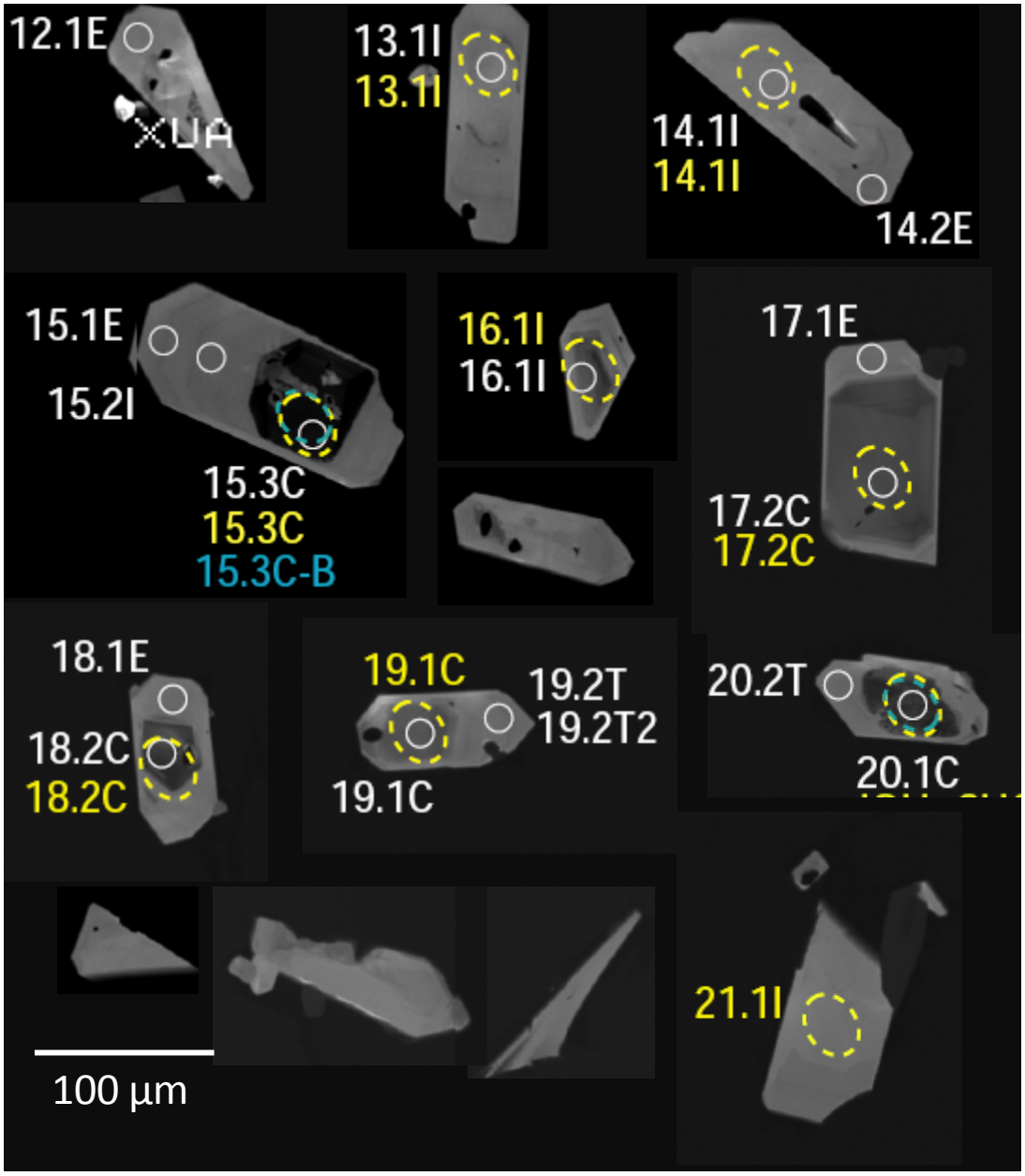

CL images of Oraefajokull 1362 AD zircons, continued.

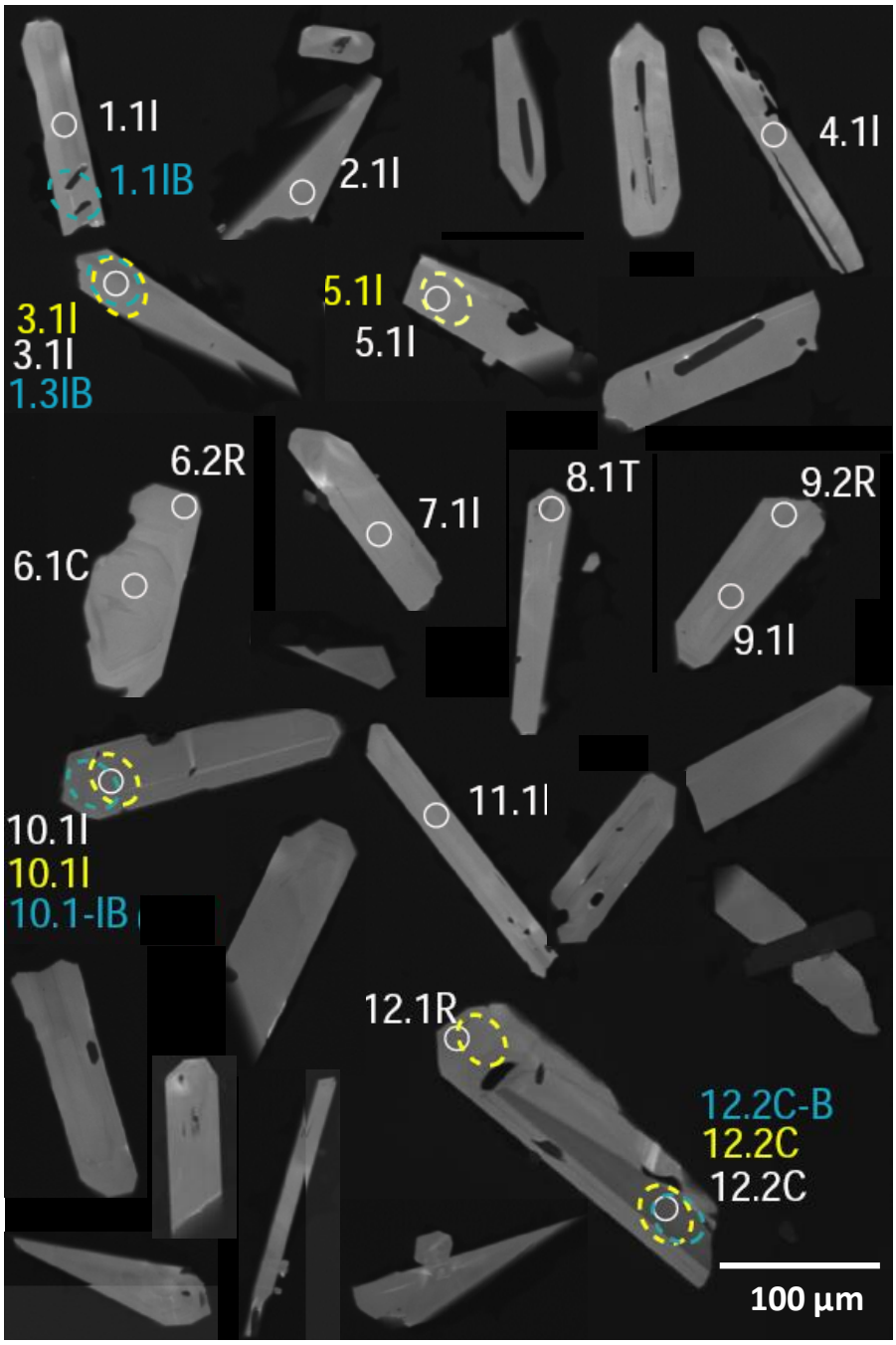

Appendix A.3

CL images of Hekla 1158 AD zircons. White circles represent spots analyzed for trace elements using the SHRIMP-RG. Yellow and blue dashed ovals represent spots analyzed for U-Th disequlibrium dating using the SHRIMP-RG. Grain labels correspond to individual analyses shown in Appendix B.

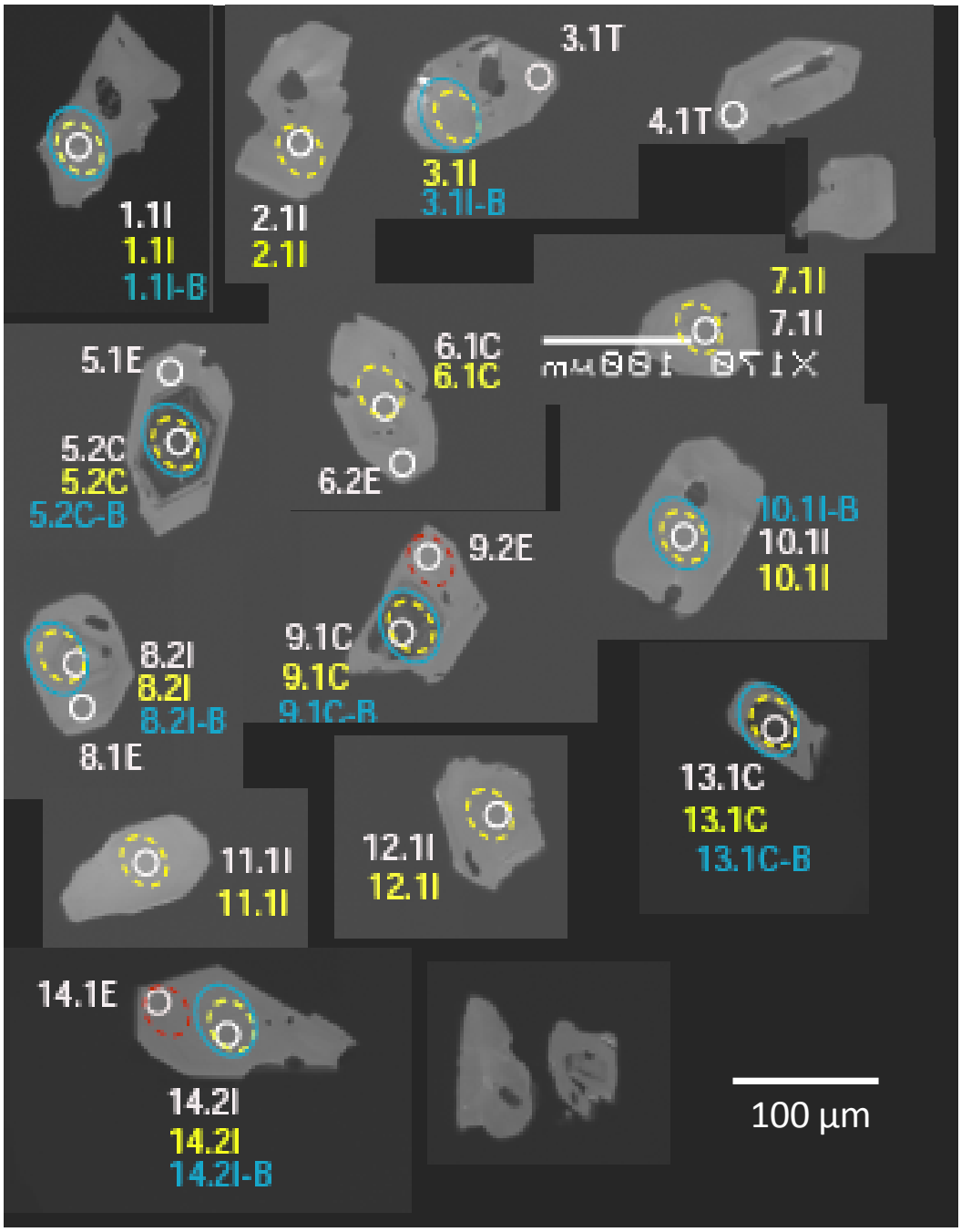

Appendix A.4

CL images of Torfajokull 1477 AD zircons. White circles represent spots analyzed for trace elements using the SHRIMP-RG. Blue ovals and yellow-dashed ovals represent spots analyzed for U-Th disequlibrium dating using the SHRIMP-RG. Grain labels correspond to individual analyses shown in Appendix B.

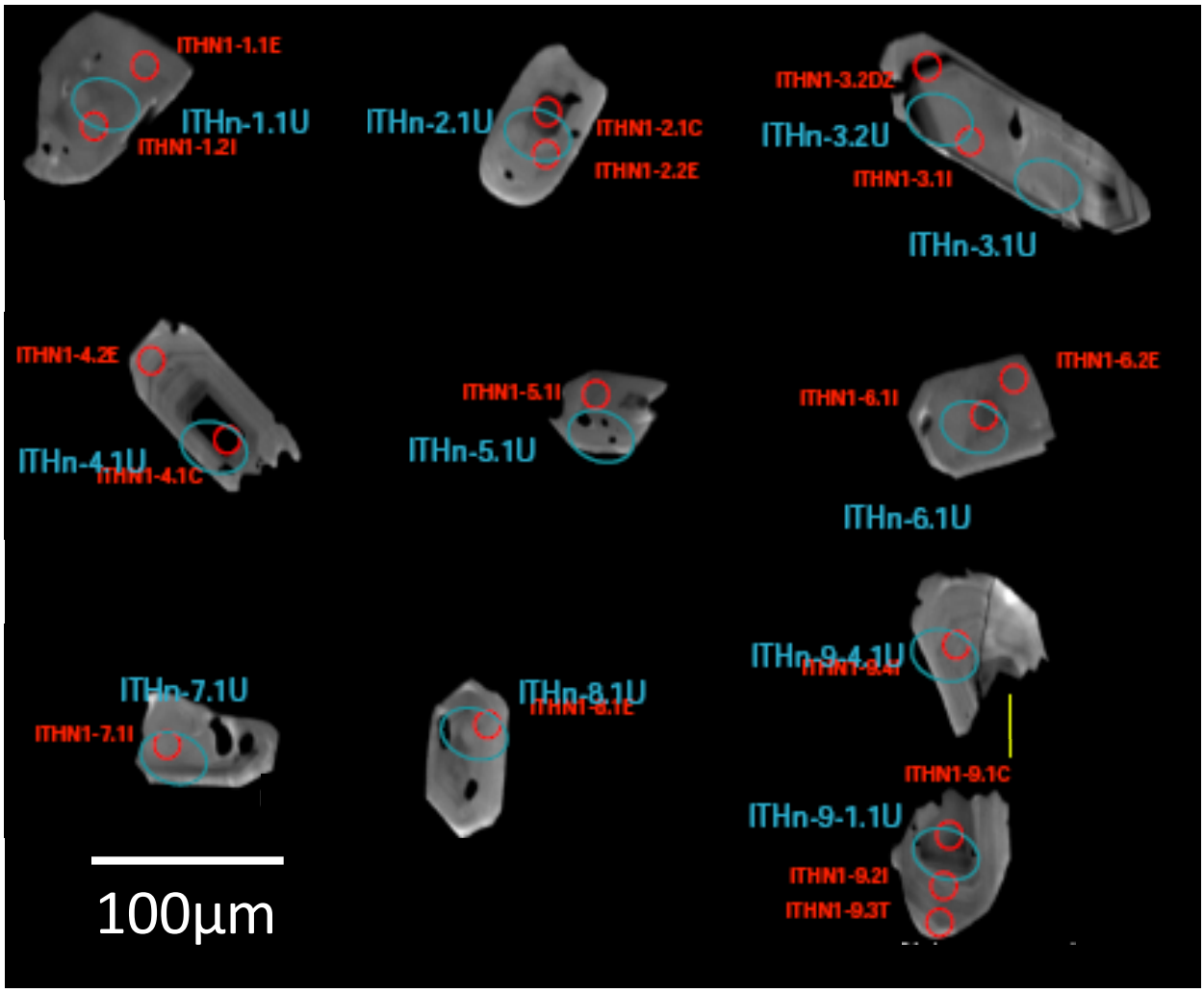

Appendix A.5

CL images of Torfajokull 871 AD zircons. Red circles represent spots analyzed for trace elements using the SHRIMP-RG. Blue ovals represent spots analyzed for U-Th disequlibrium dating using the SHRIMP-RG. Grain labels correspond to individual analyses shown in Appendix B.

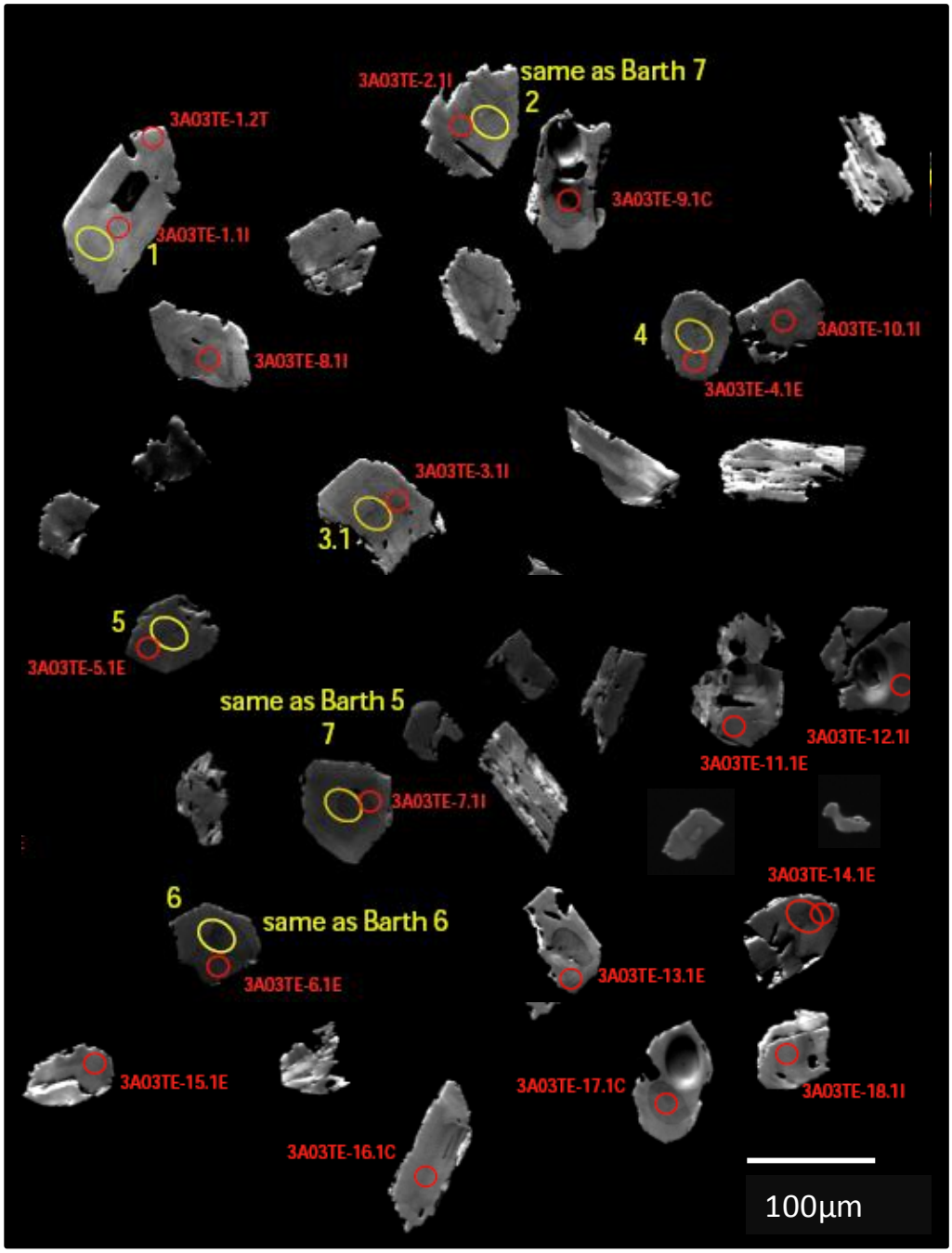

Appendix A.6

CL images of Torfajokull 3100 BP zircons. Red circles represent spots analyzed for trace elements using the SHRIMP-RG. Yellow ovals represent spots analyzed for U-Th disequlibrium dating using the SHRIMP-RG. Grain labels correspond to individual analyses shown in Appendix B. Spots labeled "same as Barth…" are spots that we re-analyzed after Brown et al. 2004.

Appendix A.7

CL images of Torfajokull 7500 BP zircons. Red circles represent spots analyzed for trace elements using the SHRIMP-RG. Yellow ovals represent spots analyzed for U-Th disequlibrium dating using the SHRIMP-RG. Grain labels correspond to individual analyses shown in Appendix B.

APPENDIX B

SHRIMP Trace Element Analyses of Individual Zircon Grains (Iceland)

Table B.1
SHRIMP Trace Element Analyses of Individual Zircon Grains from Askja 1875 AD

	Ti	Y	Nb	Hf	Th	U	La	Ce	Nd	Sm	Eu	Gd	Tb	Dy	Ho	Er	Tm	Yb	Lu
Total Iceland Av.	15.8	2874	40.2	8633	249.1	253.7	0.17	0.17	4.91	11.6	2.80	96.8	32.1	360.1	120.4	520.3	91.8	732.8	114.6
IC45-1.1I	23.2	2109	7.2	9494	32.7	53.3	0.05	7.51	3.94	8.7	1.92	66.9		243.4		331.5		421.0	62.6
IC45-1.2E	20.7	1658	5.6	9909	25.6	43.0	0.04	6.09	2.83	7.7	2.09	64.1		222.3		301.3		397.7	61.5
IC45-2.1I	29.0	1700	4.3	9260	25.9	39.5	0.05	5.39	4.51	8.7	2.42	66.2		238.1		309.0		406.0	62.4
IC45-2.2R	25.3	549	5.5	9101	10.3	23.3	0.04	3.34	0.51	1.6	0.53	17.0		67.4		105.8		159.5	26.7
IC45-3.1C	21.3	1359	5.3	9569	25.7	43.0	0.04	5.53	2.63	6.7	1.89	56.6		211.5		288.7		378.2	59.6
IC45-3.2R	24.4	1086	8.9	9178	40.1	67.9	0.03	7.04	1.49	4.1	1.10	33.8		145.9		215.1		316.6	50.8
IC45-4.1R	23.2	1102	10.3	9371	40.2	65.4	0.04	7.74	1.45	3.6	1.11	34.1		133.0		194.5		287.2	49.1
IC45-4.2I	19.8	1748	5.9	9684	29.3	49.1	0.04	6.43	3.18	8.8	2.17	69.5		236.7		320.8		416.9	64.5
IC45-4.3R	24.2	928	8.3	9470	23.4	46.3	0.03	5.97	0.91	3.5	0.87	28.4		121.3		179.1		269.8	42.2
IC45-5.1I	28.9	1551	4.3	9105	21.0	35.9	0.07	4.68	3.62	8.6	2.38	64.2		221.0		289.5		383.7	60.4
IC45-5.2I	23.0	2809	11.8	8827	56.2	75.0	0.06	10.26	6.18	14.5	3.52	113.8		373.7		481.2		635.3	96.1
IC45-6.2I	22.8	1244	4.9	9715	18.1	34.5	0.03	4.43	1.88	4.7	1.57	45.5		165.2		227.3		317.9	50.8
IC45-7.1E	19.0	2476	10.1	9824	52.2	82.3	0.08	11.11	5.42	11.2	2.63	90.7		310.8		424.9		543.8	81.6
IC45-7.2I	32.1	1432	3.8	9167	20.1	34.2	0.04	4.11	3.64	7.9	2.22	58.3		216.9		285.7		388.1	58.7
IC45-8.1I	20.3	813	10.0	10094	19.0	40.9	0.03	7.46	0.60	2.3	0.69	23.2		106.6		159.7		246.5	37.7
IC45-9.1I	22.6	1850	5.4	9427	28.7	47.3	0.07	6.47	4.43	9.9	2.35	71.2		245.6		334.2		434.3	66.0

Table B.2
SHRIMP Trace Element Analyses of Individual Zircon Grains from Hekla 1158 AD

	Ti	Y	Nb	Hf	Th	U	La	Ce	Nd	Sm	Eu	Gd	Tb	Dy	Ho	Er	Tm	Yb	Lu
Total Iceland Av.	15.8	2874	40.2	8633	249.1	253.7	0.17	0.17	4.91	11.6	2.80	96.8	32.1	360.1	120.4	520.3	91.8	732.8	114.6
IHB1-1.1I	18.9	3573	12.6	8129	117.9	175.9	0.05	12.29	6.97	17.7	6.36	130.7		492.7		711.7		1066.8	171.3
IHB1-10.1I	10.3	1527	7.5	9533	41.2	92.8	0.04	5.79	1.97	5.4	1.63	46.8		182.6		288.4		452.6	79.4
IHB1-11.1I	17.3	2678	9.1	8208	79.3	131.4	0.10	8.54	5.47	12.7	4.39	97.6		369.9		532.3		802.3	128.0
IHB1-12.1R	13.0	988	9.9	9468	47.4	109.6	0.02	7.22	0.81	2.4	0.86	22.7		108.6		186.4		313.7	53.6
IHB1-12.2C	14.6	6523	30.1	8207	308.5	313.0	0.15	40.72	15.20	37.9	13.11	272.4		918.9		1229.1		1734.9	282.3
IHB1-13.1I	8.4	1669	10.4	9712	103.7	143.0	0.04	16.64	2.58	6.9	3.11	68.2		319.2		494.6		778.9	128.7
IHB1-14.1I	7.4	1972	8.9	8502	46.4	101.4	0.06	9.70	3.31	7.5	2.27	65.9		257.6		378.8		512.2	77.4
IHB1-14.2R	36.5	1225	18.2	10466	45.1	107.9	0.18	10.29	1.04	3.0	0.71	28.8		144.4		255.6		426.6	69.8
IHB1-15.1I	15.8	1723	5.6	9272	41.4	81.1	0.11	5.71	2.52	6.5	2.21	52.1		202.0		308.3		477.8	80.2
IHB1-16.1I	18.5	5123	26.3	8088	136.1	194.2	0.15	20.70	10.28	23.7	7.46	165.2		590.6		815.4		1184.3	190.5
IHB1-17.1I	11.0	1781	5.3	9293	45.9	94.2	0.05	5.70	2.32	6.3	2.19	53.6		223.3		348.3		539.0	86.9
IHB1-18.1I	10.3	1759	5.0	9477	41.8	86.4	0.03	5.20	2.17	6.2	2.03	52.8		209.5		319.2		490.7	80.3
IHB1-19.1I	10.0	1643	5.3	9421	41.1	83.1	0.10	5.83	2.03	5.8	1.96	50.1		195.3		297.5		468.9	73.9
IHB1-2.1I	10.2	1741	5.4	9479	48.3	96.5	0.03	5.79	2.22	6.2	2.18	52.2		226.2		348.8		541.9	87.7
IHB1-20.1I	29.6	1627	6.2	9149	37.1	77.8	0.67	6.90	2.22	5.6	1.79	47.8		190.5		290.0		459.4	76.0
IHB1-21.2T	10.9	1323	5.1	9329	38.0	82.6	0.03	5.21	1.56	4.7	1.57	39.8		175.2		280.8		446.8	74.5
IHB1-22.1I	19.7	7090	36.1	7889	298.4	319.0	0.09	28.74	15.09	38.9	13.08	288.1		1016.2		1358.6		1901.9	298.1
IHB1-22.2I	14.8	2523	8.5	8666	72.6	133.8	0.06	7.96	4.54	11.6	4.08	89.9		358.7		507.8		770.6	122.8
IHB1-23.1I	15.1	5032	23.8	8522	239.8	324.2	0.08	18.98	7.28	20.9	6.84	176.5		718.9		1016.0		1521.0	242.7
IHB1-24.1I	22.1	2199	15.2	8185	69.7	130.6	0.10	8.67	2.37	7.3	2.69	63.1		277.5		430.7		690.4	115.6
IHB1-3.1I	12.7	2367	7.9	9058	91.5	145.3	0.05	6.35	2.94	9.4	3.41	86.0		347.1		517.9		793.8	129.1
IHB1-4.1I	17.2	2999	10.7	8636	86.1	142.7	0.08	8.51	6.10	14.1	4.63	109.3		379.2		548.8		816.1	137.2
IHB1-5.1I	11.1	1786	5.7	9389	51.4	104.5	0.05	6.08	2.58	6.1	1.92	53.2		228.2		353.8		530.3	88.9
IHB1-6.1C	14.8	677	7.7	8454	14.8	37.6	0.04	7.65	0.79	2.3	0.70	19.6		78.7		132.6		212.2	36.8
IHB1-6.2R	12.9	625	5.5	9794	22.5	69.9	0.03	4.76	0.42	1.8	0.62	15.6		78.3		138.3		246.1	41.9
IHB1-7.1I	10.0	1762	6.4	10553	42.7	86.3	0.05	6.27	2.46	6.2	2.13	57.7		215.7		323.9		502.9	86.4
IHB1-8.1T	14.0	1403	19.0	9763	198.6	271.2	1.90	17.94	4.06	4.7	1.57	42.3		198.6		336.9		570.7	96.3
IHB1-9.1I	13.0	2301	7.6	8883	74.0	123.7	0.05	6.21	2.85	8.6	3.22	75.7		281.4		433.3		673.5	113.5
IHB1-9.2R	17.8	2467	7.5	8387	67.9	112.5	0.07	7.25	4.55	11.3	4.09	87.6		325.9		463.6		723.8	120.2

Table B.3
SHRIMP Trace Element Analyses of Individual Zircon Grains from Oraefajokull 1362 AD

z	Ti	Y	Nb	Hf	Th	U	La	Ce	Nd	Sm	Eu	Gd	Tb	Dy	Ho	Er	Tm	Yb	Lu
Total Iceland Av.	15.8	2874	40.2	8633	249.1	253.7	0.17	0.17	4.91	11.6	2.80	96.8	32.1	360.1	120.4	520.3	91.8	732.8	114.6
IOHN1-1.2E	12.4	5832	24.2	6211	135.1	174.3	0.07	25.28	9.82	26.7	10.65	219.1		773.3		1043.7		1377.6	210.8
IOHN1-10.1I	8.8	1032	5.0	8663	16.5	38.3	0.04	5.20	0.96	3.2	1.17	28.5		121.2		193.3		291.6	47.0
IOHN1-11.1I	9.5	1369	15.2	8127	45.9	89.2	0.03	16.82	1.43	4.6	1.07	39.4		177.3		269.0		389.6	59.5
IOHN1-13.1I	9.8	1684	5.2	8309	35.0	66.8	0.05	6.28	2.16	6.6	2.16	55.1		229.1		331.9		480.0	73.3
IOHN1-14.1I	8.9	1757	6.9	8133	33.2	62.3	0.04	6.42	2.06	6.1	1.98	59.8		216.4		329.3		472.3	76.0
IOHN1-14.2E	11.6	741	6.3	7723	14.2	43.5	0.04	4.36	0.55	2.0	0.62	17.4		87.3		144.9		239.8	38.9
IOHN1-15.2I	13.0	820	7.3	8396	24.0	57.8	0.05	5.73	0.67	2.2	0.73	19.9		89.7		152.3		235.6	40.9
IOHN1-15.3C	16.9	18199	203.8	7744	1040.0	887.3	0.24	326.59	26.25	70.0	9.80	608.9		2330.5		3190.5		3966.4	549.8
IOHN1-16.1I	9.2	6952	44.8	7868	274.6	322.1	0.12	60.16	9.92	28.8	6.17	251.6		877.0		1211.8		1597.2	236.7
IOHN1-17.1E	11.7	824	6.9	8150	29.6	63.1	0.04	6.63	0.71	2.3	0.82	21.6		103.0		167.2		266.7	42.9
IOHN1-17.2C	9.2	9131	56.5	7339	308.9	371.1	0.12	87.97	14.52	40.1	10.04	326.6		1238.5		1705.1		2207.4	321.4
IOHN1-18.1E	14.6	991	9.0	8047	40.1	78.8	0.02	7.53	0.77	2.8	0.97	25.5		123.7		201.5		321.7	49.7
IOHN1-19.1C	10.6	5234	62.3	8110	367.7	389.5	0.38	69.57	6.17	18.9	3.79	176.5		694.4		984.7		1286.4	194.0
IOHN1-19.2T2	12.0	1027	8.4	7627	29.8	65.5	0.04	7.66	0.95	2.9	0.97	25.2		118.6		192.3		297.9	48.6
IOHN1-2.1R	11.6	921	8.0	8567	23.8	58.7	0.04	6.44	0.66	2.0	0.88	21.0		97.0		171.7		269.1	43.8
IOHN1-3.1T	11.6	7104	40.4	7294	203.8	241.3	0.08	37.03	9.32	30.2	9.87	252.6		946.2		1283.3		1697.2	254.6
IOHN1-3.2I	12.0	8016	44.8	7019	257.9	277.4	0.13	50.09	13.30	36.1	11.96	315.4		1070.7		1448.7		1852.1	280.0
IOHN1-4.1C	29.1	18996	166.4	7336	893.3	761.4	0.32	351.38	37.51	93.0	12.34	689.4		2577.6		3344.6		4104.4	570.2
IOHN1-4.2R	12.8	1558	22.7	8982	119.9	147.0	0.04	16.31	1.17	4.3	1.23	41.5		170.6		262.8		391.1	65.1
IOHN1-5.1C	20.3	12297	772.2	9008	1494.9	1593.0	0.22	357.54	8.90	25.0	4.03	232.8		1360.5		2290.2		3489.5	491.4
IOHN1-5.2T	12.8	914	8.2	8183	28.6	63.3	0.03	6.79	0.70	2.1	0.81	22.7		104.4		176.6		278.9	45.1
IOHN1-7.1T	12.7	978	8.7	7908	33.9	71.2	0.02	7.31	0.91	2.6	0.88	24.0		113.0		185.0		294.9	46.6
IOHN1-7.2C	12.4	12592	88.2	7471	583.4	554.2	0.18	104.52	22.48	59.4	12.11	487.0		1684.5		2242.5		2842.0	422.9
IOHN1-8.1I	12.6	1140	5.6	8985	28.2	51.1	0.11	6.46	1.02	3.2	1.04	31.7		132.0		205.7		341.8	53.9
IOHN1-9.1E	11.8	5106	20.6	6718	126.6	173.8	0.08	22.28	8.21	22.5	8.67	188.2		655.9		890.4		1204.1	189.2

Table B.4
SHRIMP Trace Element Analyses of Individual Zircon Grains from Torfajokull 1477 AD

	Ti	Y	Nb	Hf	Th	U	La	Ce	Nd	Sm	Eu	Gd	Tb	Dy	Ho	Er	Tm	Yb	Lu
Total Iceland Av.	15.8	2874	40.2	8633	249.1	253.7	0.17	0.17	4.91	11.6	2.80	96.8	32.1	360.1	120.4	520.3	91.8	732.8	114.6
ITN1-1.1I	19.2	801	9.5	9168	56.1	84.9	0.06	20.84	0.88	2.4	0.69	20.8		87.7		144.7		244.0	39.7
ITN1-10.1I	12.2	2588	13.9	9310	160.0	221.4	0.04	23.31	5.13	10.2	1.59	74.7		326.1		484.5		728.5	109.1
ITN1-11.1I	15.9	1727	8.2	9579	83.1	112.3	0.07	17.96	3.41	7.0	1.66	55.5		198.3		293.4		431.0	71.3
ITN1-12.1I	19.1	2578	12.9	8832	150.9	178.0	0.09	26.67	4.94	11.0	2.80	86.7		342.4		494.4		728.5	112.3
ITN1-14.1E	16.3	915	9.7	9535	63.9	112.7	0.03	18.37	1.11	3.0	0.77	22.6		108.7		175.6		295.0	46.8
ITN1-14.2I	19.4	1631	12.9	8858	109.4	152.6	0.03	26.10	3.11	6.2	1.60	45.8		216.2		334.8		501.4	81.1
ITN1-2.1I	18.4	2376	43.9	9058	179.9	300.6	0.05	46.68	2.69	6.1	1.32	54.8		261.3		467.8		785.5	130.0
ITN1-3.1T	21.3	1741	22.6	9064	308.6	277.9	0.04	39.12	2.56	5.6	1.30	50.2		211.7		331.2		519.6	82.5
ITN1-4.1T	21.8	1191	14.1	8882	149.1	183.8	0.04	25.23	1.67	3.9	0.98	30.6		144.0		230.3		375.9	59.4
ITN1-5.1E	15.1	1217	17.0	9541	133.1	196.2	0.03	25.63	1.50	3.4	0.70	30.1		138.2		223.8		359.3	57.4
ITN1-5.2C	10.2	8213	184.2	8942	1682.9	1943.4	0.13	166.91	12.37	29.3	0.84	238.0		1169.6		1812.8		2717.7	391.7
ITN1-6.1C	12.4	3135	17.7	9472	171.8	225.0	0.09	26.60	5.46	11.8	2.11	96.8		363.0		520.1		740.9	115.7
ITN1-6.2E	14.4	852	10.7	9879	75.0	106.7	0.03	18.94	0.88	2.2	0.51	20.3		93.9		156.6		265.4	42.6
ITN1-7.1I	16.6	3086	28.1	9482	203.9	267.4	0.08	38.07	5.01	11.2	2.37	95.3		381.3		572.5		854.4	137.2
ITN1-8.1E	17.2	1741	27.2	9003	245.0	286.2	0.06	37.33	2.33	5.7	1.03	46.1		214.6		335.0		519.0	81.9
ITN1-8.2I	12.5	2085	29.7	9318	143.6	233.8	0.04	30.09	2.47	5.9	1.10	57.3		219.4		367.6		599.0	98.2
ITN1-9.2E	16.8	1109	12.3	8955	72.5	115.3	0.04	24.91	1.44	3.0	0.91	28.4		129.6		202.0		324.2	52.3

Table B.5
SHRIMP Trace Element Analyses of Individual Zircon Grains from Torfajokull 871 AD

Total Iceland Av.	15.8	2874	40.2	8633	249.1	253.7	0.17	0.17	4.91	11.6	2.80	96.8	32.1	360.1	120.4	520.3	91.8	732.8	114.6
ITHN1-1.1E	12.7	3136	23.6	9151	218.8	263.0	0.14	29.60	6.45	11.9	2.18	104.1	34.7	368.3	136.4	552.2	106.3	787.0	128.3
ITHN1-1.2I	17.6	1845	34.0	8964	292.7	295.3	0.04	42.93	2.66	6.0	1.15	53.7	18.8	208.0	75.3	321.3	62.5	475.5	77.5
ITHN1-2.1C	20.6	6651	62.0	8763	612.6	598.8	9.13	116.95	19.14	33.5	4.21	256.6	80.6	828.0	290.4	1143.1	217.1	1576.6	250.0
ITHN1-2.2E	17.8	1878	34.7	9482	211.5	261.7	0.04	46.70	2.68	6.2	1.17	57.7	19.8	213.2	79.2	330.9	66.3	497.8	82.8
ITHN1-3.1I	11.2	2012	17.5	9220	113.8	96.5	0.06	23.33	4.20	8.1	1.49	68.0	21.5	231.5	83.7	334.4	64.6	484.9	78.1
ITHN1-3.2DZ	12.3	3981	170.9	9481	801.2	908.5	0.11	142.42	5.01	12.3	1.18	119.6	43.0	460.8	169.4	708.4	138.6	1068.7	167.6
ITHN1-4.1C	13.7	8457	391.3	9379	3829.0	2277.8	0.26	380.37	13.88	31.5	2.14	281.2	102.2	1066.6	364.5	1498.5	277.5	2082.3	296.1
ITHN1-4.2E	15.8	1859	37.4	9096	317.6	320.8	0.07	45.72	2.70	6.0	1.05	53.4	18.8	202.9	76.9	315.4	62.9	471.1	75.5
ITHN1-5.1I	14.8	3012	32.0	9020	234.9	277.5	0.12	37.81	5.32	10.9	2.12	101.2	32.0	350.2	129.6	524.8	100.6	765.8	122.8
ITHN1-6.1I	18.8	2125	41.4	8615	730.9	503.2	0.03	53.75	3.40	6.7	1.26	62.4	21.9	237.9	90.1	372.1	69.9	538.8	87.1
ITHN1-6.2E	13.0	3441	28.6	8854	258.7	299.7	0.11	33.69	6.48	12.7	2.55	117.4	39.4	413.5	147.7	603.1	113.4	851.7	136.8
ITHN1-7.1I	13.1	2303	22.6	9276	149.9	202.3	0.37	27.82	5.19	8.9	1.59	72.8	24.5	260.5	96.6	398.1	75.5	573.9	92.7
ITHN1-8.1E	20.8	2413	20.0	9339	159.0	194.4	0.14	29.21	4.78	8.9	2.02	77.9	26.4	288.4	102.9	428.5	81.8	635.3	101.7
ITHN1-9.1C	14.5	4990	53.0	9194	406.5	474.6	0.36	66.70	9.33	19.8	1.72	168.2	56.6	584.8	212.1	854.2	162.0	1208.3	195.0
ITHN1-9.2I	14.3	2094	49.1	9565	456.8	476.8	0.06	59.35	3.03	7.5	0.86	65.8	22.3	243.3	88.8	370.7	70.9	558.1	88.9
ITHN1-9.3T	16.0	1886	40.1	9408	415.5	404.3	0.06	48.15	2.58	5.9	1.02	54.7	19.4	207.7	77.9	320.8	63.3	488.4	78.7
ITHN1-9.4I	14.7	1419	30.0	9233	192.0	247.0	0.04	34.48	1.88	4.6	0.67	39.0	13.8	150.6	58.3	239.5	48.2	369.9	62.3

Table B.6
SHRIMP Trace Element Analyses of Individual Zircon Grains from Torfajokull 3100 BP

Z	Ti	Y	Nb	Hf	Th	U	La	Ce	Nd	Sm	Eu	Gd	Tb	Dy	Ho	Er	Tm	Yb	Lu
Total Iceland Av.	15.8	2874	40.2	8633	249.1	253.7	0.17	0.17	4.91	11.6	2.80	96.8	32.1	360.1	120.4	520.3	91.8	732.8	114.6
3A03TE-1.1I	20.8	1340	30.6	8993	128.8	158.8	0.14	23.58	5.24	10.9	2.79	98.7	32.4	331.0	119.8	480.5	92.9	688.7	113.7
3A03TE-1.2T	19.5	940	22.4	8627	97.9	131.6	0.03	21.88	1.53	3.3	0.87	31.8	11.3	122.4	47.9	212.3	43.1	334.7	59.0
3A03TE-8.1I	20.3	2970	36.6	8263	210.3	236.2	0.03	16.19	1.64	3.3	0.93	29.5	10.4	118.1	44.6	191.9	37.4	292.0	49.1
3A03TE-3.1I	22.5	2493	47.7	8195	192.2	253.5	0.15	30.83	6.68	14.0	3.33	110.8	36.0	374.6	136.5	529.5	101.7	774.4	121.8
3A03TE-2.1I	23.4	2030	35.1	8250	155.6	199.0	0.02	24.89	1.76	4.1	0.96	34.1	11.3	127.3	48.9	210.4	41.8	320.3	54.5
3A03TE-9.1C	22.7	2607	40.4	8899	392.3	318.1	0.03	19.53	1.15	3.3	0.79	26.9	9.2	99.9	38.8	167.5	33.3	260.1	45.1
3A03TE-4.1E	17.8	1237	21.5	8334	99.7	142.1	0.03	20.71	1.51	2.7	0.71	27.4	9.8	106.4	40.4	173.6	34.0	266.2	46.1
3A03TE-10.1I	21.1	2102	40.6	8659	189.0	254.5	0.12	37.21	4.76	10.9	2.74	95.2	31.3	332.2	124.5	516.4	100.7	763.4	126.1
3A03TE-5.1E	25.7	1546	29.0	8709	358.7	283.7	0.17	34.43	6.18	13.3	3.31	114.2	37.9	386.4	138.1	560.0	109.0	806.6	130.9
3A03TE-6.1E	20.6	3272	32.6	8873	226.4	245.6	0.06	26.37	2.28	4.3	1.15	36.3	13.1	146.1	55.9	234.6	46.2	362.3	61.6
3A03TE-7.1E	21.0	2387	31.3	8135	231.4	220.0	0.13	39.56	4.48	8.8	2.17	75.0	25.7	271.2	98.5	414.3	78.4	606.2	100.0
3A03TE-11.1E	18.6	1099	16.2	7899	126.5	162.0	0.04	32.73	2.61	5.5	1.46	51.1	18.6	212.2	83.8	385.8	76.8	614.8	106.1
3A03TE-12.1I	19.6	979	22.1	8997	97.0	131.3	0.02	25.79	1.95	3.5	0.94	32.0	11.9	133.0	53.4	232.1	47.3	374.3	65.7
3A03TE-13.1E	21.1	1307	24.5	8546	143.6	182.9	0.04	28.94	2.03	4.3	1.10	37.2	13.5	142.1	54.8	226.9	43.6	342.4	57.6
3A03TE-14.1E	22.5	1413	28.7	8574	274.7	248.6	0.03	28.35	2.33	4.6	1.05	37.9	14.4	153.1	56.2	247.3	49.1	371.2	61.2
3A03TE-15.1E	21.2	1343	26.1	8413	202.3	193.2	0.08	40.72	3.24	6.1	1.48	56.6	20.3	235.2	96.4	425.8	86.1	660.9	113.3
3A03TE-16.1C	18.7	3240	28.1	8560	202.5	220.8	0.10	49.24	4.58	9.8	2.12	84.0	28.4	298.2	108.1	444.6	85.1	615.0	101.5
3A03TE-17.1C	19.4	1195	25.0	8794	150.3	156.2	0.07	36.22	3.18	6.2	1.54	53.8	18.0	202.7	80.9	356.4	71.3	571.9	96.8
3A03TE-18.1I	17.0	2869	23.3	8517	175.6	207.2	0.04	32.58	2.60	4.9	1.20	43.1	14.9	164.9	62.9	269.1	53.1	415.8	69.9

Table B.7
SHRIMP Trace Element Analyses of Individual Zircon Grains from Torfajokull 7500 BP

z	Ti	Y	Nb	Hf	Th	U	La	Ce	Nd	Sm	Eu	Gd	Tb	Dy	Ho	Er	Tm	Yb	Lu
5A03TE-1.1	15.7	4927	146.6	6815	1413.7	812.3	0.11	342.74	8.71	22.4	5.77	209.0	67.0	658.2	218.3	837.5	145.7	1014.4	149.2
5A03TE-10.1I	31.9	4528	31.5	7310	297.0	279.7	0.23	29.66	15.43	27.9	10.05	191.3	56.2	545.1	192.0	754.4	145.5	1076.0	178.9
5A03TE-11.1I	9.1	1479	38.7	7111	110.6	146.7	0.01	56.94	2.37	5.0	1.29	49.8	16.8	178.1	66.4	270.6	49.6	364.1	57.5
5A03TE-12.1C	14.3	1883	38.6	8470	300.5	254.4	0.06	55.41	3.16	6.3	1.87	61.2	21.0	226.0	81.0	340.0	63.7	478.7	78.6
5A03TE-13.1I	14.3	2380	37.8	7655	146.9	143.8	0.14	79.39	4.64	10.1	2.81	79.7	28.1	283.6	101.7	422.4	76.8	566.3	94.5
5A03TE-14.1I	17.5	3689	29.2	7382	463.9	497.5	0.16	27.55	10.35	19.0	4.75	133.7	42.5	431.1	151.0	626.1	124.8	977.9	161.3
5A03TE-15.1I	7.7	3197	33.3	7666	119.5	165.4	0.14	45.24	5.66	13.0	3.20	117.6	39.1	400.2	142.2	555.1	101.3	696.2	112.7
5A03TE-15.2E	8.1	1438	41.1	8967	145.1	223.4	0.04	51.13	2.03	4.7	0.86	41.4	15.3	162.2	61.4	259.0	50.1	363.3	58.0
5A03TE-16.1C	8.5	3103	52.0	6808	122.5	169.7	0.10	59.01	5.36	11.8	3.09	105.7	34.5	367.1	131.7	524.7	96.4	712.5	112.1
5A03TE-17.1C	13.9	6652	126.6	9084	2165.9	1404.4	0.37	223.41	13.98	29.2	5.36	251.6	86.7	891.7	310.5	1263.8	238.1	1731.7	265.9
5A03TE-18.1I	10.3	1837	46.9	7723	200.9	229.8	0.04	74.83	2.63	6.2	1.51	61.1	21.3	223.3	78.9	318.2	59.6	431.6	68.2
5A03TE-19.1I	12.5	1256	22.6	8710	56.2	85.9	0.03	16.44	2.49	4.8	1.46	45.8	14.6	159.6	55.3	231.5	43.6	337.9	54.6
5A03TE-2.1I	5.9	5397	64.0	7753	231.1	314.4	0.11	92.16	10.97	24.9	6.94	206.3	69.6	720.3	246.9	967.1	173.7	1210.9	184.7
5A03TE-2.2E	10.7	1404	115.1	11335	339.0	321.2	0.11	55.24	2.22	5.2	1.24	41.6	16.9	183.7	63.2	281.8	55.8	437.5	65.3
5A03TE-20.1I	22.9	2511	34.3	7521	346.8	317.1	0.09	30.90	4.14	8.8	2.81	74.7	26.4	264.8	103.6	416.5	79.8	592.9	99.8
5A03TE-21.1E	8.9	2112	60.5	8253	313.1	345.2	0.05	84.95	3.19	6.8	1.47	66.6	22.7	243.7	92.3	354.2	68.3	486.8	76.0
5A03TE-21.2C	14.9	2348	65.0	7525	383.5	393.1	1.05	101.81	4.15	8.5	1.95	75.6	27.1	279.1	99.5	395.0	73.5	512.7	83.1
5A03TE-22.1C	17.2	6587	220.3	7442	1133.7	502.1	0.67	886.12	16.01	34.0	7.67	268.4	82.9	833.2	295.8	1104.5	196.4	1363.7	199.3
5A03TE-22.2E	12.1	1893	52.4	8389	326.6	313.2	0.03	67.57	2.88	6.5	1.63	60.9	21.1	218.4	81.7	325.3	59.9	442.3	71.3
5A03TE-23.1E	21.8	4555	36.4	7374	302.8	327.4	0.24	31.91	14.99	27.9	8.53	192.9	58.8	575.4	199.8	781.6	149.9	1079.3	179.0
5A03TE-24.1C	8.1	3909	49.8	7514	221.1	264.1	0.14	87.46	6.49	17.8	4.09	155.1	49.8	509.3	177.0	695.6	127.8	892.3	138.8
5A03TE-24.2E	9.8	2680	70.9	7982	365.6	387.3	0.04	114.14	3.68	8.4	1.82	93.2	30.2	321.5	115.4	452.9	82.9	608.6	96.2

(Continued)

Table B.7 (Continued)
SHRIMP Trace Element Analyses of Individual Zircon Grains from Torfajokull 7500 BP

5A03TE-25.1E	9.8	1503	35.0	7545	180.3	197.8	0.04	57.72	2.30	5.5	1.31	50.3	16.0	173.8	64.5	261.6	48.0	349.6	55.9
5A03TE-25.2C	8.4	2241	33.3	8031	105.8	145.5	0.40	39.80	4.60	9.5	2.13	85.7	26.9	273.2	99.6	385.9	71.2	519.1	80.1
5A03TE-3.1I	6.5	4479	43.9	7606	219.5	284.6	0.12	68.40	7.96	18.7	4.15	161.1	54.5	548.5	194.1	757.5	139.3	979.9	151.7
5A03TE-4.1C	10.6	2471	62.0	7137	343.8	303.8	0.05	117.85	4.45	8.7	2.45	83.8	28.7	299.0	107.4	416.6	75.6	533.3	84.7
5A03TE-4.1C	12.1	9983	210.1	6775	1095.2	927.6	0.31	405.52	20.31	47.6	9.10	386.1	127.2	1285.4	450.8	1698.3	300.3	2093.7	313.2
5A03TE-6.1I	10.2	2063	55.7	7080	269.1	268.5	0.06	91.66	3.22	7.6	1.81	72.1	24.9	255.8	91.0	365.1	66.8	471.8	73.6
5A03TE-7.1C	13.5	2838	65.3	8313	261.4	290.5	0.06	73.51	3.95	9.7	2.07	88.9	30.4	331.0	121.3	503.1	95.6	739.0	119.9
5A03TE-7.1E	11.1	1462	36.6	9533	170.1	222.4	0.03	43.85	1.80	4.6	0.92	40.9	14.7	171.0	61.1	259.0	50.2	378.6	59.7
5A03TE-7.2I	6.3	2727	36.2	7550	104.9	158.3	0.08	35.27	5.54	10.6	2.78	103.7	32.7	342.6	122.5	485.5	90.8	640.0	97.2
5A03TE-8.1C	11.9	2722	39.9	7055	127.6	158.2	1.13	50.49	5.94	12.6	3.14	107.6	34.0	349.9	122.6	489.2	89.2	637.6	101.1
5A03TE-8.2E	9.3	1016	26.2	9008	60.3	118.6	0.05	28.01	1.31	3.2	0.69	27.6	10.4	115.6	42.3	182.6	37.0	285.9	45.3
5A03TE-9.1E	10.1	2694	78.3	8075	620.2	520.6	0.05	119.70	4.10	9.7	2.16	88.0	31.7	331.6	115.1	466.4	84.5	595.2	95.3

APPENDIX C

Matrix Overview of Modeling Results

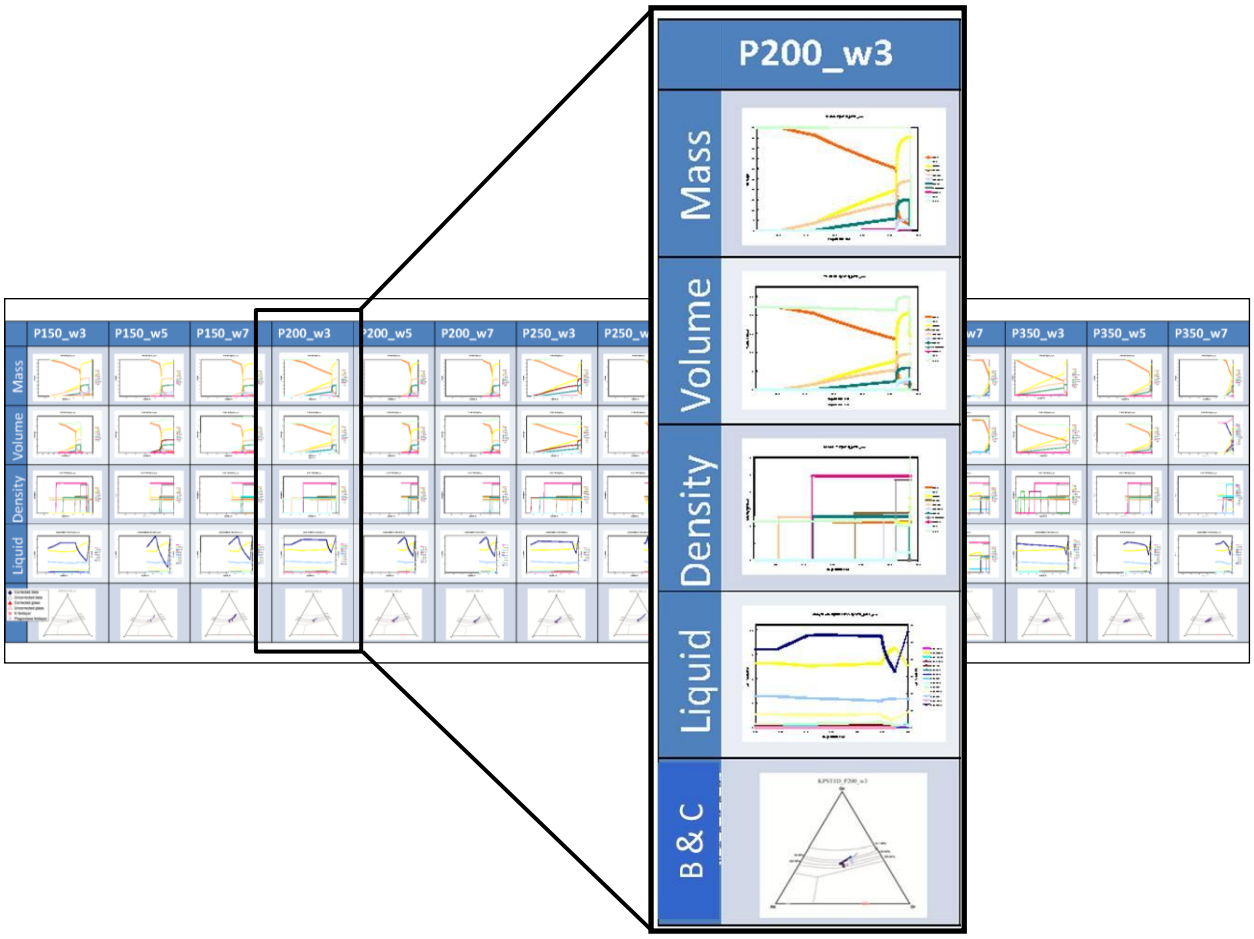

Appendix C

Master matrix created to compare model outputs for melting simulations run with a composition of KPST01D, variable water contents and variable pressures. All results shown here are from runs conducted with equilibrium crystallization, pressures from 150 MPa to 350 MPa (in 50 MPa increments) and initial water contents of 3, 5, and 7 wt. %. In this compilation, each column represents a single simulation (e.g., 250 MPa and 3 wt. % water in the blown-up example) and each row represents a different type of data generated (e.g., mass, volume and density of individual phases and the total system, changing composition of the liquid, and composition of the evolving liquid projected onto a Qz-Or-Ab ternary diagram with experimental cotectics drawn in (in the style of Blundy and Cashman, 2001; "B&C"). More complete results can be seen found in Appendix D.

APPENDIX D

Plotted Model Outputs for Melting Simulations

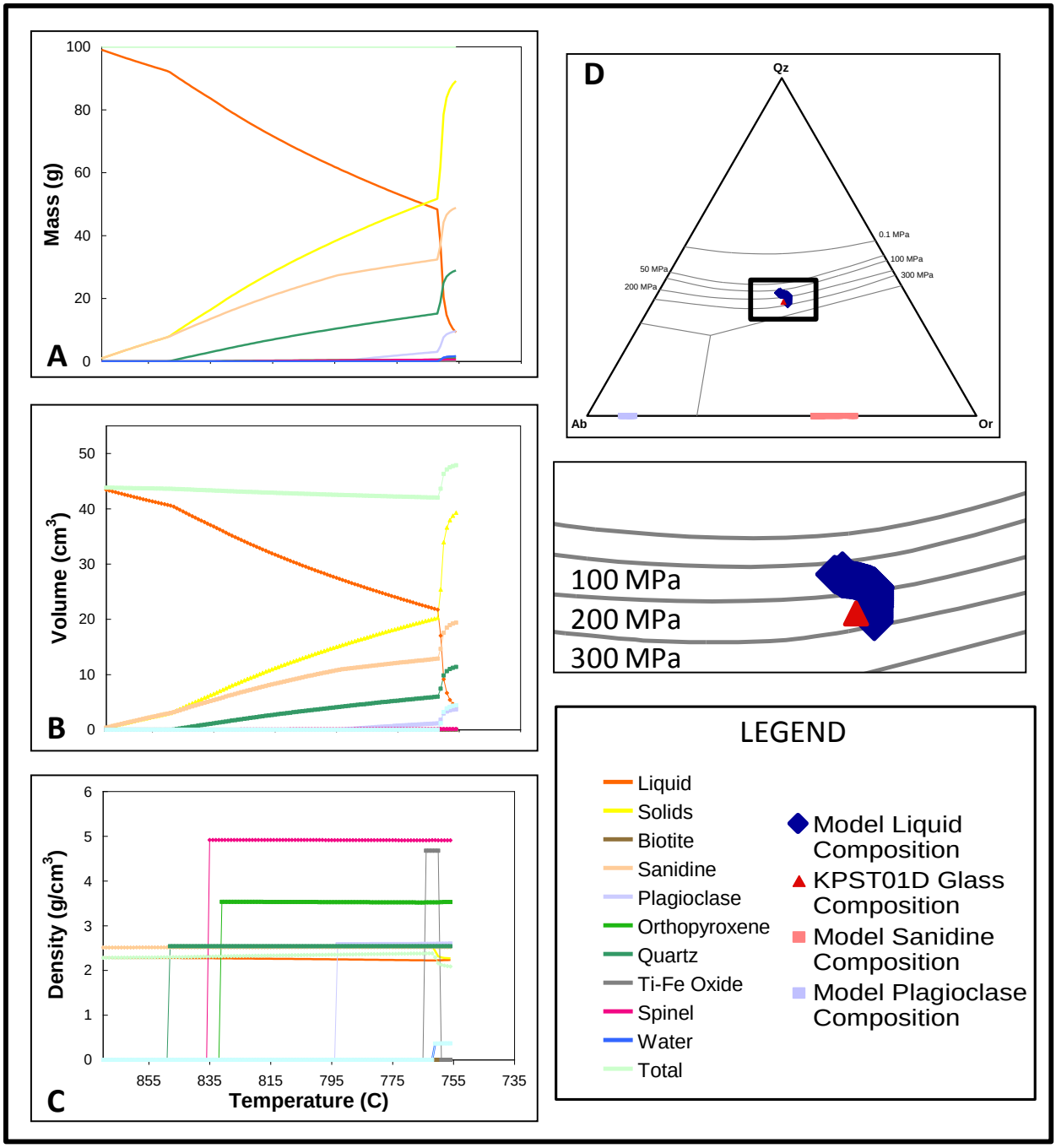

Data from one simulation run with equilibrium crystallization, composition KPST01D, 150 MPa and 2 wt. % water: (A) mass, (B) volume (C) density, (D) evolution of melt compositions on the Qz-Ab-Or ternary (using the Blundy and Cashman, 2001 projection scheme) with cotectic pressures in the zoomed-in box placed below the cotectic curve to which they correspond.

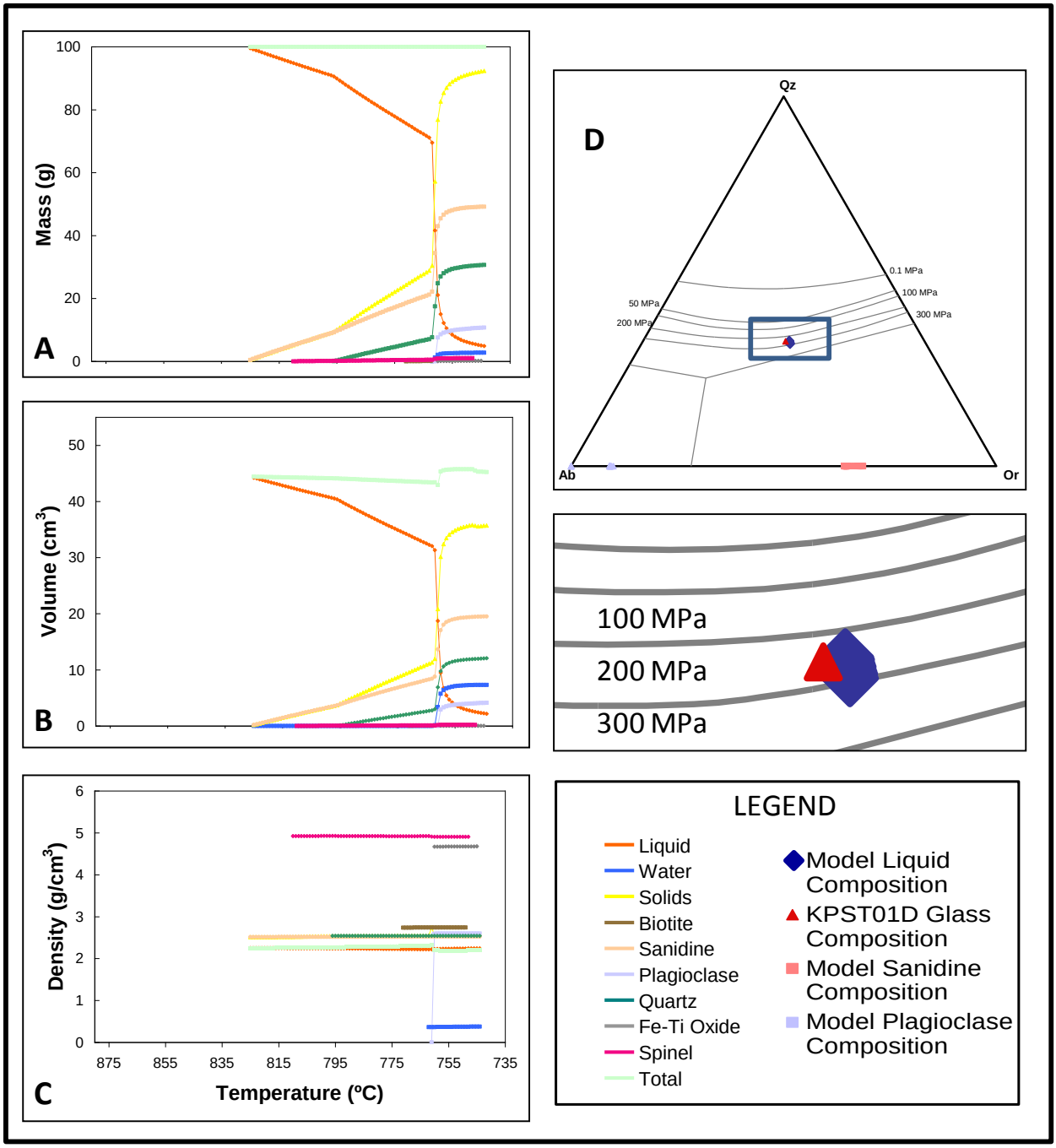

Data from one simulation run with equilibrium crystallization, composition KPST01D, 150 MPa and 3 wt. % water: (A) mass, (B) volume (C) density, (D) evolution of melt compositions on the Qz-Ab-Or ternary (using the Blundy and Cashman, 2001 projection scheme) with cotectic pressures in the zoomed-in box placed below the cotectic curve to which they correspond.

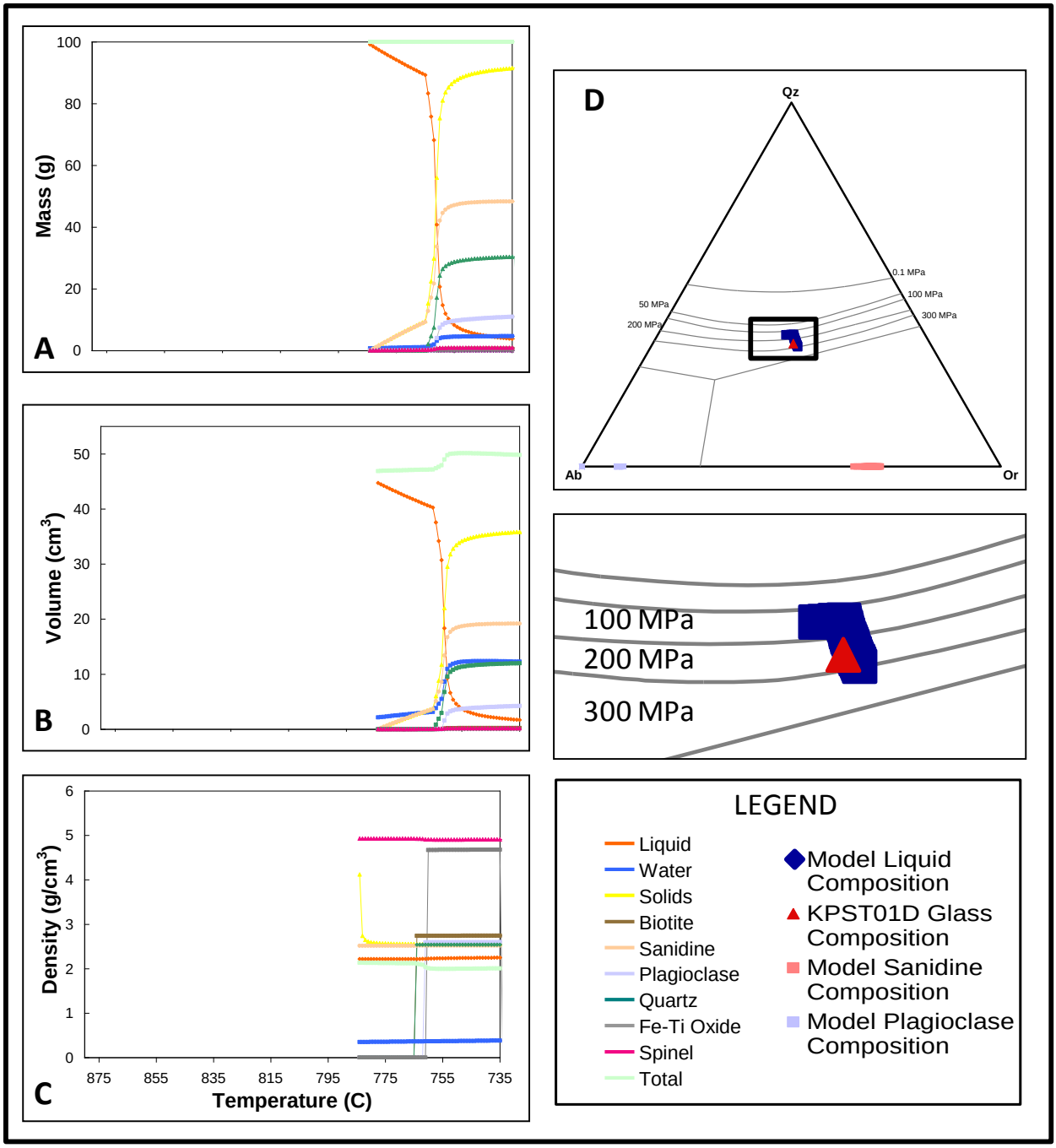

Data from one simulation run with equilibrium crystallization, composition KPST01D, 150 MPa and 5 wt. % water: (A) mass, (B) volume (C) density, (D) evolution of melt compositions on the Qz-Ab-Or ternary (using the Blundy and Cashman, 2001 projection scheme) with cotectic pressures in the zoomed-in box placed below the cotectic curve to which they correspond.

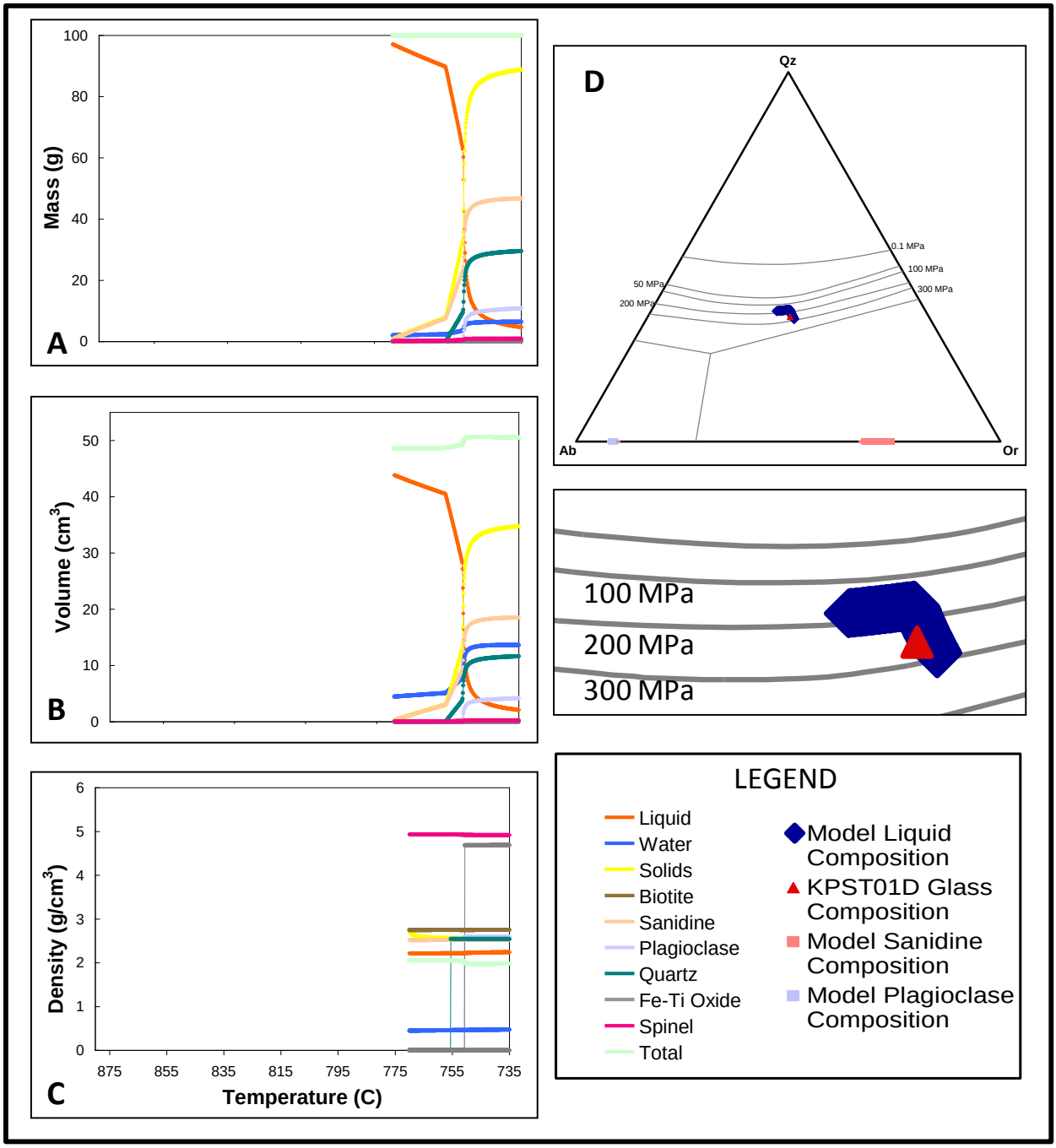

Data from one simulation run with equilibrium crystallization, composition KPST01D, 150 MPa and 5 wt. % water: (A) mass, (B) volume (C) density, (D) evolution of melt compositions on the Qz-Ab-Or ternary (using the Blundy and Cashman, 2001 projection scheme) with cotectic pressures in the zoomed-in box placed below the cotectic curve to which they correspond.

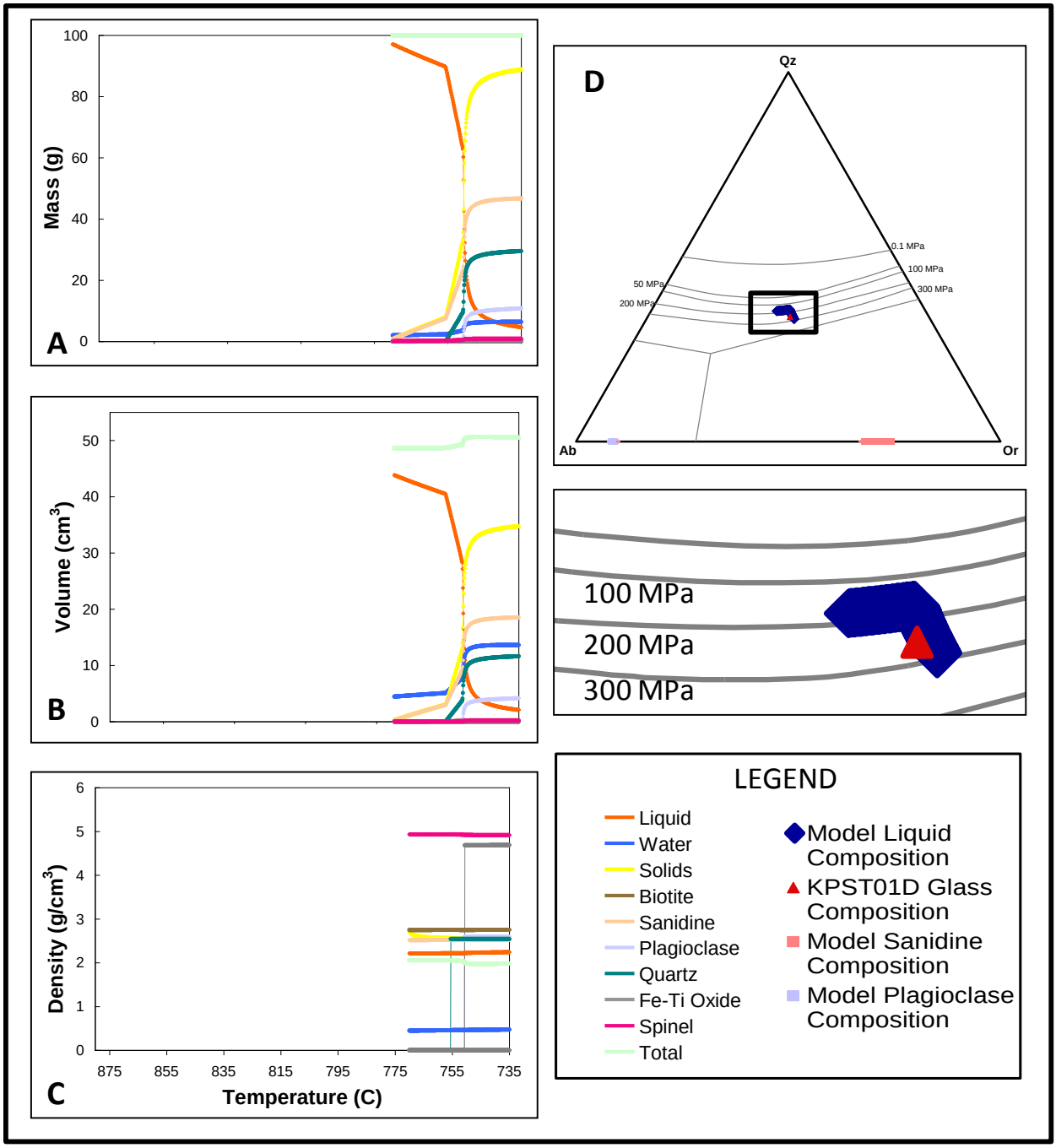

Data from one simulation run with equilibrium crystallization, composition KPST01D, 150 MPa and 7 wt. % water: (A) mass, (B) volume (C) density, (D) evolution of melt compositions on the Qz-Ab-Or ternary (using the Blundy and Cashman, 2001 projection scheme) with cotectic pressures in the zoomed-in box placed below the cotectic curve to which they correspond.

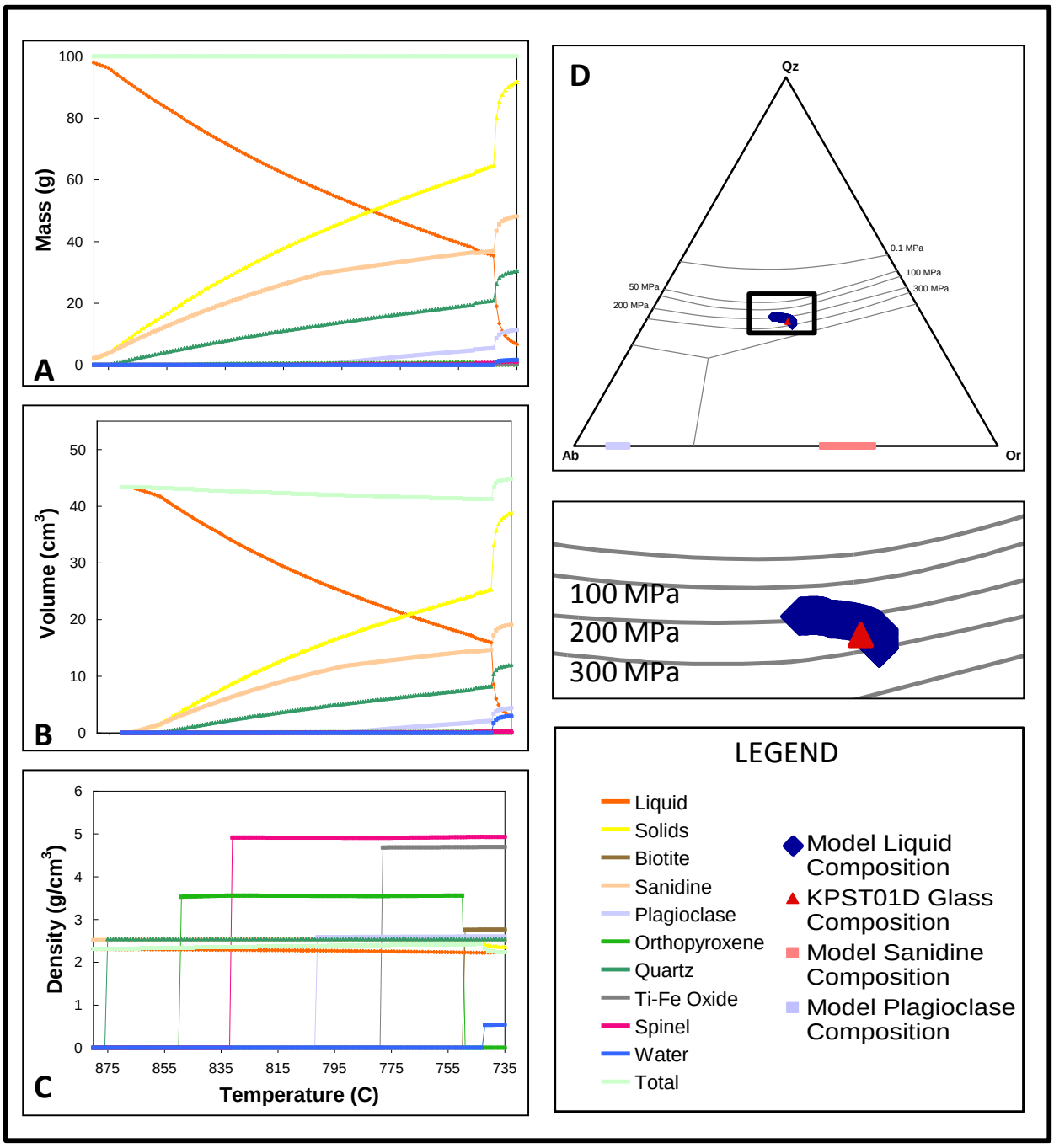

Data from one simulation run with equilibrium crystallization, composition KPST01D, 200 MPa and 2 wt. % water: (A) mass, (B) volume (C) density, (D) evolution of melt compositions on the Qz-Ab-Or ternary (using the Blundy and Cashman, 2001 projection scheme) with cotectic pressures in the zoomed-in box placed below the cotectic curve to which they correspond.

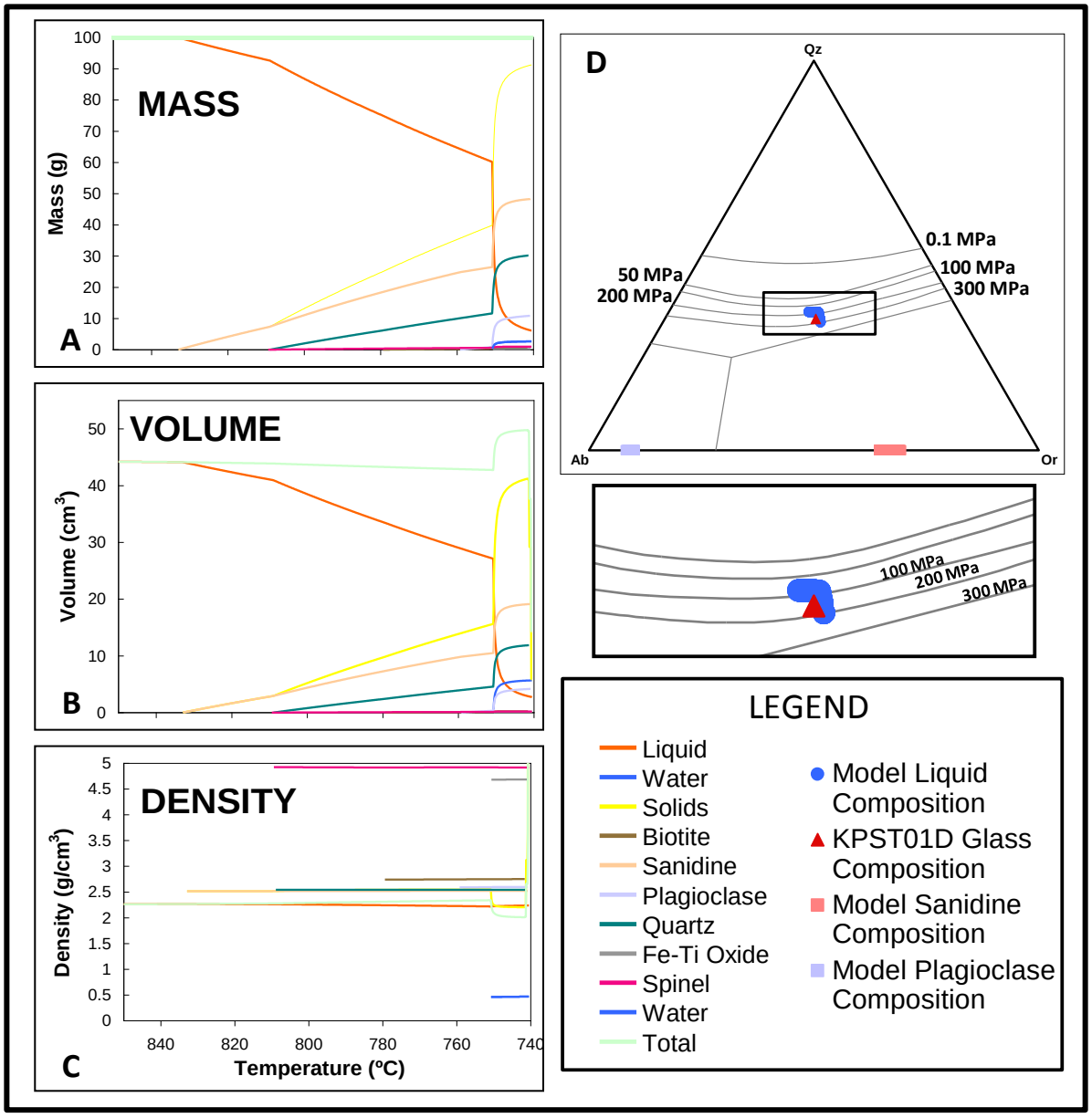

Data from one simulation run with equilibrium crystallization, composition KPST01D, 200 MPa and 3 wt. % water: (A) mass, (B) volume (C) density, (D) evolution of melt compositions on the Qz-Ab-Or ternary (using the Blundy and Cashman, 2001 projection scheme) with cotectic pressures in the zoomed-in box placed below the cotectic curve to which they correspond. This figure is also shown in the Results section of this study.

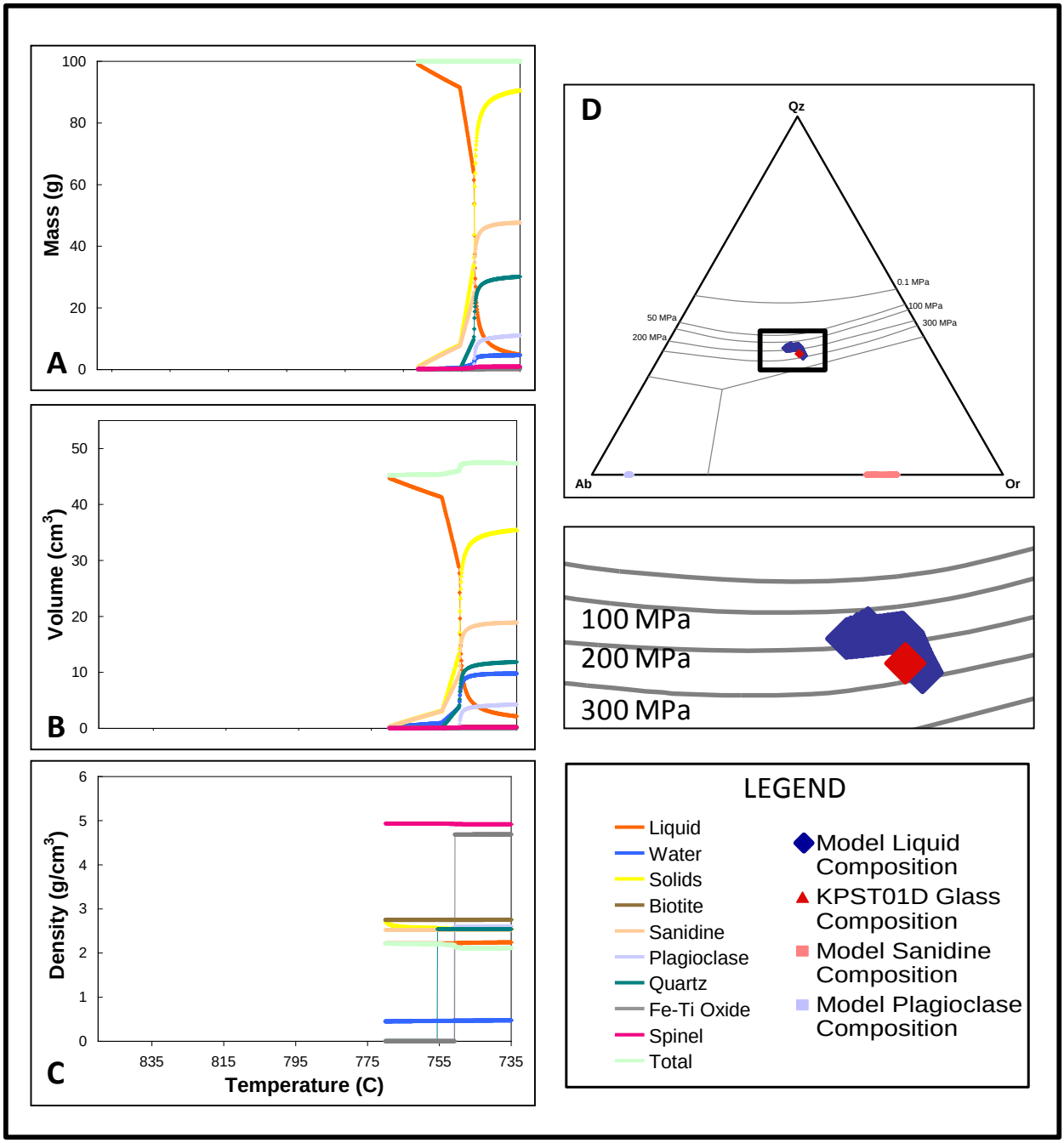

Data from one simulation run with equilibrium crystallization, composition KPST01D, 200 MPa and 5 wt. % water: (A) mass, (B) volume (C) density, (D) evolution of melt compositions on the Qz-Ab-Or ternary (using the Blundy and Cashman, 2001 projection scheme) with cotectic pressures in the zoomed-in box placed below the cotectic curve to which they correspond.

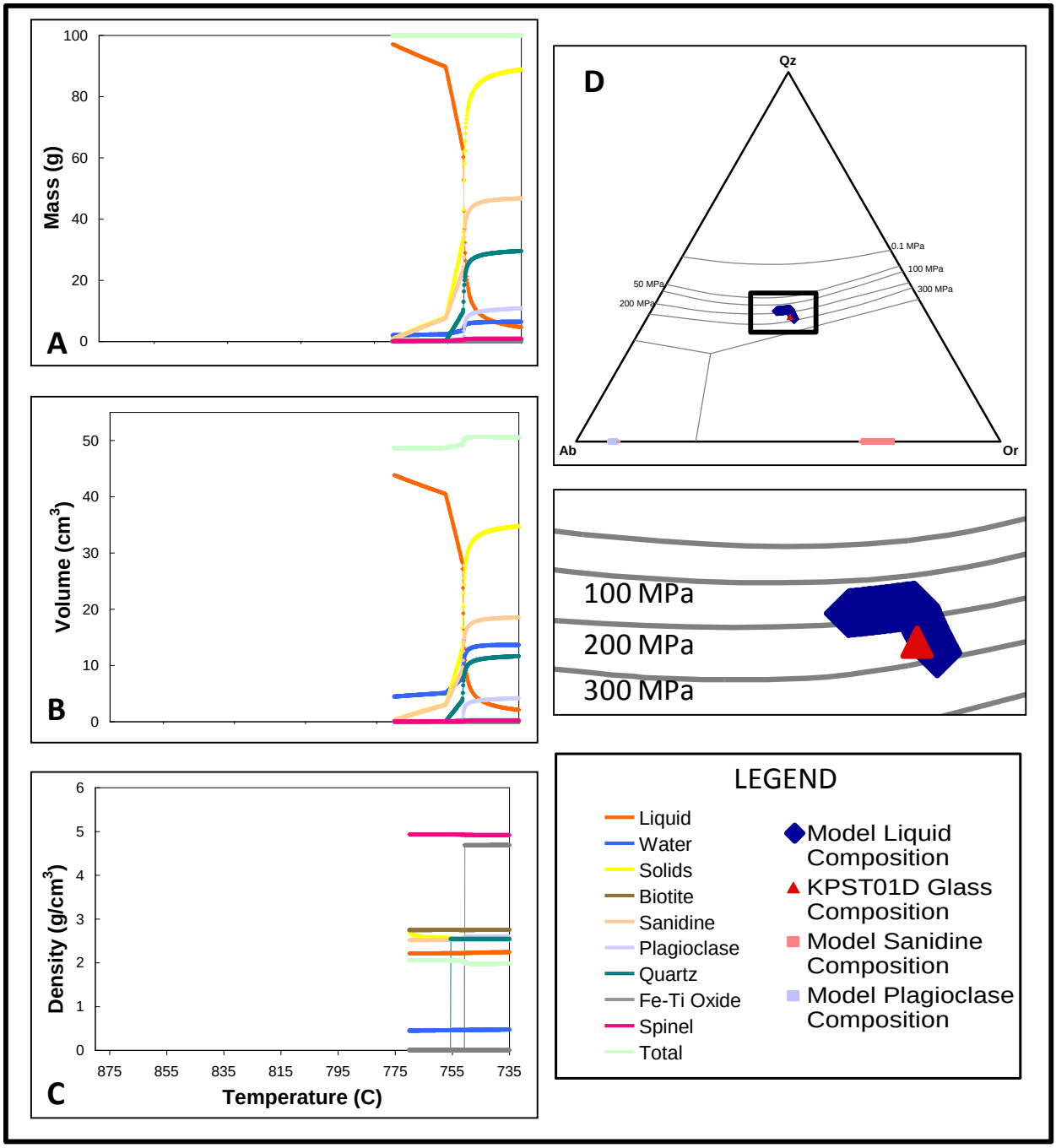

Data from one simulation run with equilibrium crystallization, composition KPST01D, 200 MPa and 7 wt. % water: (A) mass, (B) volume (C) density, (D) evolution of melt compositions on the Qz-Ab-Or ternary (using the Blundy and Cashman, 2001 projection scheme) with cotectic pressures in the zoomed-in box placed below the cotectic curve to which they correspond.

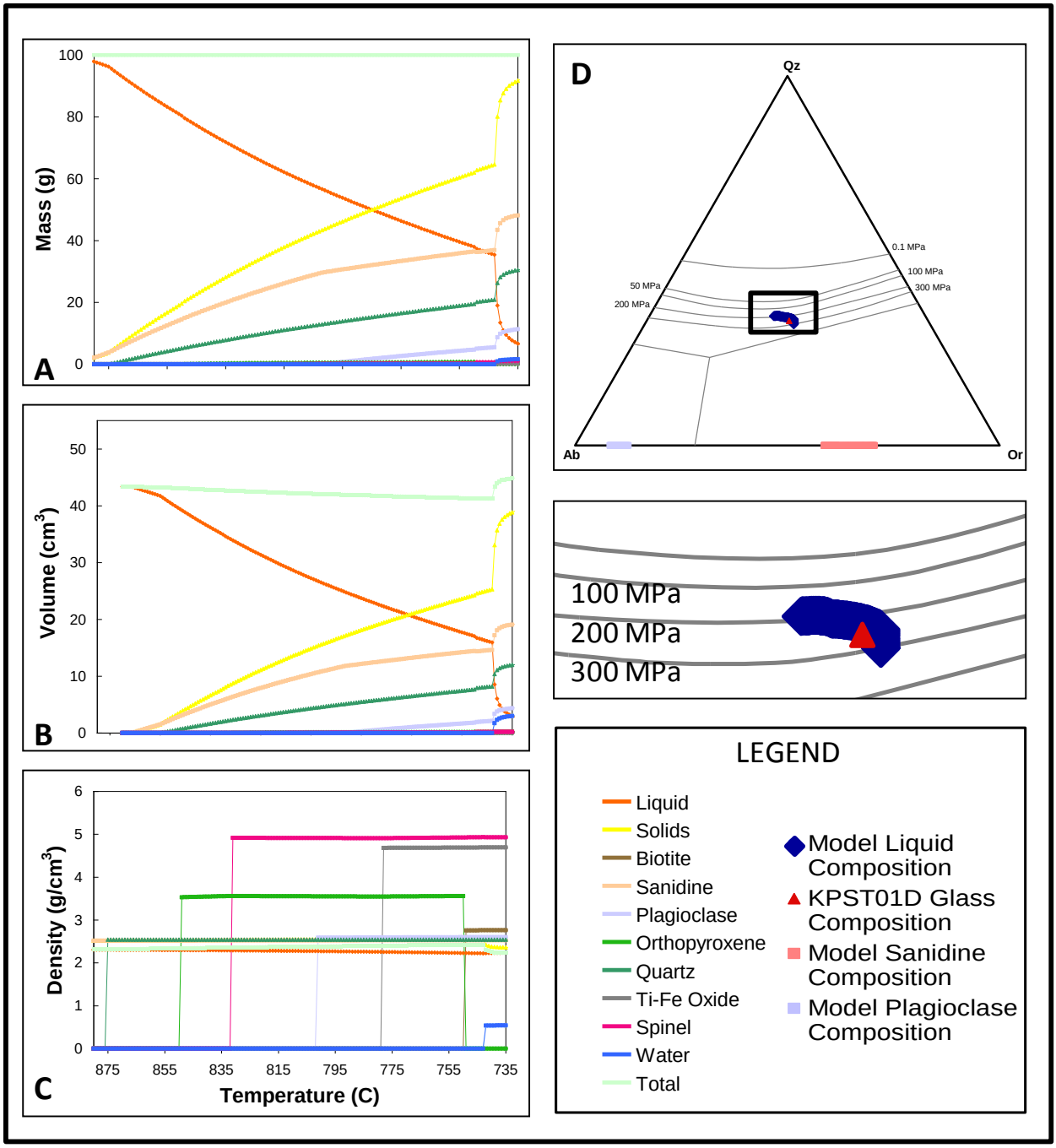

Data from one simulation run with equilibrium crystallization, composition KPST01D, 250 MPa and 2 wt. % water: (A) mass, (B) volume (C) density, (D) evolution of melt compositions on the Qz-Ab-Or ternary (using the Blundy and Cashman, 2001 projection scheme) with cotectic pressures in the zoomed-in box placed below the cotectic curve to which they correspond.

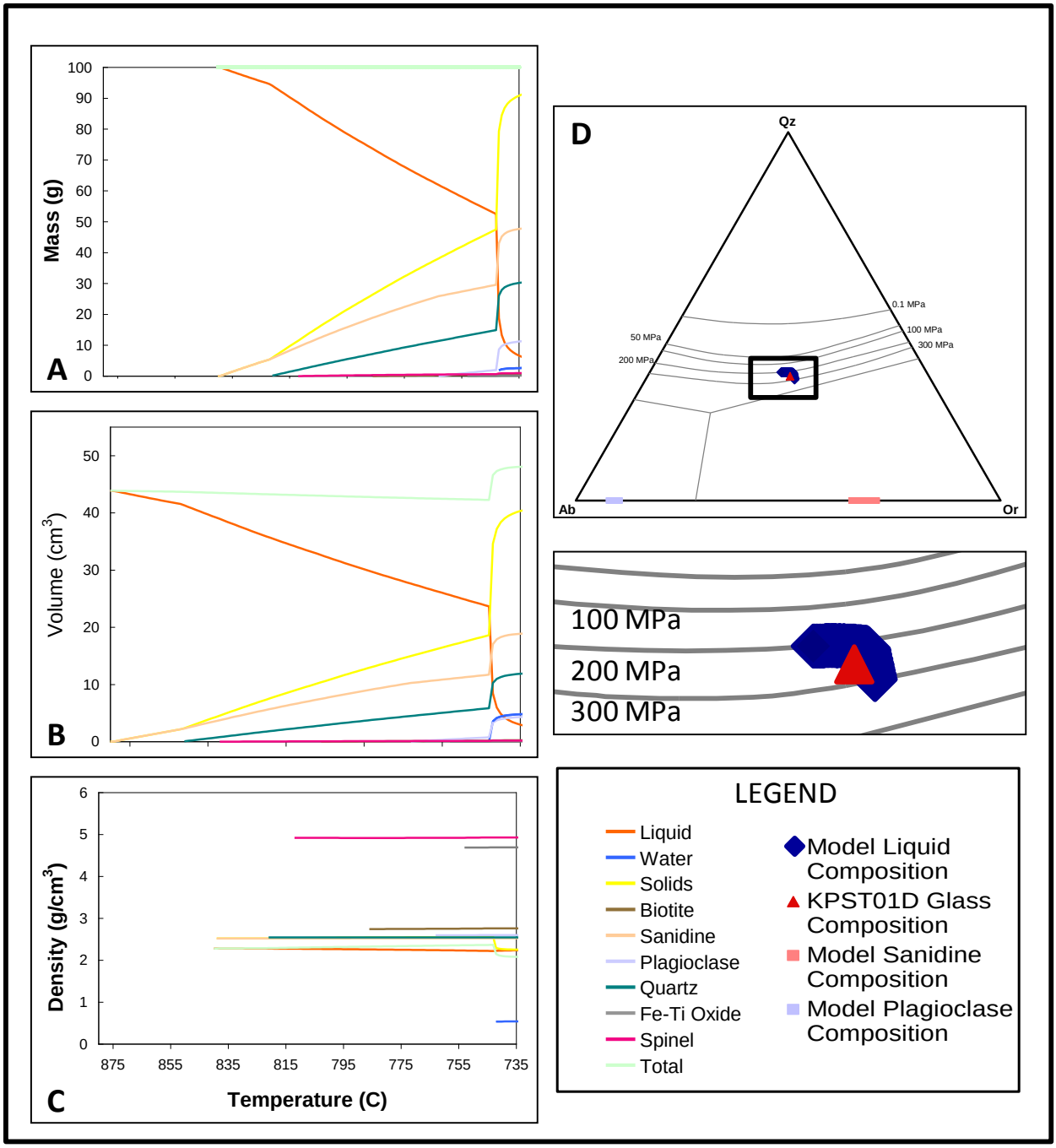

Data from one simulation run with equilibrium crystallization, composition KPST01D, 250 MPa and 3 wt. % water: (A) mass, (B) volume (C) density, (D) evolution of melt compositions on the Qz-Ab-Or ternary (using the Blundy and Cashman, 2001 projection scheme) with cotectic pressures in the zoomed-in box placed below the cotectic curve to which they correspond.

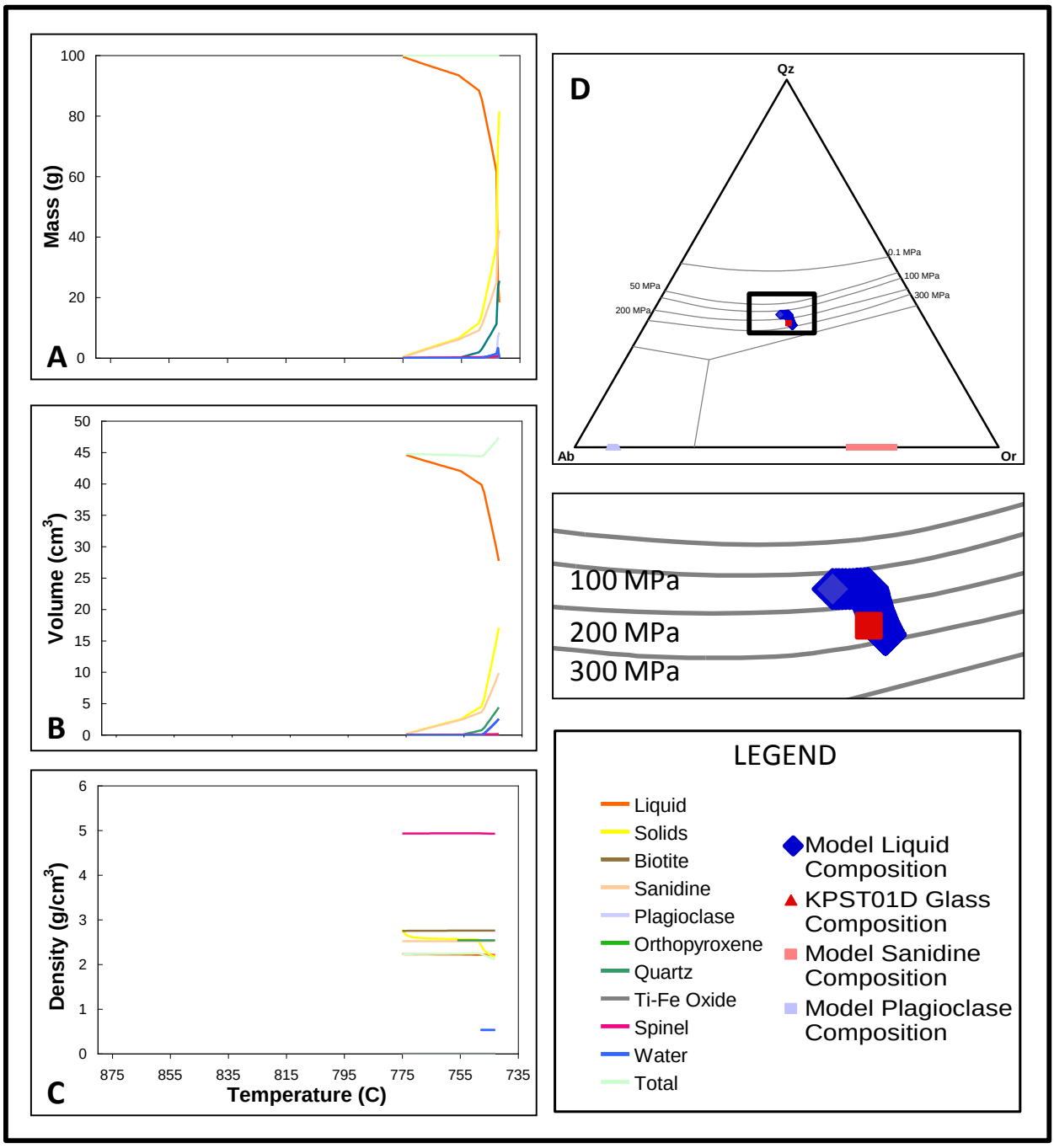

Data from one simulation run with equilibrium crystallization, composition KPST01D, 250 MPa and 5 wt. % water: (A) mass, (B) volume (C) density, (D) evolution of melt compositions on the Qz-Ab-Or ternary (using the Blundy and Cashman, 2001 projection scheme) with cotectic pressures in the zoomed-in box placed below the cotectic curve to which they correspond.

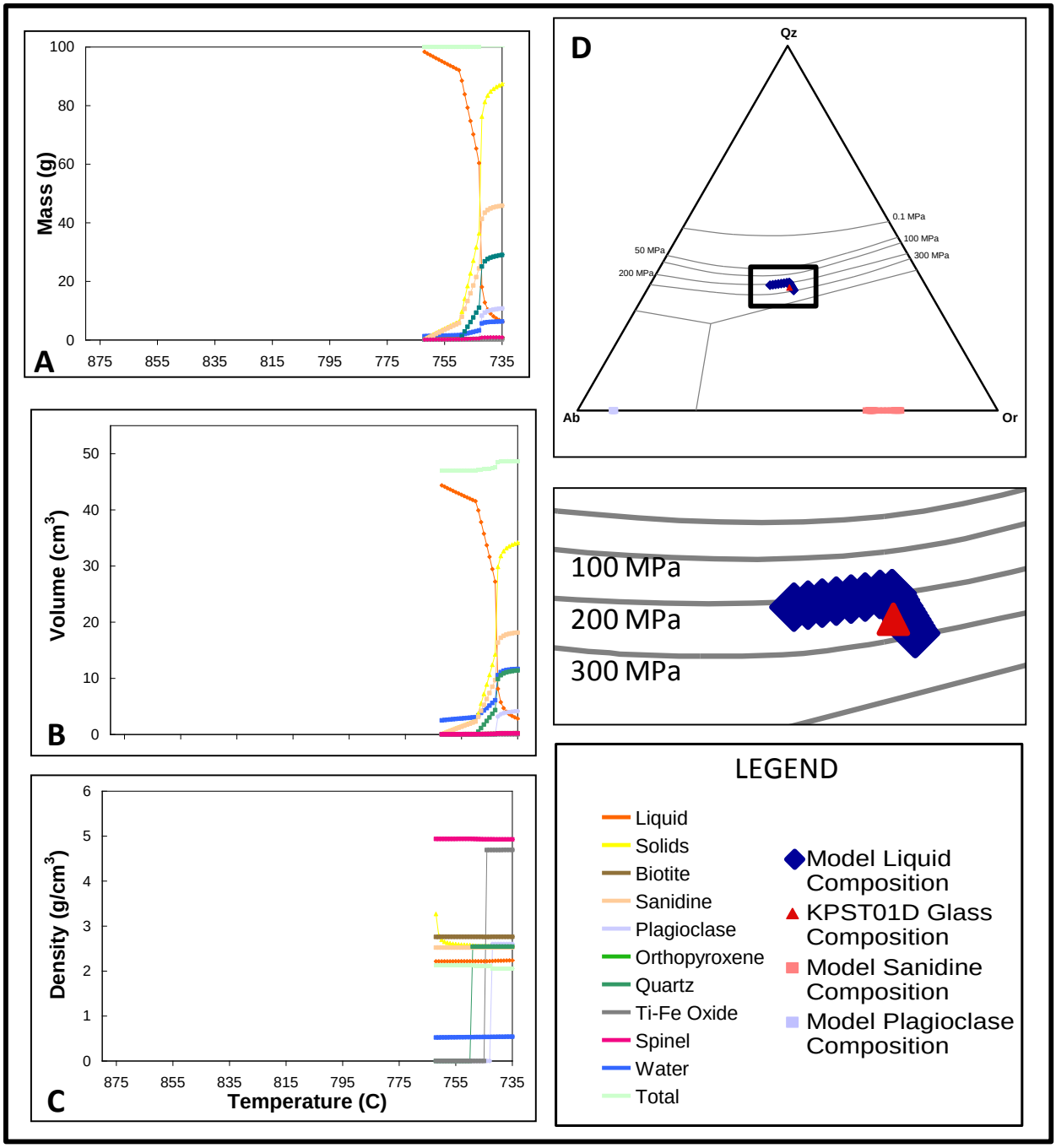

Data from one simulation run with equilibrium crystallization, composition KPST01D, 250 MPa and 7 wt. % water: (A) mass, (B) volume (C) density, (D) evolution of melt compositions on the Qz-Ab-Or ternary (using the Blundy and Cashman, 2001 projection scheme) with cotectic pressures in the zoomed-in box placed below the cotectic curve to which they correspond.

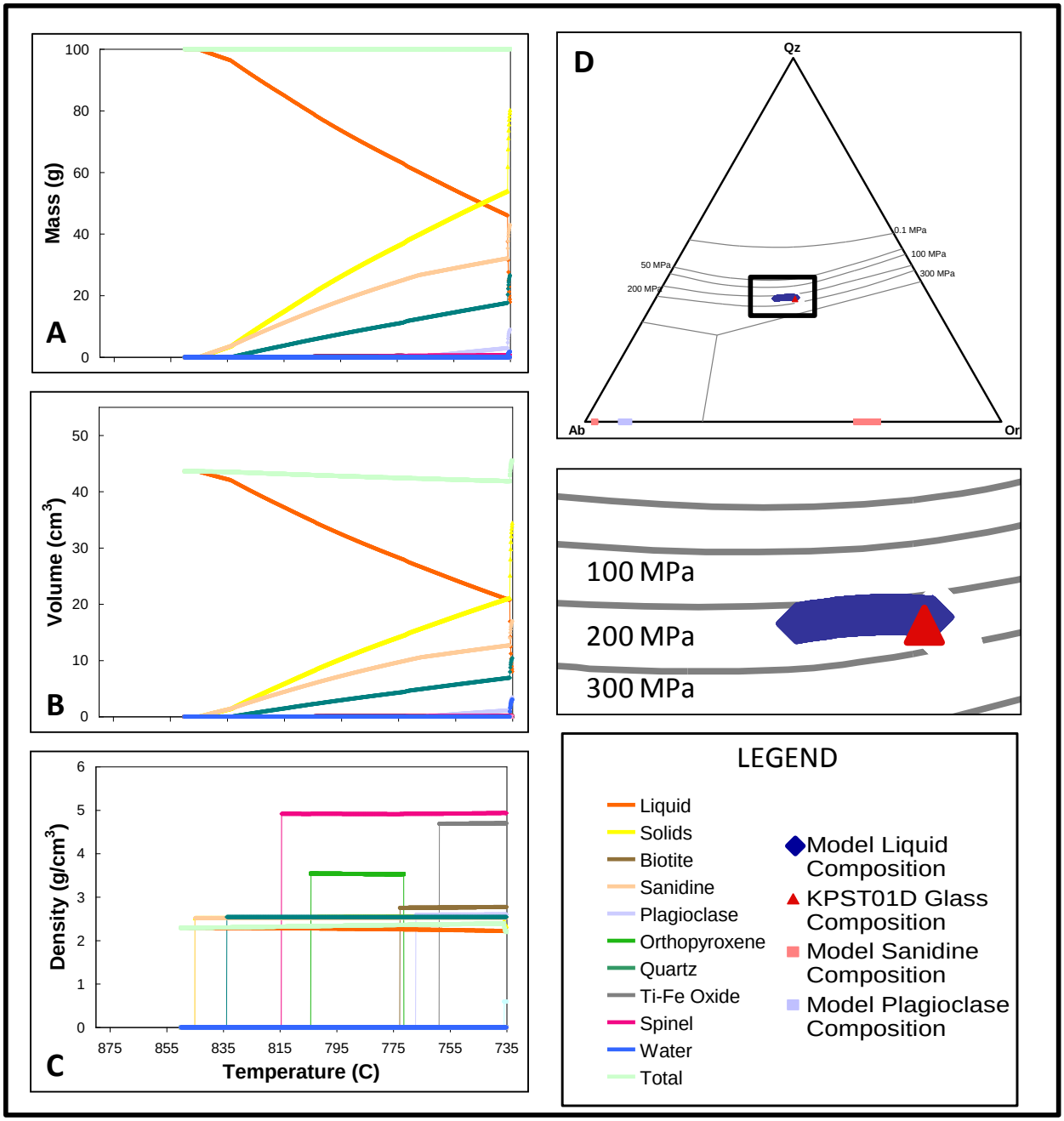

Data from one simulation run with equilibrium crystallization, composition KPST01D, 300 MPa and 3 wt. % water: (A) mass, (B) volume (C) density, (D) evolution of melt compositions on the Qz-Ab-Or ternary (using the Blundy and Cashman, 2001 projection scheme) with cotectic pressures in the zoomed-in box placed below the cotectic curve to which they correspond.

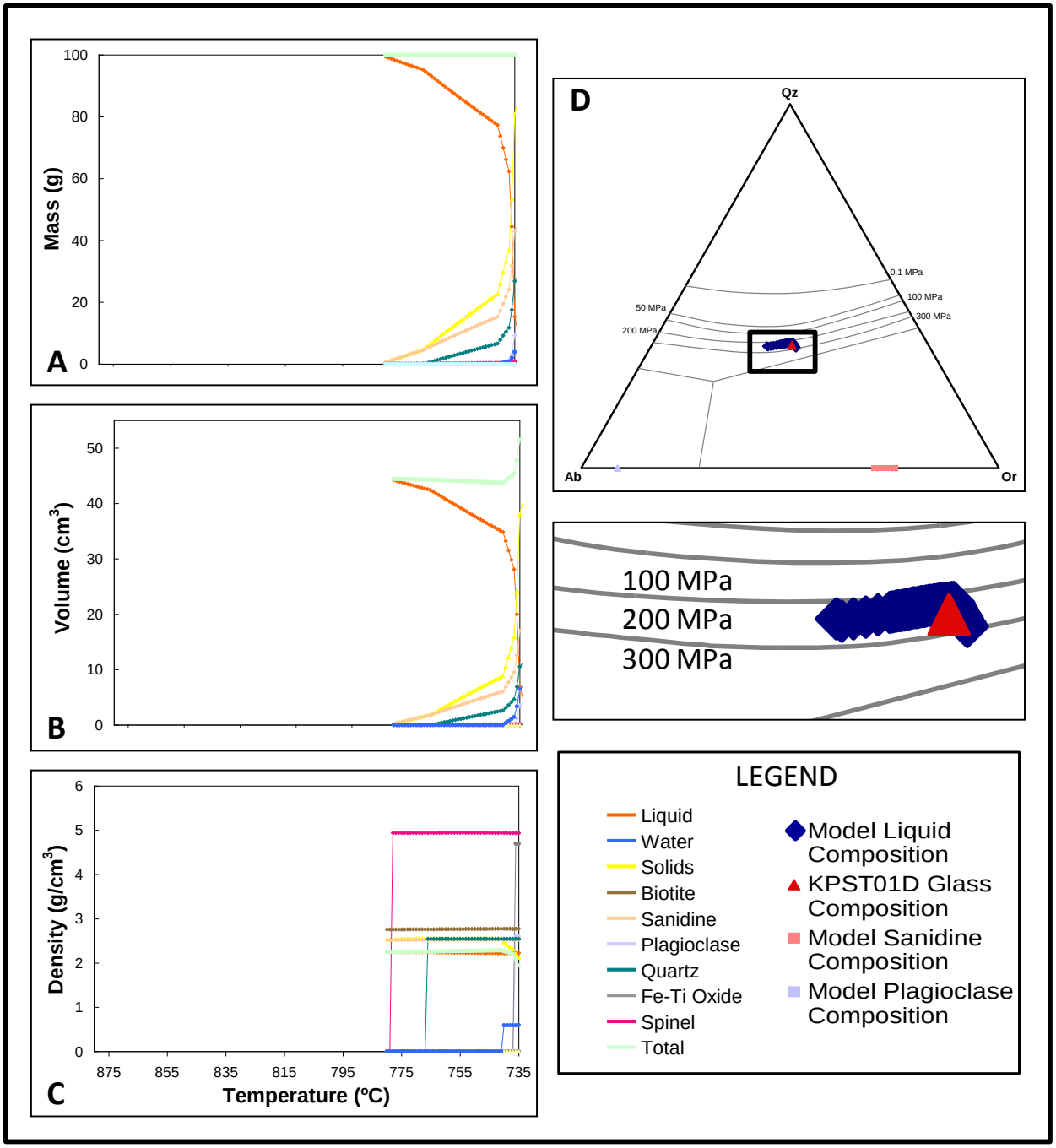

Data from one simulation run with equilibrium crystallization, composition KPST01D, 300 MPa and 5 wt. % water: (A) mass, (B) volume (C) density, (D) evolution of melt compositions on the Qz-Ab-Or ternary (using the Blundy and Cashman, 2001 projection scheme) with cotectic pressures in the zoomed-in box placed below the cotectic curve to which they correspond.

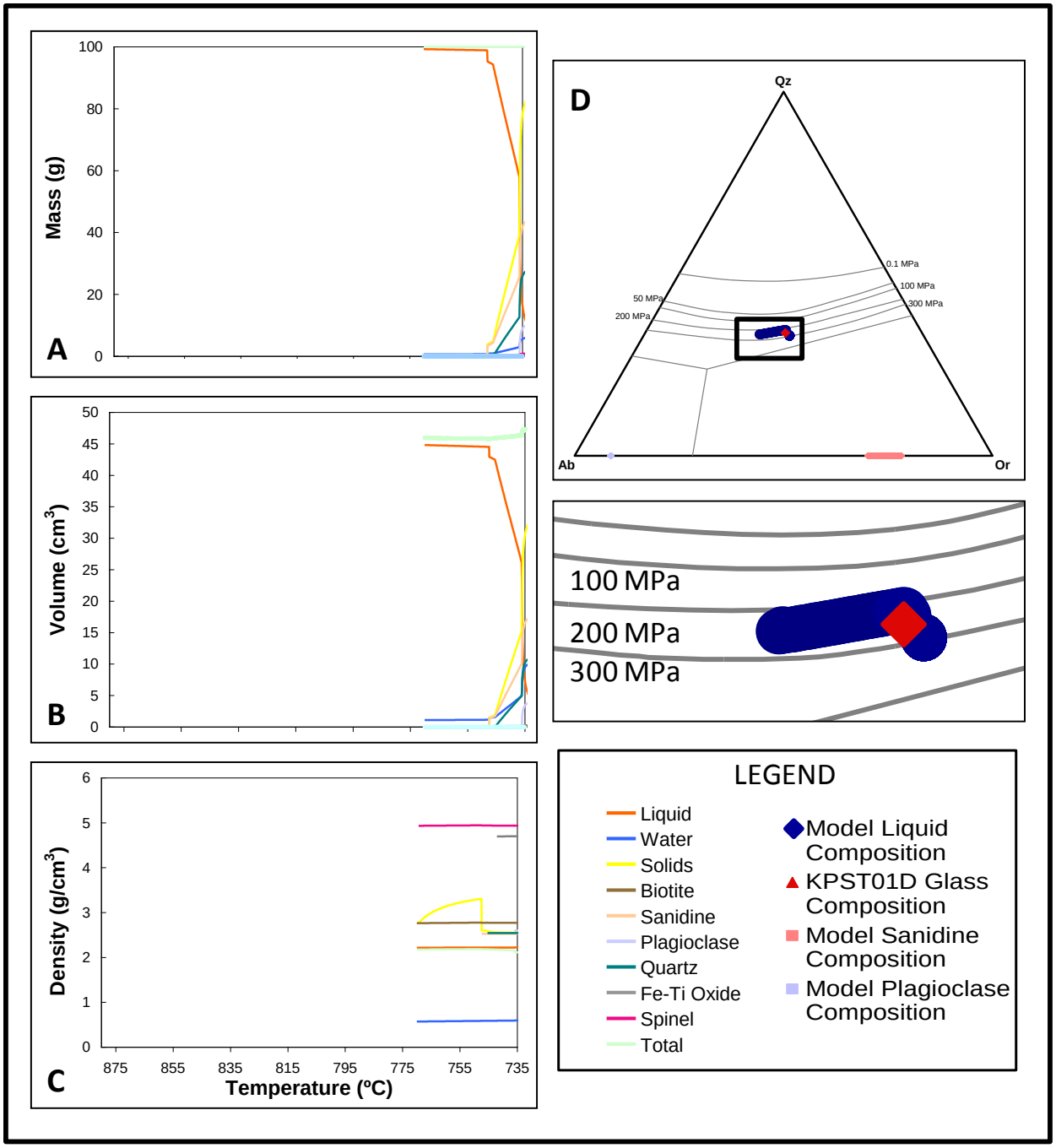

Data from one simulation run with equilibrium crystallization, composition KPST01D, 300 MPa and 7 wt. % water: (A) mass, (B) volume (C) density, (D) evolution of melt compositions on the Qz-Ab-Or ternary (using the Blundy and Cashman, 2001 projection scheme) with cotectic pressures in the zoomed-in box placed below the cotectic curve to which they correspond.

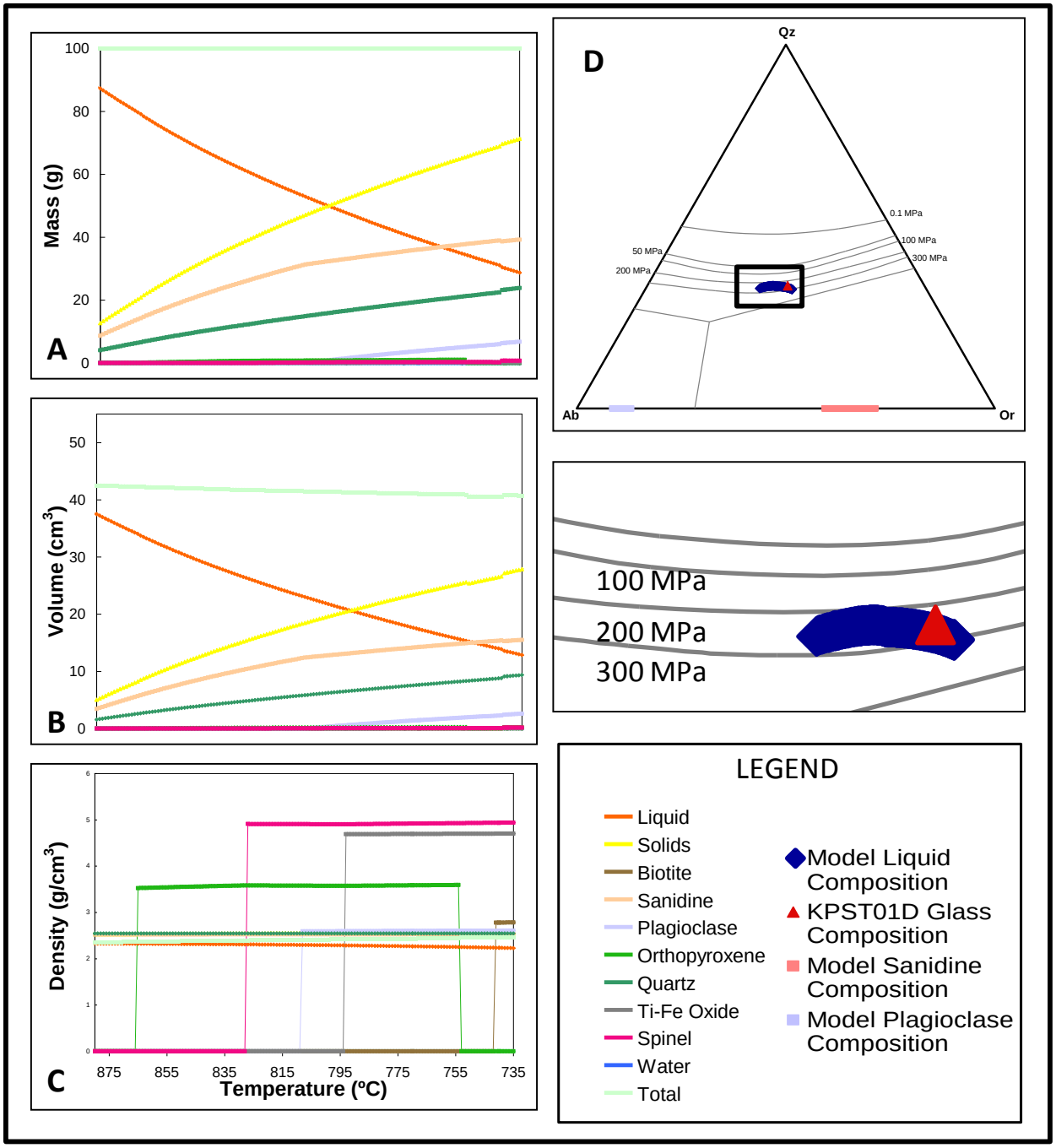

Data from one simulation run with equilibrium crystallization, composition KPST01D, 350 MPa and 2 wt. % water: (A) mass, (B) volume (C) density, (D) evolution of melt compositions on the Qz-Ab-Or ternary (using the Blundy and Cashman, 2001 projection scheme) with cotectic pressures in the zoomed-in box placed below the cotectic curve to which they correspond.

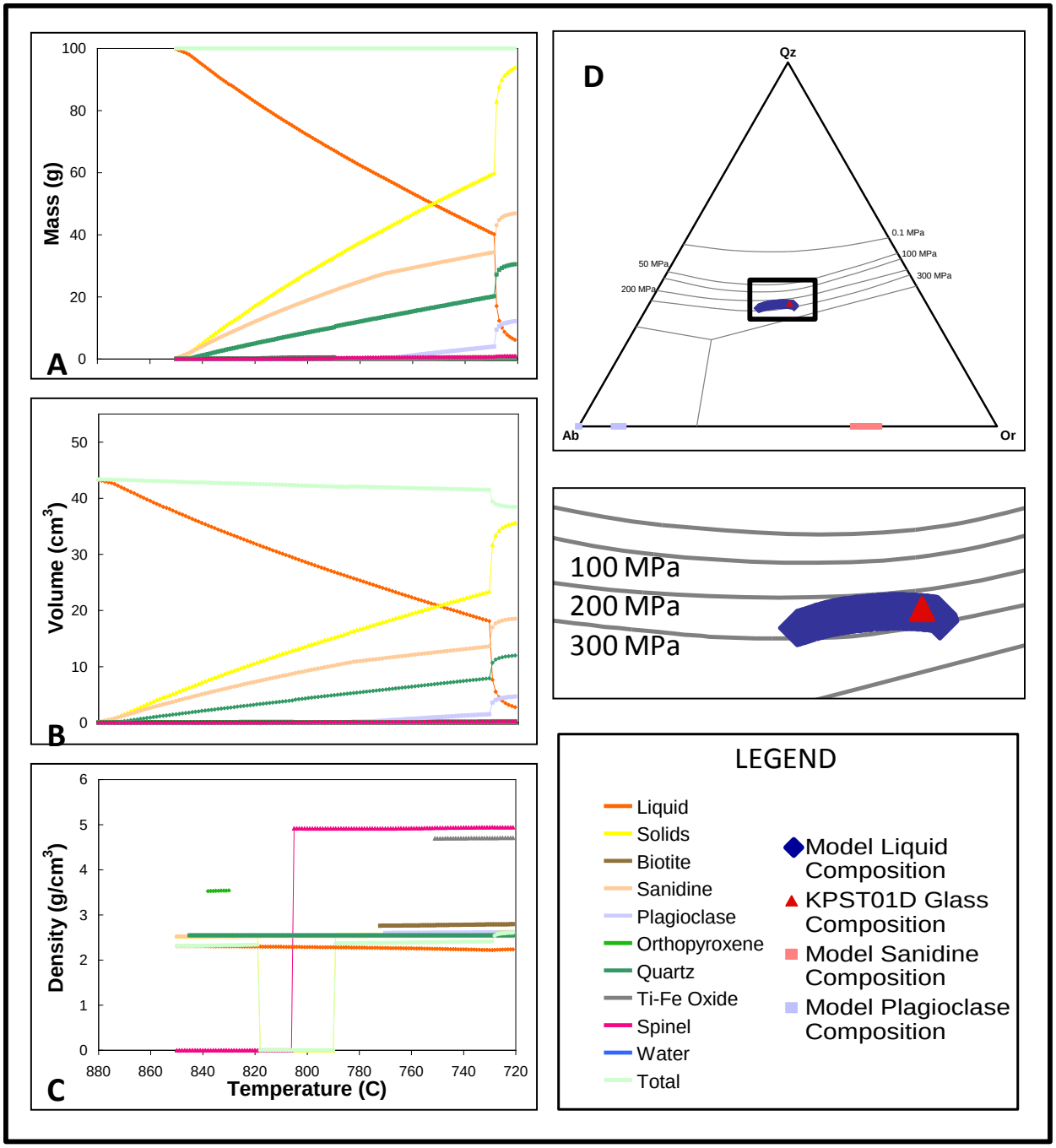

Data from one simulation run with equilibrium crystallization, composition KPST01D, 350 MPa and 3 wt. % water: (A) mass, (B) volume (C) density, (D) evolution of melt compositions on the Qz-Ab-Or ternary (using the Blundy and Cashman, 2001 projection scheme) with cotectic pressures in the zoomed-in box placed below the cotectic curve to which they correspond.

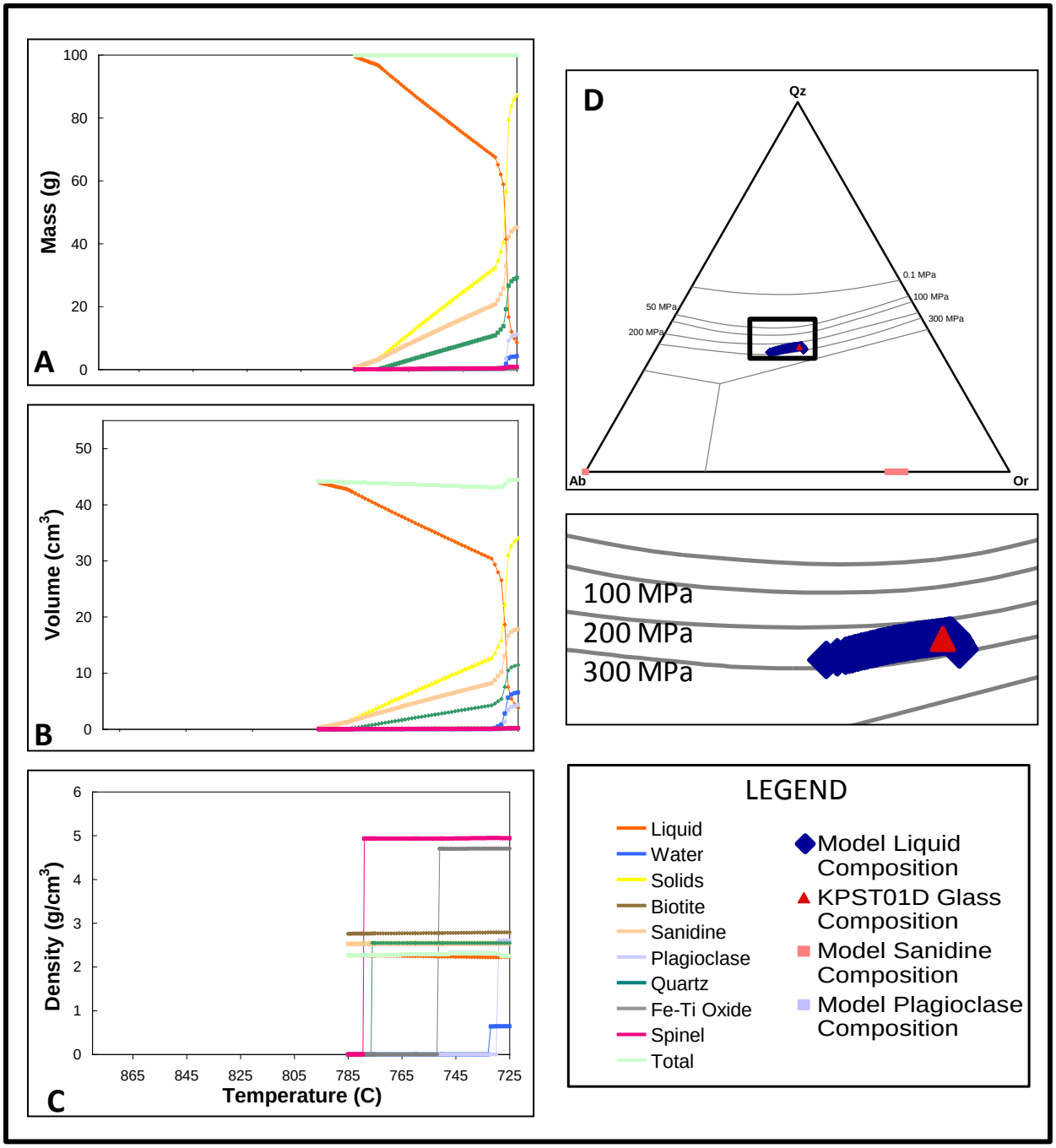

Data from one simulation run with equilibrium crystallization, composition KPST01D, 350 MPa and 5 wt. % water: (A) mass, (B) volume (C) density, (D) evolution of melt compositions on the Qz-Ab-Or ternary (using the Blundy and Cashman, 2001 projection scheme) with cotectic pressures in the zoomed-in box placed below the cotectic curve to which they correspond.

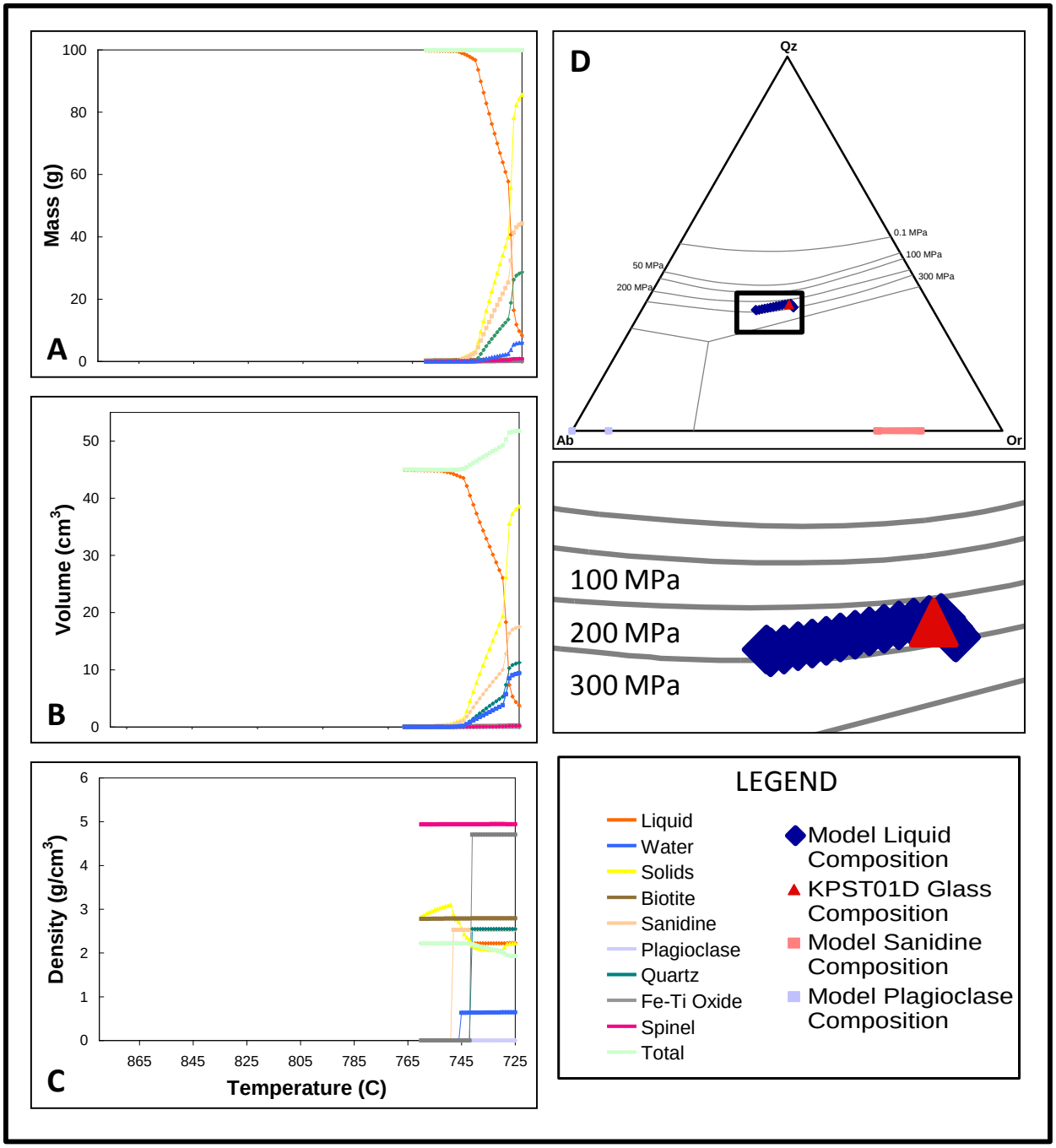

Data from one simulation run with equilibrium crystallization, composition KPST01D, 350 MPa and 7 wt. % water: (A) mass, (B) volume (C) density, (D) evolution of melt compositions on the Qz-Ab-Or ternary (using the Blundy and Cashman, 2001 projection scheme) with cotectic pressures in the zoomed-in box placed below the cotectic curve to which they correspond.

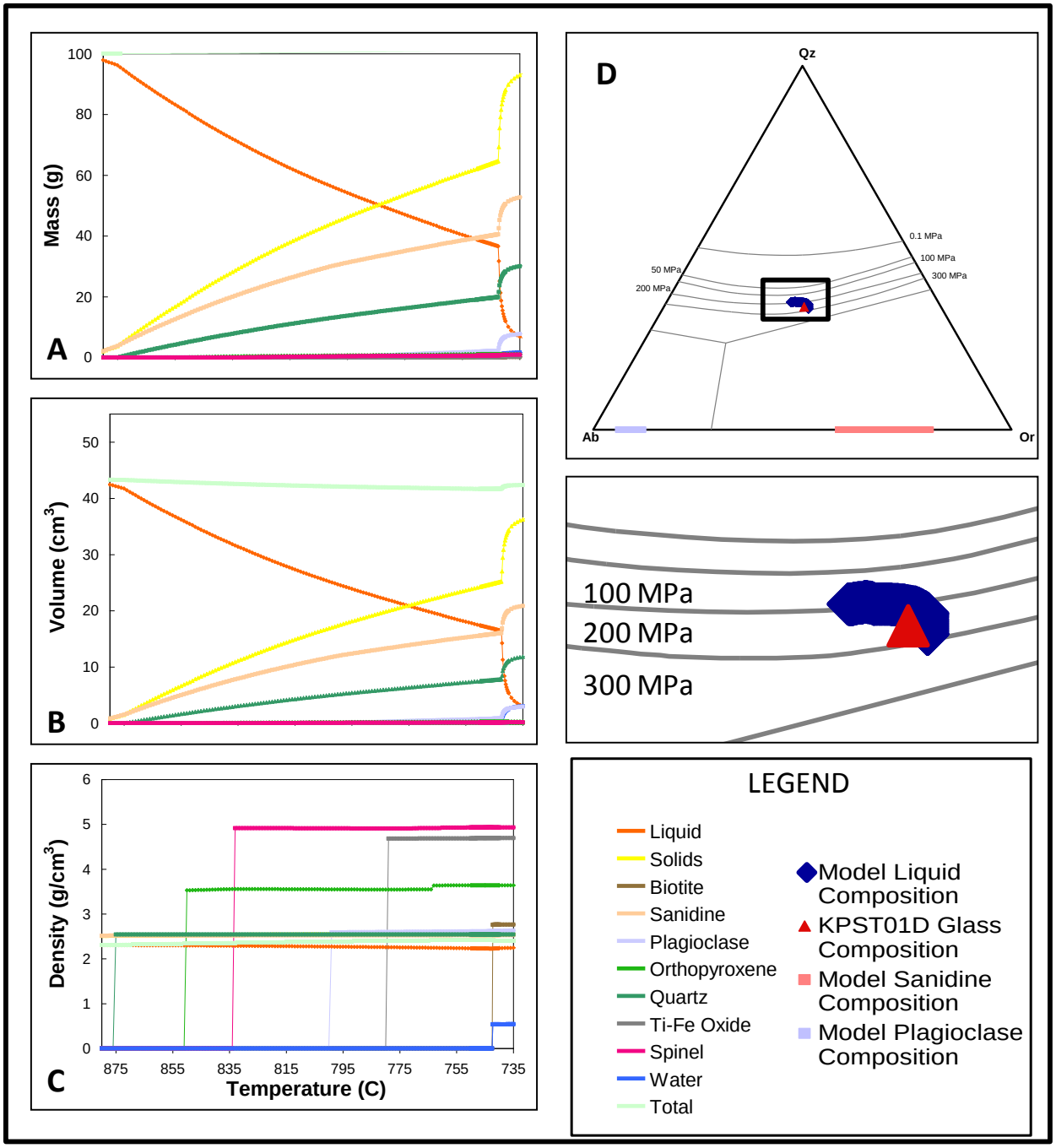

Data from one simulation run with fractional crystallization, composition KPST01D, 250 MPa and 2 wt. % water: (A) mass, (B) volume (C) density, (D) evolution of melt compositions on the Qz-Ab-Or ternary (using the Blundy and Cashman, 2001 projection scheme) with cotectic pressures in the zoomed-in box placed below the cotectic curve to which they correspond.

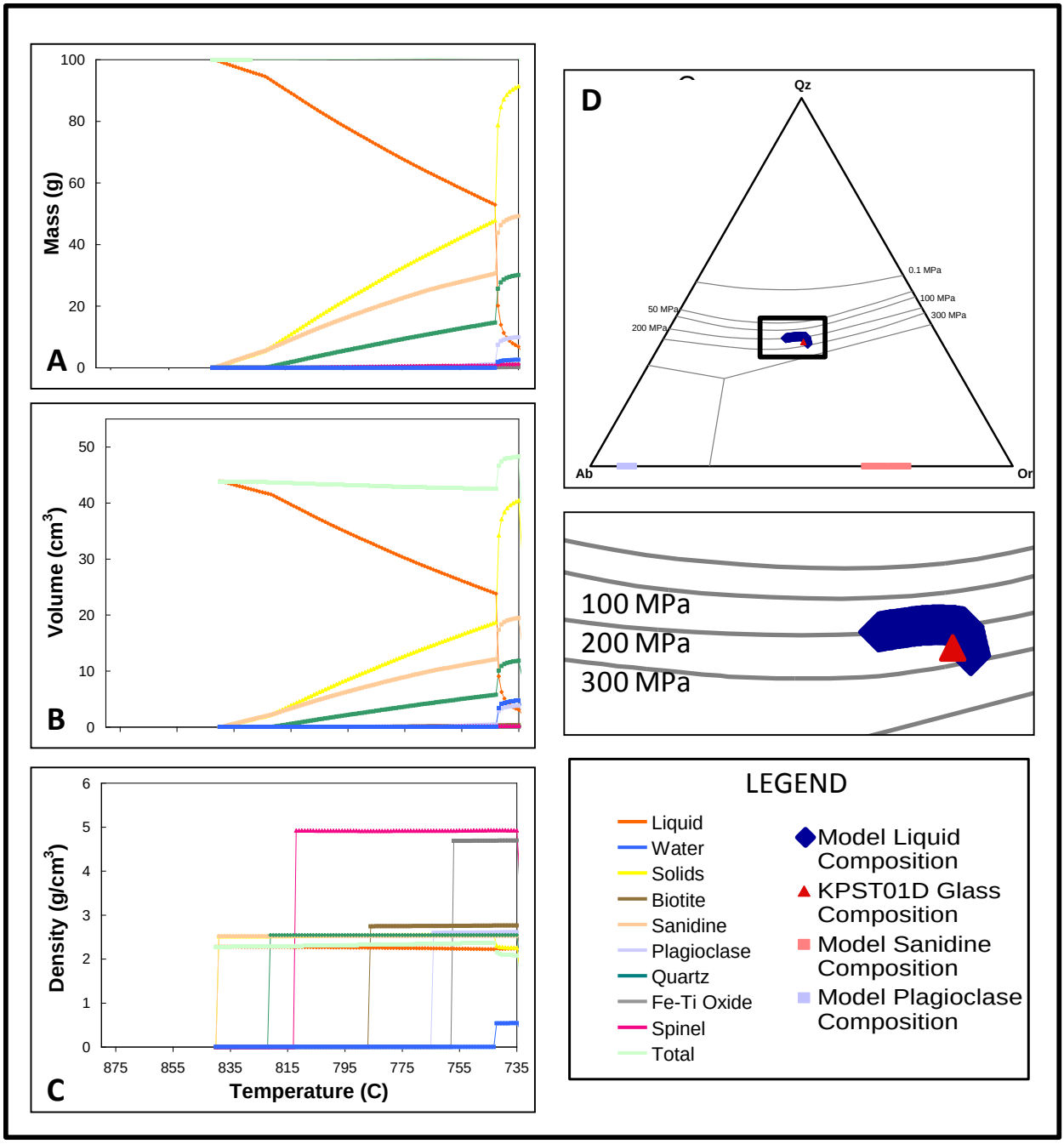

Data from one simulation run with fractional crystallization, composition KPST01D, 250 MPa and 3 wt. % water: (A) mass, (B) volume (C) density, (D) evolution of melt compositions on the Qz-Ab-Or ternary (using the Blundy and Cashman, 2001 projection scheme) with cotectic pressures in the zoomed-in box placed below the cotectic curve to which they correspond.

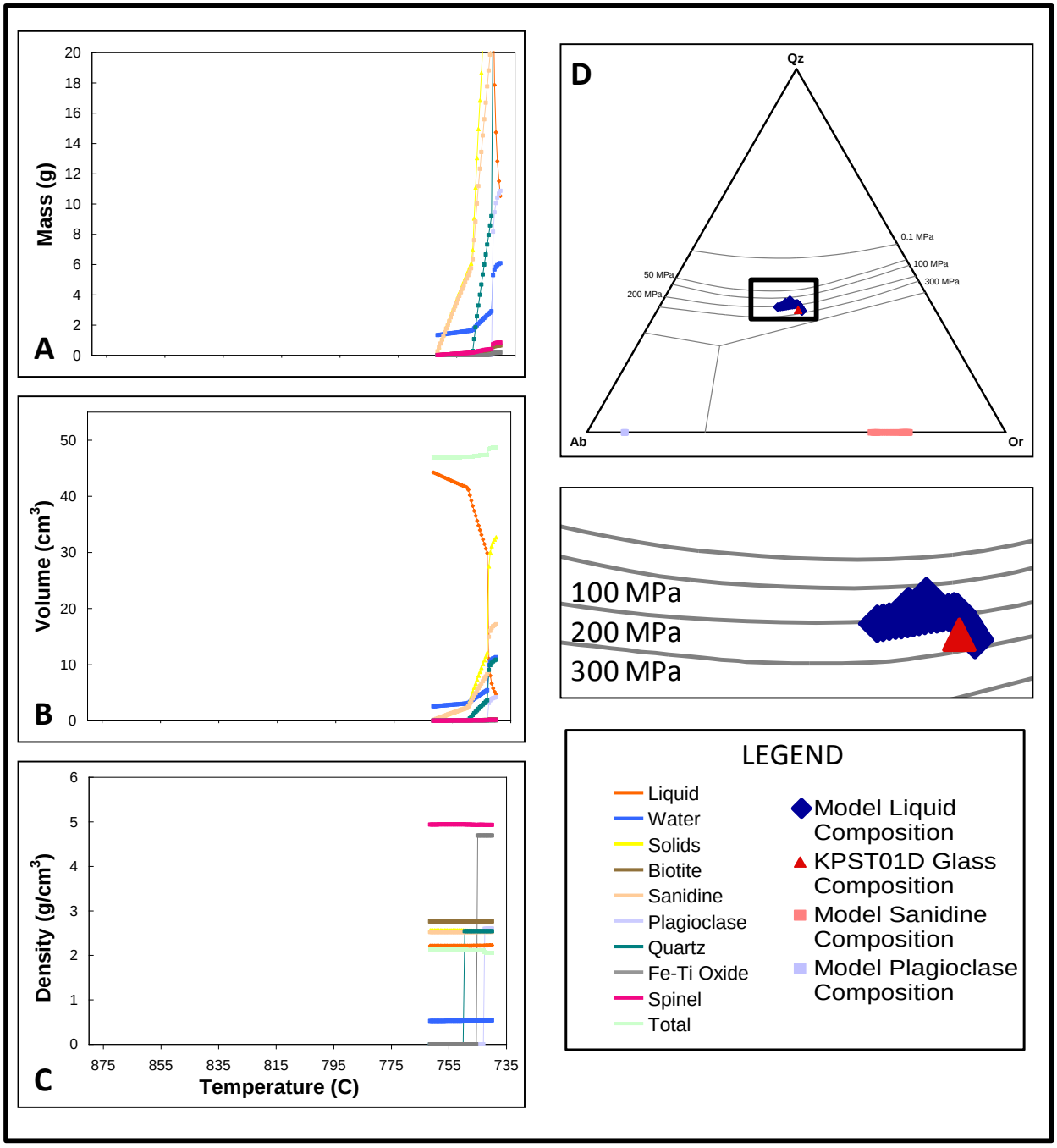

Data from one simulation run with fractional crystallization, composition KPST01D, 250 MPa and 7 wt. % water: (A) mass, (B) volume (C) density, (D) evolution of melt compositions on the Qz-Ab-Or ternary (using the Blundy and Cashman, 2001 projection scheme) with cotectic pressures in the zoomed-in box placed below the cotectic curve to which they correspond.

REFERENCES

Arnorsson, S., Ivarsson, G., Cuff, K. E., and Saemundsson, K., 1987. Geothermal activity in the Torfajokull Field, south Iceland; summary of geochemical studies. *Joekull* **37**, 1-12.

Bachmann, O. and Bergantz, G. W., 2004. On the origin of crystal-pore rhyolites; extracted from batholithic crystal mushes. *Journal of Petrology* **45**, 1565-1582.

Bachmann, O. and Bergantz, G. W., 2004. On the origin of crystal-pore rhyolites; extracted from batholithic crystal mushes. *Journal of Petrology* **45**, 1565-1582.

Bachmann, O. and Bergantz, G. W., 2008. Rhyolites and their Source Mushes across Tectonic Settings. *Journal of Petrology* **49**, 2277-2285.

Bachmann, O., Miller, C. F., and de Silva, S. L., 2007. The volcanic-plutonic connection as a stage for understanding crustal magmatism. *Journal of Volcanology and Geothermal Research* **167**, 1-23.

Bacon, C. R. and Lowenstern, J. B., 2005. Late Pleistocene granodiorite source for recycled zircon and phenocrysts in rhyodacite lava at Crater Lake, Oregon. *Earth and Planetary Science Letters* **233**, 277-293.

Bea, F., 1996. Residence of REE, Y, Th and U in granites and crustal protoliths; Implications for the chemistry of crustal melts. *Journal of Petrology* **37**, 521-552.

Belousova, E. A., Griffin, W. L., and O'Reilly, S. Y., 2006. Zircon crystal morphology, trace element signatures and Hf isotope composition as a tool for petrogenetic modelling: Examples from Eastern Australian granitoids. *Journal of Petrology* **47**, 329-353.

Bindeman, I. N. and Valley, J. W., 2003. Rapid generation of both high- and low-delta O-18, large-volume silicic magmas at the Timber Mountain/Oasis Valley caldera complex, Nevada. *Geological Society of America Bulletin* **115**, 581-595.

Blake, S., 1984. Magma mixing and hybridization processes at the alkalic, silicic, Torfajoekull central volcano triggered by tholeiitic Veidivoetn fissuring, South Iceland. *Journal of Volcanology and Geothermal Research* **22**, 1-31.

Blake, S., 1984. Volatile Oversaturation during the Evolution of Silicic Magma Chambers as an Eruption Trigger. *Journal of Geophysical Research* **89**, 8237-8244.

Blundy, J. and Cashman, K., 2001. Ascent-driven crystallisation of dacite magmas at Mount St. Helens, 1980-1986. *Contributions to Mineralogy and Petrology* **140**, 631-650.

Brown, K. L., Carter, C. A., Fohey, N. K., Wooden, J. L., Yi, K., Barth, A. P., and Anonymous, 2004. A study of the origin of rhyolite at mid-ocean ridges; geochronology and petrology of trachydacite and rhyolite from Salton Sea, California, and Torfajokull, Iceland. *Abstracts with Programs - Geological Society of America* **36**, 79.

Brown, S. J. A. and Fletcher, I. R., 1999. SHRIMP U-Pb dating of the preeruption growth history of zircons from the 340 ka Whakamaru Ignimbrite, New Zealand: Evidence for >250 k.y. magma residence times. *Geology* **27**, 1035-1038.

Buesch, D. C., 1992. Incorporation and Redistribution of Locally Derived Lithic Fragments within a Pyroclastic Flow. *Geological Society of America Bulletin* **104**, 1193-1207.

Buesch, D. C., Valentine, G. A., and Anonymous, 1986. *Peach Springs Tuff and volcanic stratigraphy of the southern Cerbat Mountains, Kingman, Arizona*. Geol. Soc. Am., Boulder, CO.

Carmichael, I. S. E., 1964. The petrology of Thingmuli, a Tertiary volcano in eastern Iceland. *Journal of Petrology* **5**, 435-460.

Carmichael, I. S. E., Turner, F. J., and Verhoogen, J., 1974. McGraw-Hill Book Co., New York.

Charlier, B. L. A., Wilson, C. J. N., Lowenstern, J. B., Blake, S., Van Calsteren, P. W., and Davidson, J. P., 2005. Magma generation at a large, hyperactive silicic volcano (Taupo, New Zealand) revealed by U-Th and U-Pb systematics in zircons. *Journal of Petrology* **46**, 3-32.

Claiborne, L. L., Miller, C. F., Walker, B. A., Wooden, J. L., Mazdab, F. K., and Bea, F., 2006. Tracking magmatic processes through Zr/Hf ratios in rocks and Hf and Ti zoning in zircons: An example from the Spirit Mountain batholith, Nevada. *Mineralogical Magazine* **70**, 517-543.

Claiborne, L.L., Miller, C.F. and Wooden, J.L., 2010a, Trace element composition of igneous zircon; a thermal and compositional record of the accumulation and evolution of a large silicic batholiths, Spirit Mountain, Nevada, *Contributions to Mineralogy and Petrology*.

Claiborne, L.L., Miller, C.F., Flanagan, D.M., Clynne, M.A. and Wooden, J.L., 2010b, Zircon reveals protracted magma storage and recycling beneath Mount St. Helens, *Geology*, G31285.

Condomines, M., Groenvold, K., Hooker, P. J., Muehlenbachs, K., O'Nions, R. K., Oskarsson, N., and Oxburgh, E. R., 1983. Helium, oxygen, strontium and neodymium isotopic relationships in Icelandic volcanics. *Earth and Planetary Science Letters* **66**, 125-136.

Condomines, M., Morand, P., Allegre, C. J., and Sigvaldason, G., 1981. Th-230-U-238 Disequilibria in Historical Lavas from Iceland. *Earth and Planetary Science Letters* **55**, 393-406.

Corfu, F., Hanchar, J. M., Hoskin, P. W. O., and Kinny, P., 2003. Atlas of Zircon Textures. *Reviews in Mineralogy and Geochemistry* **53**, 469-500.

DeWitt, E., Thorson, J. P., and Smith, R. C., 1986, Geology and Gold Deposits of the Oatman district, northwestern Arizona: USGS Bulletin 1857, p. I1-I27

Faulds, J. E., Feuerbach, D. L., Miller, C. F., and Smith, E. I., 2001. Cenozoic evolution of the northern Colorado River extensional corridor, southern Nevada and Northwest Arizona. *Guidebook - Pacific Section, American Association of Petroleum Geologists* **78**, 239-271.

Ferguson, C.A., 2008, Silver Creek Caldera, probable source of the Miocene Peach Spring Tuff, Oatman Mining District, Arizona. *Abstracts with Programs – Geological Society of America*, **40**(1), 33.

Ferry, J. M. and Watson, E. B., 2007. New thermodynamic models and revised calibrations for the Ti-in-zircon and Zr-in-rutile thermometers. *Contributions to Mineralogy and Petrology* **154**, 429-437.

Fowler, S. J. and Spera, F. J., 2008. Phase equilibria trigger for explosive volcanic eruptions. *Geophysical Research Letters* **35**, -.

Fu, B., Page, F. Z., Cavosie, A. J., Fournelle, J., Kita, N. T., Lackey, J. S., Wilde, S. A., and Valley, J. W., 2008. Ti-in-zircon thermometry: applications and limitations. *Contributions to Mineralogy and Petrology* **156**, 197-215.

Furman, T., Meyer, P. S., and Frey, F., 1992. Evolution of Icelandic Central Volcanos - Evidence from the Austurhorn Intrusion, Southeastern Iceland. *Bulletin of Volcanology* **55**, 45-62.

Gaudio, S.,2003, *Discrimination and correlation of the Peach Springs Tuff and Peach Springs age-equivalent ignimbrites by geochronology, petrography, and incompatible element geochemistry from the northern Colorado River Extensional Corridor, Central Basin and Range Province, U.S.A.* [B.A. Thesis]: Wooster, Ohio. College of Wooster, 69 p.

Ghiorso, M. S. and Sack, R. O., 1995. Chemical Mass-Transfer in Magmatic Processes .4. A Revised and Internally Consistent Thermodynamic Model for the Interpolation and Extrapolation of Liquid-Solid Equilibria in Magmatic Systems at Elevated-Temperatures and Pressures. *Contributions to Mineralogy and Petrology* **119**, 197-212.

Glazner, A. F., Nielson, J. E., Howard, K. A., and Miller, D. M., 1986. Correlation of the Peach Springs Tuff, a Large-Volume Miocene Ignimbrite Sheet in California and Arizona. *Geology* **14**, 840-843.

Grimes, C. B., John, B. E., Kelermen, P. B., Mazdab, F. K., Wooden, J. L., Cheadle, M. J., Hanghoj, K., and Schwartz, J. J., 2007. Trace element chemistry of zircons from oceanic crust: A method for distinguishing detrital zircon provenance. *Geology* **35**, 643-646.

Gronvold, K., Larsen, G., Einarsson, P., Thorarinsson, S. and Saemundsson, K., 1983, The Hekla eruption 1980-1981, *Bulletin of Volcanology*, **46**(4), 349-363.

Gualda, G.A. and Ghiorso, M.S., 2009, Crystallization of the Bishop magma body (or magma bodies?): Lessons from thermodynamics. *Transactions of the American Geophysical Union, Fall Meeting, EOS,* V23C-2096.

Gunnarsson, B., Marsh, B. D., and Taylor, H. P., 1998. Generation of Icelandic rhyolites: silicic lavas from the Torfajokull central volcano. *Journal of Volcanology and Geothermal Research* **83**, 1-45.

Gusa, S., Nielson, J. E., and Howard, K. A., 1987. Heavy-Mineral Suites Confirm the Wide Extent of the Peach Springs Tuff in California and Arizona, USA. *Journal of Volcanology and Geothermal Research* **33**, 343-347.

Hanchar, J. M. and Miller, C. F., 1993. Zircon zonation patterns as revealed by cathodoluminescence and backscattered electron images; implications for interpretation of complex crustal histories. *Chemical Geology* **110**, 1-13.

Hanchar, J. M. and Watson, E. B., 2003. Zircon Saturation Thermometry. *Reviews in Mineralogy and Geochemistry* **53**, 89-112.

Harrison, T. M. and Watson, E. B., 1983. Kinetics of Zircon Dissolution and Zirconium Diffusion in Granitic Melts of Variable Water-Content. *Contributions to Mineralogy and Petrology* **84**, 66-72.

Harrison, T. M., Watson, E. B., and Aikman, A. B., 2007. Temperature spectra of zircon crystallization in plutonic rocks. *Geology* **35**, 635-638.

Hayden, L. A. and Watson, E. B., 2007. Rutile saturation in hydrous siliceous melts and its bearing on Ti-thermometry of quartz and zircon. *Earth and Planetary Science Letters* **258**, 561-568.

Hildreth, W. and Anonymous, 1981. Gradients in silicic magma chambers; implications for lithospheric magmatism. *Journal of Geophysical Research* **86**, 10153-10192.

Hildreth, W., 2004. Volcanological perspectives on Long Valley, Mammoth Mountain, and Mono Craters; several contiguous but discrete systems. *Journal of Volcanology and Geothermal Research* **136**, 169-198.

Hoskin, P. W. O. and Schaltegger, U., 2003. The Composition of Zircon and Igneous and Metamorphic Petrogenesis. *Reviews in Mineralogy and Geochemistry* **53**, 27-62.

Johannes, W. and Holtz, F., 1996. Petrogenesis and Experimental Petrology of Granitic Rocks. *Minerals and Rocks* **22**.

Jonasson, K., 1994. Rhyolite volcanism in the Krafla central volcano, North-east Iceland. *Bulletin of Volcanology* **56**, 516-528.

Jonasson, K., 2007. Silicic volcanism in Iceland: Composition and distribution within the active volcanic zones. *Journal of Geodynamics* **43**, 101-117.

Kennedy, B. and Stix, J., 2007. Magmatic processes associated with caldera collapse at Ossipee ring dyke, New Hampshire. *Geological Society of America Bulletin* **119**, 3-17.

Kjartansson, E. and Gronvold, K., 1983. Location of a Magma Reservoir beneath Hekla Volcano, Iceland. *Nature* **301**, 139-141.

Knesel, K. M. and Duffield, W. A., 2007. Gradients in silicic eruptions caused by rapid inputs from above and below rather than protracted chamber differentiation. *Journal of Volcanology and Geothermal Research* **167**, 181-197.

Larsen, G., Dugmore, A., and Newton, A., 1999. Geochemistry of historical-age silicic tephras in Iceland. *Holocene* **9**, 463-471.

Le Bas, M.J., LeMaitre, R.W., Streckeisen, A.L., and Zanettin, B., 1986, A chemical classification of volcanic rocks based on teh total alkali-silica diagram. *Journal of Petrology and Geochemistry*, **27**, 745-750.

Lowenstern, J. B., Charlier, B. L. A., Clynne, M. A., and Wooden, J. L., 2006. Extreme U-Th disequilibrium in rift-related basalts, rhyolites and granophyric granite and the timescale of rhyolite generation, intrusion and crystallization at Alid volcanic center, Eritrea. *Journal of Petrology* **47**, 2105-2122.

Lowenstern, J. B., Clynne, M. A., and Bullen, T. D., 1997. Comagmatic A-type granophyre and rhyolite from the Alid volcanic center, Eritrea, northeast Africa. *Journal of Petrology* **38**, 1707-1721.

Lowenstern, J. B., Persing, H. M., Wooden, J. L., Lanphere, M., Donnelly-Nolan, J., and Grove, T. L., 2000. U-Th dating of single zircons from young granitoid xenoliths: new tools for understanding volcanic processes. *Earth and Planetary Science Letters* **183**, 291-302.

Macdonald, R., Mcgarvie, D. W., Pinkerton, H., Smith, R. L., and Palacz, Z. A., 1990. Petrogenetic Evolution of the Torfajokull Volcanic Complex, Iceland .1. Relationship between the Magma Types. *Journal of Petrology* **31**, 429-459.

Macdonald, R., Sparks, R. S. J., Sigurdsson, H., Mattey, D. P., Mcgarvie, D. W., and Smith, R. L., 1987. The 1875 Eruption of Askja Volcano, Iceland - Combined Fractional Crystallization and Selective Contamination in the Generation of Rhyolitic Magma. *Mineralogical Magazine* **51**, 183-202.

Marsh, B. D., 1981. On the crystallinity, probability of occurrence, and rheology of lava and magma. *Contributions to Mineralogy and Petrology* **78**, 85-98.

Marsh, B. D., Gunnarsson, B., Congdon, R., and Carmody, R., 1990. Hawaiian basalt and Icelandic rhyolite; indicators of differentiation and partial melting. *Geologische Rundschau = International Journal of Earth Sciences (1999)* **80**, 481-510.

Martin, E. and Sigmarsson, O., 2007. Crustal thermal state and origin of silicic magma in Iceland: the case of Torfajokull, Ljosufjoll and Snaefellsjokull volcanoes. *Contributions to Mineralogy and Petrology* **153**, 593-605.

Miller, C. F., McDowell, S. M., and Mapes, R. W., 2003. Hot and cold granites? Implications of zircon saturation temperatures and preservation of inheritance. *Geology* **31**, 529-532.

Miller, J. S., Heizler, M. T., and Miller, C. F., 1998. Timing of magmatism, basin formation, and tilting at the west edge of the Colorado River extensional corridor: Results from single-crystal Ar-40/Ar-39 geochronology of Tertiary rocks in the Old Woman Mountains area, southeastern California. *Journal of Geology* **106**, 195-209.

Mork, M. E., 1984. Magma Mixing in the Post-Glacial Veidivotn Fissure Eruption, Southeast Iceland - a Microprobe Study of Mineral and Glass Variations. *Lithos* **17**, 55-75.

Nielson, J. E., Lux, D. R., Dalrymple, G. B., and Glazner, A. F., 1990. Age of the Peach Springs Tuff, Southeastern California and Western Arizona. *Journal of Geophysical Research-Solid Earth and Planets* **95**, 571-580.

O'Hara, M. J., Fry, N., and Prichard, H. M., 2001. Minor phases as carriers of trace elements in non-modal crystal-liquid separation processes; II, Illustrations and bearing on behaviour of REE, U, Th and the PGE in igneous processes. *Journal of Petrology* **42**, 1887-1910.

Onions, R. K. and Gronvold, K., 1973. Petrogenetic Relationships of Acid and Basic Rocks in Iceland - Sr-Isotopes and Rare-Earth Elements in Late and Postglacial Volcanics. *Earth and Planetary Science Letters* **19**, 397-409.

Oskarsson, N., Sigvaldason, G. E., and Steinthorsson, S., 1982. A Dynamic-Model of Rift-Zone Petrogenesis and the Regional Petrology of Iceland. *Journal of Petrology* **23**, 28-74.

Oswald, P., Geist, D., Harpp, K., Christensen, B., Wallace, P., and Anonymous, 2007. Differentiation of historical Hekla magmas. *Eos, Transactions, American Geophysical Union* **88**.

Pamukcu, A., 2010, *The evolution of the Peach Spring Tuff magmatic system as revealed by accessory mineral textures and compositions* [Master's Thesis]: Vanderbilt University, Nashville, TN.

Prestvik, T., 1979, *Geology of the Oraefi district, southeastern Iceland*. Nordic Volcanological Institute 7901. University of Iceland. 28 p.

Prestvik, T., 1985, *Petrology of Quaternary volcanic rocks from Oraefi, southeast Iceland* [Report]: Trondheim, Norwary, University of Trondheim, Norway, 81 p.

Prestvik, T., Goldberg, S., Karlsson, H., and Gronvold, K., 2001. Anomalous strontium and lead isotope signatures in the off-rift Oraefajokull central volcano in south-east Iceland. Evidence for enriched endmember(s) of the Iceland mantle plume? *Earth and Planetary Science Letters* **190**, 211-220.

Rose-Koga, E. F. and Sigmarsson, G., 2008. B-O-Th isotope systematics in Icelandic tephra. *Chemical Geology* **255**, 454-462.

Saemundsson, K., 1979. Outline of the geology of Iceland. *Joekull*, 7-28.

Sawka, W. N. and Chappell, B. W., 1988. Fractionation of Uranium, Thorium and Rare-Earth Elements in a Vertically Zoned Granodiorite - Implications for Heat-Production Distributions in the Sierra-Nevada Batholith, California, USA. *Geochimica Et Cosmochimica Acta* **52**, 1131-1143.

Selbekk, R. S. and Tronnes, R. G., 2007. The 1362 AD Oraefajoull eruption, Iceland: Petrology and geochemistry of large-volume homogeneous rhyolite. *Journal of Volcanology and Geothermal Research* **160**, 42-58.

Self, S., 2006, The effects and consequences of very large explosive volcanic eruptions. *Philosophical Transactions of the Royal Society*, A364: 2073-2093.

Sharma, K., Self, S., Blake, S., Thordarson, T., and Larsen, G., 2008. The AD 1362 Oraefajokull eruption, S.E. Iceland; physical volcanology and volatile release. *Journal of Volcanology and Geothermal Research* **178**, 719-739.

Sigmarsson, O., Condomines, M., and Fourcade, S., 1992. A Detailed Th, Sr and O Isotope Study of Hekla - Differentiation Processes in an Icelandic Volcano. *Contributions to Mineralogy and Petrology* **112**, 20-34.

Sigmarsson, O., Hemond, C., Condomines, M., Fourcade, S., and Oskarsson, N., 1991. Origin of Silicic Magma in Iceland Revealed by Th Isotopes. *Geology* **19**, 621-624.

Sigurdsson, H. and Sparks, R. S. J., 1981. Petrology of Rhyolitic and Mixed Magma Ejecta from the 1875 Eruption of Askja, Iceland. *Journal of Petrology* **22**, 41-84.

Sigvalda.G, Steintho.S, Oskarsso.N, and Imsland, P., 1974. Compositional Variation in Recent Icelandic Tholeiites and Kverkfjoll Hot Spot. *Nature* **251**, 579-582.

Sigvaldason, G. E., 2002. Volcanic and tectonic processes coinciding with glaciation and crustal rebound: an early Holocene rhyolitic eruption in the Dyngjufjoll volcanic centre and the formation of the Askja caldera, north Iceland. *Bulletin of Volcanology* **64**, 192-205.

Sparks, R. S. J., Wilson, L., and Sigurdsson, H., 1981. The Pyroclastic Deposits of the 1875 Eruption of Askja, Iceland. *Philosophical Transactions of the Royal Society of London Series a-Mathematical Physical and Engineering Sciences* **299**, 241-&.

Sparks, R.S.J., Self, S., Grattan, J.P., Oppenheimer, C., Pyle, D.M. and Rymer, H., 2005, *Super-eruptions: global effects and future threats* [Report]: Geological Society of London Working Group, The Geological Society, London, 24 p.

Sverrisdottir, G., 2007. Hybrid magma generation preceding Plinian silicic eruptions at Hekla, Iceland: evidence from mineralogy and chemistry of two zoned deposits. *Geological Magazine* **144**, 643-659.

Tait, S., Jaupart, C., and Vergniolle, S., 1989. Pressure, Gas Content and Eruption Periodicity of a Shallow, Crystallizing Magma Chamber. *Earth and Planetary Science Letters* **92**, 107-123.

Taylor, S. R. and McLennan, S. M., 1985. *The continental crust: Its composition and evolution*.

Thorarinsson, S., 1958. The Oeraefajoekull eruption of 1362. *Acta Naturalia Islandica* **2**.

Thordarson, T. and Hoskuldsson, A., 2002. Iceland. *Classic Geology in Europe* **3**.

Thordarson, T. and Larsen, G., 2007. Volcanism in Iceland in historical time: Volcano types, eruption styles and eruptive history. *Journal of Geodynamics* **43**, 118-152.

Thorson, 1971, *Igneous petrology of the Oatman district, Mohave County, Arizona,* [Ph.D. Dissertation]: Santa Barbara, California. University of California, Santa Barbara, 189 p.

Vaum, R.C., Gualda, G.A., Ghiorso, M.S., Miller, C.F. and Colombini, L.L., 2009, Using MELTS to understand the evolution of silicic magmas: Challenges and successes in modeling the Highland Range Volcanic Sequence (NV). *Transactions of the American Geophysical Union, Fall Meeting, EOS,* V13D-2058.

Vazquez, J. A. and Reid, M. R., 2002. Time scales of magma storage and differentiation of voluminous high-silica rhyolites at Yellowstone Caldera, Wyoming. *Contributions to Mineralogy and Petrology* **144**, 274-285.

Walker, B. A., Miller, C. F., Lowery Claiborne, L., Wooden, J. L., and Miller, J. S., 2007. Geology and geochronology of the Spirit Mountain Batholith, southern Nevada; implications for timescales and physical processes of batholith construction. *Journal of Volcanology and Geothermal Research* **167**, 239-262.

Walker, G. P. L., 1966. Acid volcanic rocks in Iceland. *Bulletin of Volcanology* **29**, 375-402.

Watson, E. B. and Harrison, T. M., 2005. Zircon thermometer reveals minimum melting conditions on earliest Earth. *Science* **308**, 841-844.

Watson, E. B., 1996. Dissolution, growth and survival of zircons during crustal fusion: Kinetic principles, geological models and implications for isotopic inheritance. *Transactions of the Royal Society of Edinburgh-Earth Sciences* **87**, 43-56.

Watson, E. B., Wark, D. A., and Thomas, J. B., 2006. Crystallization thermometers for zircon and rutile. *Contributions to Mineralogy and Petrology* **151**, 413-433.

Wells, R. E. and Hillhouse, J. W., 1989. Paleomagnetism and tectonic rotation of the lower Miocene Peach Springs Tuff: Colorado Plateau, Arizona, to Barstow, California. *Geological Society of America Bulletin* **101**, 846-863.

Wood, D. A., 1978. Major and trace element variations in the Tertiary lavas of eastern Iceland and their significance with respect to the Iceland geochemical anomaly. *Journal of Petrology* **19**, 393-436.

Young, R. A. and Brennan, W. J., 1974. Peach Springs Tuff - Its Bearing on Structural Evolution of Colorado-Plateau and Development of Cenozoic Drainage in Mohave-County, Arizona. *Geological Society of America Bulletin* **85**, 83-90.

Zellmer, G. F., Rubin, K. H., Gronvold, K., and Jurado-Chichay, Z., 2008. On the recent bimodal magmatic processes and their rates in the Torfajokull-Veidivotn area, Iceland. *Earth and Planetary Science Letters* **269**, 387-397.

Zellmer, G. F., Rubin, K. H., Gronvold, K., Jurado-Chichay, Z., Hernandez-Trevino, T., and Anonymous, 2004. U-series whole-rock and mineral geochemistry of recent bimodal eruptive products from the Torfajokull/Veidivotn volcanic system, south-central Iceland. *Eos, Transactions, American Geophysical Union* **85**.